NON-COVALENT INTERACTIONS IN MOLECULAR CLUSTERS: COMPETITION BETWEEN π- AND H-BONDING

A thesis submitted to The University of Manchester for the degree of
Doctor of Philosophy
in the Faculty of Engineering and Physical Sciences

2010

ANTONIO ARMENTANO

School of Chemistry

Contents

List of Figures

List of Tables

Abstract

The work presented in this thesis focuses on establishing which type of non covalent interactions (H-bond or π-bond) are present in phenol$^{(+)}$…Ar_n (*n*=2-6) and phenol$^{(+)}$…CH_4 clusters. The experimental investigation on these clusters has been performed using resonance enhanced multiphoton ionisation (REMPI), zero electron kinetic energy (ZEKE), photoionisation efficiency (PIE) and mass analysed threshold ionisation (MATI) spectroscopy.

A REMPI spectroscopy investigation on phenol…Ar_n (*n*=2-6) suggests a structure for these clusters where the argon atoms are located on the same side of the aromatic ring.

Analysis of the MATI spectra of phenol$^+$…Ar_2 provides a value for the ionisation energy (IE) (68288±5 cm^{-1}) and the long progression in the b_{xs} mode indicates a strong change of the geometry upon ionisation suggesting that the Ar atoms are more attracted toward the OH group of phenol.

The dissociation threshold for the loss of one argon atom of phenol$^+$…Ar_2 has been obtained using PIE/MATI spectroscopy. This value (~210 cm^{-1}) is significantly lower than the dissociation energy for the loss of one argon atom from phenol$^+$…Ar (535 cm^{-1}). This can explained if a π→H isomerisation process occurs upon ionisation. A similar value (~190 cm^{-1}) has been found for the dissociation threshold for the loss of one argon atom from phenol$^+$…Ar_3. The entire dissociation process for this cluster can also be explained by taking into account a π→H isomerisation. Analysis of the various dissociation thresholds observed result in binding energies of H-bound Ar ligand, D_0(H)=870 cm^{-1} and π-bound Ar ligand,D_0(π)=535 cm^{-1} for phenol$^+$…Ar, which are in good agreement with the best available theoretical values D_0(H)=946 cm^{-1} and D_0(π)=542 cm^{-1}, respectively.

A very surprising value (~810 cm^{-1}) has been obtained for the dissociation energy for the loss of four argon atoms from phenol$^+$…Ar_4. This value is even lower than the dissociation energy for the loss of two argon atoms from phenol$^+$…Ar_2 (1115 cm^{-1}). This surprising measurement is explained by proposing a structure for phenol$^+$…Ar_4 where all argon atoms are located on the same side of the ring in a tetrahedron-like structure.

Finally, the REMPI spectrum of phenol…CH_4 revealed that the origin transition S_1←S_0 is red-shifted by 61 cm^{-1} compared to the origin of the phenol monomer. This value is similar to the red-shift found for phenol…Ar (33 cm^{-1}) and confirms the geometrical similarity between argon and methane in these neutral clusters. Additionally, a further investigation on phenol$^+$…CH_4 cation demonstrates that while this cluster adopts a π-bound geometry in the neutral and first excited states, a π→H isomerisation occurs upon ionisation, similar to phenol$^+$…Ar_n (*n*= 2-3) clusters.

Declaration

I declare that no portion of the work referred to in the thesis has been submitted in support of an application for another degree or qualification of this or any other university or other institute of learning.

Copyright statement

Acknowledgements

I would like to thank:

My family and my best friends Michela and Giulio, for their love that has made this work possible.

Prof. K. Müller-Dethlefs, for his supervision.

M. Taherkhani, Dr M. Riese and Dr. X. Tong, for their constant help.

Dr M. Ford for the program code used to simulate partially rotational resolved REMPI spectra.

A.Takeda, Dr. M. Miyazaki, Dr. S. Ishiuchi, Dr. M. Sakai and Prof. M. Fujii, for the great Japan-UK cooperation.

Dr. Jiri Cerny, for introducing me to the *ab initio* methodologies.

Dr. M. Benyezzar and M. Needham, for the technical support and experimental advices.

Prof. O. Dopfer for his suggestions and advices.

Dr. J. Agger, for his support during the time spent as demonstrator.

The rest of the group: M. Varnasseri and C. Gravestock.

The mechanical workshop at the University of Manchester.

Chapter 1

Introduction

Non-covalent interactions play an important role in many chemical and biological phenomena. First, they are involved in solvation processes where an adequate description of how the nature and the number of the solvent molecules affect the interaction with the solute is still a challenging problem. Second, non-covalent interactions govern the structure of biomacromolecules such as DNA, RNA, peptides and proteins. For example, the double-helical structure of DNA, which is fundamental for the transfer of genetic information, is mainly due to the interactions between the nucleic acid bases. These bases are polar, aromatic heterocycles bonded by non-covalent interactions: planar H-bonds and π-π bonds, resulting in two structural motifs, planar H-bonding and π-stacking. In particular, very accurate calculations showed that stacking stabilisation energies are comparable to those of strong H-bonding.[1,2,3] Third, non-covalent interactions are responsible for molecular recognition processes, where a high accuracy and selectivity is crucial for the formation of biomacromolecules. Additionally, non-covalent interactions play a vital role not only in the microscopic but also in the macroscopic world. It was discovered that even a quite heavy and large animal such as a gecko can support its body weight on a vertical surface and is able to move with surprising facility even on vertical flat glass, using the non covalent interactions between the hairs located under the feet and the surface.[4]

The study of non-covalently bound complexes has attracted the attention of many research groups because they represent a simple prototype for the more complicated chemical and biological systems mentioned before. These complexes are characterised by large bond lengths and low bond energies. The main consequence of the low bond strength is the appearance of low intermolecular vibrational frequencies.

Extensive cooling of the molecular cluster is a main requisite for spectroscopic studies.[5] The invention of molecular beams produced by skimming a continuous or pulsed supersonic jet enabled molecules and clusters to be sufficiently cooled. Using microwave spectroscopy, it was then possible to analyse clusters such as Ne…HCN and the HF dimer.[6] Rotationally resolved spectra of smaller clusters[7] were subsequently obtained employing IR laser spectroscopy.[8] The investigation of exited states was made possible by using laser induced fluorescence spectroscopy (LIF)[9] and resonance enhanced multiphoton ionisation (REMPI)[10] (normally R2PI). However, it was only with the development of high-resolution laser spectroscopic methods such as zero kinetic photoelectron spectroscopy (ZEKE)[11] and mass analysed threshold ionisation spectroscopy (MATI)[12] that it was possible to achieve vibrationally resolved spectra in the cationic ground state of clusters.[13]

Unlike traditional photoelectron spectroscopy, these techniques offer sufficient spectral resolution to allow the identification of the low frequency intermolecular modes that characterise the van der Waals potential energy surface. Within their original concept of ZEKE photoelectron spectroscopy,[14] threshold electrons are created under field-free conditions and then after a small delay extracted using an electrical field. During the

waiting time kinetic electrons move into all directions while zero kinetic energy electrons are localized in the ionisation region. A pulsed field ionisation (PFI)[15,16] variant of the original ZEKE technique is commonly used for the studies of cationic systems. A further improvement in the ZEKE spectroscopy resolution can be achieved when the fractional Stark state selective field ionisation (FSSFI) scheme[17] is used.

MATI spectroscopy offers the advantage of mass selectivity,[12] however compared to ZEKE, MATI spectra generally display considerably lower resolution. To overcome to this issue a more complicate detection scheme is employed in the high resolution MATI spectroscopy.[18]

At the same time, the amelioration of *ab initio* calculations can simplify the assignment and the interpretation of spectroscopic results offering additional information on the interactions and structures adopted in molecular clusters.[19]

More recently, complexes studied in Helium nanodroplets represents a very novel method which has been object of many studies.[20] Helium droplets provide a matrix which is particularly suitable for the spectroscopic investigation of van der Waals clusters.[21,22]The kinetic and internal energy of each molecule or atom as well as the binding energy released by complexation are dissipated into the helium droplet.[23] Consequently, the aggregates inside helium droplets can reach a temperature of 0.38 K[24,25] contributing to the observation of free molecular rotation and extremely narrow ro-vibrational spectral lines. [26]

It is also worth to mention the significant increment of experiments of time-resolved photoelectron spectroscopy (TRPES) which are giving a significant contribution to the study of molecular clusters.[27] The first example of a particularly powerful application of this technique on clusters can be found in Syage's articles.[28,29] It was demonstrated that picosecond TRPES could be employed to follow reaction and salvation dynamic within clusters. This experiment was applied to excited state proton transfer in phenol…$(NH_3)_n$ clusters. It was found that a proton transfer to the solvent molecules occurs, resulting in a $PhO^-…H^+(NH_3)_n$ transient species in which the NH_3 molecules rearrange to better solvate the proton. A picosecond TRPES experiment was employed to investigate the dynamics of competition between H-bonding and π-stacking in phenol$^+$…Ar_2.[30,31] Furthermore, the recent development of high-power femtosecond laser has largely facilitated TRPES experiment obtaining new interesting discovers on dynamics in clusters.[32]

Several groups have now investigated molecular clusters of biological interest in the gas phase using the infrared depletion technique;[33,34] for example the guanine…cytosine cluster has been investigated using IR depletion, adding new vibrational information compared with previously electronic excitation spectra.[35,36]

Among non-covalently bound complexes, clusters involving aromatic molecules have attracted a very large interest. From a spectroscopic point of view, they contain a suitable chromophore since their $S_1 \leftarrow S_0$ and $D_0 \leftarrow S_1$ transitions are normally situated in the near-UV region. In particular, the vibrationally-resolved spectra of aromatic noble gas complexes provide important information for understanding intermolecular forces.[37, 38]

Complexes constituting of benzene and a noble gas such as argon were subjects of many experimental[39] and theoretical[40,41] investigations. From rotationally resolved UV spectroscopy,[42,43] it was possible to establish the structure in the neutral S_0 state: the noble gas atom is located above the aromatic ring. From the analysis of ZEKE and MATI[44] spectra it was found that the ionisation of benzene…Ar does not lead to a significant increase in the binding energy of the argon atom.

The analysis of non-covalent interactions becomes more interesting and challenging when clusters containing substituted aromatic molecules are considered. The presence of a substituent electron-donor (i.e. $-NH_2$, -OH) or electron acceptor (i. e. -F, -Cl) is the reason for the significant change in the interactions between the aromatic ring and the noble gas atom. In particular, aromatic systems having a substituent such as $-NH_2$ or -OH can offer two principal binding sites: bonding via the substituent and van der Waals bonding with the aromatic π-system (π-bond). From the spectroscopic analysis of clusters containing one argon atom and mono-substituted aromatic molecules of the type C_6H_5X (X=F,[45,46] Cl,[47] OH,[48] NH_2[48]) and for di-substituted molecules of the type $C_6H_4X_2$ (X=Cl,[49] F[50]) , π-binding above-ring was also observed. However, the change from benzene to substituted benzene derivatives causes an increase in the intensity of the intermolecular bending vibrations during excitation to the S_1 state as well during ionisation.[47] In particular for all these systems a red-shift occurs for the transition energy into the first electronically excited state S_1 as well for the ionisation energy.

This phenomena seems to be not valid for N-Butylbenzene…Ar (BB..Ar).[51,52] While the excitation energies for the first electronically excited state S_1 are red-shifted compared

to the monomer, for BB…Ar clusters with the BB conformers *anti-*; blu-shifted excitation energies were observed for BB…Ar clusters with the BB conformers *gauche-*. This was explained considering that the enhanced attractive interaction between the alkyl chain and the aromatic ring in the *gauche*-conformer in the S_1 state has been decreased by the argon atom. At the same time this supported that the argon atom is located in the same side of the aromatic ring where the alkyl chain bends towards.

Aniline…Ar and phenol…Ar have been object of many spectroscopic and computational studies.[1] A clear description of the structure of phenol…Ar was obtained from high-resolution laser induced fluorescence (LIF) spectroscopy.[53] This is consistent with recent high-level *ab initio* calculations at the CCSD(T)/CBS level,[54] which indicate that the π-bound structure is indeed the global minimum in the S_0 state, whereas the H-bound structure is only a transition state. The dissociation processes of aniline…Ar and phenol…Ar were investigated by using MATI spectroscopy obtaining very accurate values for the dissociation energetics.[18,55]

If more than one argon atom is part of the aromatic cluster then the number of possible additional configurations increases drastically. The use of *ab initio* calculations for these clusters requires a very high computational cost and the accuracy is largely reduced, affecting the facilities of determining conclusive information regarding geometry and stability of the systems under study.

A very datelined spectroscopic analysis of the aniline…Ar_n (n>1) clusters can be found in many publications.[56] In particular, recently Gu and Knee investigated the dissociation

process for aniline…Ar_2 observing that upon ionisation one of the two argon atoms moves to the hydrogen–bonded site.[55] Structural knowledge has also been obtained for the large size aniline…Ar_n (*n*=7-35) considering the local arrangement of the Argon atoms.[57]

The investigation of the non-covalent interaction becomes in equal way interesting when clusters containing aromatic systems and simple molecules are considered. In this case, the type of molecule has a relevant effect on the geometries adopted in the cluster. Spectroscopic investigation reveals that in contrast to 'spherical molecules' (e. g. CH_4[58,59]) which prefer a π-bond interaction with the phenol in the ground electronic state S_0; molecules with dipole and /or quadrupole moments (e. g. CO[60] and N_2[61]) favour H-bonds to the acid proton of phenol.

In this thesis a spectroscopic analysis (performed using R2PI, PIE and MATI spectroscopy) is extended to the higher clusters of phenol…Ar_n (*n*=2-6) and phenol…CH_4. The work presented in this thesis further confirms that the electronic spectra of aromatic molecules such as benzene and its derivates are significantly sensitive to the chemical environment. Mass selected clusters, therefore, provide an ideal testing ground for understanding size selective solvation.

In details, a description of the experimental and spectroscopic techniques used to obtain the spectra in this thesis is reported in Chapter 2 and 3. In Chapter 4 the spectroscopic results from the cation state are able to determine the vibrational modes frequencies and ionisation energy for phenol$^+$…Ar_2. The energetics for the dissociation process for the loss of one and two argon atoms from phenol$^+$…Ar_2 are explained in Chapter 5,

focusing on the change of location of one Argon atom moving from a site close the aromatic ring to a site in proximity of the hydrogen of the substituent O-H (π→H isomerisation) which occurs upon ionisation. Chapter 6 presents an analysis of the spectral shift of the origin transition $S_1 0^0$ for phenol…Ar_n (*n*=3-6) compared to the phenol monomer origin, providing an initial estimate of possible geometries and stable structures for phenol…Ar_n (*n*=3-6). The dissociation process for phenol$^+$…Ar_3 is considered in Chapter 7. The band contour analysis of the high resolution R2PI spectrum of phenol…Ar_3 is reported in Chapter 8 and supports the structure of phenol…Ar_3 hypothesised in Chapter 6. In Chapter 9, a possible explanation is given to explain the surprising value found for the dissociation energy for the loss of four argon atoms from phenol$^+$…Ar_4. Finally, in Chapter 10 the recent results obtained by R2PI, MATI spectroscopy combined with REMPI-IR dip spectroscopy of phenol…CH_4 reveal that the π→H site switching occurs upon ionisation.

1.1 References

[1] P. Hobza and K. Müller-Dethlefs, *Non-covalent Interactions. Theory and experiment*, RSC Publishing, Cambridge 2010.

[2] P. Jurečka and P. Hobza, *Chem. Phys. Lett.*, 2002, **365**, 89.

[3] P. Jurečka and P. Hobza, *J. Am. Chem. Soc*., 2002, **124**, 11802.

[4] K. Autmun, Y.A. Liang, S. T. Hsieh, W. Zesch, W. P. Chan, T. W. Kenny, R. Fearing and R. R. Full, *Nature*, 200, **405**, 681.

[5] A. J. Barnes, J. B. Davies, H. E. Hallam and J. D. R. Howell, *J. Chem. Soc. Faraday Trans. II*, 1973, **69**, 246.

[6] K. R. Leopold, G. T. Fraser and S. E. Novick, *Chem. Rev.*, 1994, **94**, 1807.

[7] H. B. Qian, W. A. Herrebout and B. J. Howard, *J. Mol. Phys*., 1997, **91**, 689.

[8] G. D. Hayman, J. Hodge, B. J. Howard, J. S. Muenter and T. R. Dyke, *Chem. Phys. Lett*., 1985, **118**, 12.

[9] D. W. Pratt, *Annu. Rev. Phys. Chem*., 1998, **49**, 481.

[10] S. Leutwyler and J. Bosinger, *J. Chem. Rev*., 1990, **90**, 489.

[11] K. Müller-Dethlefs and E. W. Schlag, *Ang. Chem. Int. Ed.*, 1998, **37**, 1346.

[12] L. Zhu and P. J. Johnson, Chem. Phys., 1991, **94**, 5769

[13] K. Müller-Dethlefs, O. Dopfer and T. G. Wright, *Chem. Rev*. 1994, **94**, 1845.

[14] K. Müller-Dethlefs, M. Sander and E. W. Schlag, *Z. Naturforforsh*. A, 1984, **39**, 1089.

[15] R. B. Metz, S. E. Bradford and D. M. Neumark, *Adv. Chem. Phys*., 1992, **81**, 1.

[16] G. Drechsler, C. Bäßmann, U. Boesl and E. W. Schlag, *Z. Naturforforsh*, 1994, **49a**, 1256.

[17] H.J. Dietrich, K. L. Y. Baranov, *Phys. Rev. Lett.*, 1996, **76**, 3530.

[18] C. E. H. Dessent, S. R. Haines and K. Müller-Dethlefs, *Chem. Phys. Lett*.,1999, **315**, 103.

[19] P. Hobza, H. L. Selzle and E. W. Schlag, *Chem. Rev*., 1994, **94**, 1767.

[20] R. Lehnig, J. A. Sebree, and A. Slenczka . *J. Phys. Chem.,* 2007, **101**, 7576.

[21] M. Lewerenz, B. Schilling and J. P. Toennies., *J. Chem. Phys.*, 1995, **102**, 8191.

[22] F**.** Stienkemeier and K. K. Lehmann., *J. Phys. B*, 2006, **39**, R127.

[23] D. Brink, S. Z. Stingari, *Phys. D*, 1990, **15**, 257.

[24] M. Hartmann, R. E. Miller, J. P. Toennies and A. F. Vilesov, *Science*, 1996, **272**, 1631.

[25] M. Hartmann, R. E. Miller, J. P. Toennies and A. F. Vilesov, *Phys. Rev. Lett.,* 1995, **75**, 1566.

[26] M. Hartmann and A. F. Vilesov, *Angew. Chem. Int. Ed*., 2004, **43**, 2622.

[27] D. M. Neumark, *Annu. Rev. Phys. Chem*., 2001, **52**, 255.

[28] J. A. Syage, *Chem.. Phys. Lett*., 1993, **202**, 227.

[29] J. A. Syage, *J. Phys. Chem.*, 1995, **99**, 5772.

[30] S. Ishiuchi, M. Sakai, Y. Tsuchida, A. Takeda, Y. Kawashima, O. Dopfer, K. Mülle-Dethlefs and M. Fujii, *Angew. Chem. Int. Ed.,* 2005, **44**, 6149.

[31] S. Ishiuchi, M. Sakai, Y. Tsuchida, A. Takeda, Y. Kawashima, O. Dopfer, K. Mülle-Dethlefs and M. Fujii, *J. Chem. Phys.*, 2007, **127**, 114307.

[32] A. Stolow, A. E. Bragg and D. M. Neumark, *Chem. Rev.*, 2004, **104**, 1719.

[33]Y. H. Lee, J. Jung, B. Kim, P. Butz, R. T. Kroemer, L. C. Snoek and J. P. Simons, *J. Phys. Chem.,* A, 2004, **108**, 69.

[34] P. Çarçabal, I. Hunig, D. P. Gamblin, B. Liu, R. A. Jockusch, R. T. Kroemer, L. C. Snoek, A. J. Fairbanks, B. G. Davis and J. P. Simons, *J. Am. Chem. Soc*., 2005, **127**, 11414.

[35] W. Chin, I. Compagnon, J. Dognon, C. Canuel, I. Dimicoli, G. von Helden, G. Meijer and M. Mons, *J. Am. Chem.*, 2005, **127**, 1388.

[36] N.C. Polfer, B. Paizs, L.C. Snoek, I. Compagnon, S. Suhai, G. Meijer, G. von Helden and J. Oomens, *J. Am. Chem.*, 2005, **127**, 8571.

[37] H. J. Neusser and H. Krause, *Chem. Rev*., 1994, **94**, 1829.

[38] C. E. H. Dessent and K. Müller-Dethlefs, *Chem. Rev.*, 2000, **100**, 3999.

[39] P. Ball, *Chem. Rev.*, 2008, **108**, 74

[40] P. Hobza, H. L. Selzle and E. W. Schlag, *J. Chem. Phys.*, 1991, **95**, 391.

[41] R. J. Moulds, M. A. Buntine and W. D. Lawrance, *J. Chem. Phys.*, 2004, **121,** 4635.

[42] T. Weber, A. von Bargen, E. Riedle and H. J. Neusser, *Int. J. Chem. Phys*., 1990, **92**, 90.

[43] E. Riedle, R. Sussmann, T. Weber and H. J. Neusser, *J. Chem. Phys.*, 1996, **104**, 865.

[44] L. A. Chewter, K. Müller-Dethlefs and E. W. Schlag, *Chem.. Phys. Lett*., 1987, **135**, 219.

[45] E. D. Lipp and C. J. Seliskar, *J. Molec. Spectroscopic.*, 1981, **87,** 242.

[46] T. L. Grebner, P. Unold and H. J. Neusser, *J. Phys. Chem. A*., 1997, **101**,158.

[47] G. Lembach and B. Brutshy, *Chem Phys. Lett*., 1997, **273**, 421.

[48] E. J. Bieske, M. W. Tainbird, I. M. Atkinson and A. W. Knight, *J. Chem Phys*., 1989, **91**, 752.

[49] W. D. Sands, L. Jones and R. Moore, *J. Chem Phys*., 1989, **93**, 6601.

[50] M. C. Su and C. S. Parmenter, *J. Chem Phys*., 1991, **156**, 261.

[51] X. Tong, M. S. Ford, C. E. H Dessent, K. Müller-Dethlefs, *J. Chem. Phys.*, 2003, **119**, 12908.

[52] X. Tong, J. Cerny, C. E. H Dessent, K. Müller-Dethlefs, J. Phys. Chem.. A, 2008, **112**, 5872.

[53] I. Kalkman, C. Brand, T. B. C. Vu, W. L. Meerts, Y. N. Svartsov, O. Dopfer, X. Tong, K. Müller-Dethlefs, S. Grimme and M. Schmitt, J. Chem. Phys., 2009, **130**, 224303.

[54] J. Çerny, X. Tong, P. Hobza, and K. Müller-Dethlefs, *J. Chem. Phys.*, 2008, **128**, 114319.

[55] Q. Gu and J. L. Knee, *J. Chem. Phys.*, 2008, **128**, 64311.

[56] P. Hermine, P. Parneix, B. Coutant, F. G. Amar and P. Brechignac, *Z. Phys. D*, 1992, **22,** 529; P. Parneix, P. Brechignac and F. G. Amar, *J. Chem. Phys.*, 1996, **104**, 983; S. Douin, S. Piccirillo and P. Brechignac, *Chem. Phys. Lett.*, 1997, **273,** 389; S. Douin, P. Parneix, F. G. Amar and P. Brechignac, *J. Phys. Chem. A*, 1997, **101,** 122.

[57] T. Pino, P. Parneix, S. Douin and P. Brechignac, *J. Phys. Chem. A*, 2004, 108, 7364.

[58] N. Solcà and O. Dopfer, *J. Chem Phys*., 2001, **105**, 5637

[59] G. V. Hartland, B. F. Henson, V. A. Venturo and P. M. Felker, *J. Chem Phys*., 1992, **96**, 1164.

[60] S. R. Haines, C. E. D. Dessent and K. Müller-Dethlefts, *J. Chem. Phys*, 1999, **111**, 1947.

[61] S. R. Haines, W. D. Geppert, D. M. Chapman, M. J. Watkins, C. E. D. Dessent, M. C. R. Cockett and K. Müller-Dethlefts, *J. Chem. Phys.*, 1998, **109**, 9244.

Chapter 2

Experimental techniques

2.1 Introduction

This chapter provides a general overview of the experimental methods and spectroscopic techniques used to record the data presented in this thesis. Most of the descriptions are generalised; specific details and conditions relating to each molecular system are provided in the experimental sections. Additionally a short description of the experimental observables obtained from these experimental methods is also reported in the last section of the chapter.

2.2 Supersonic free-jet expansion and molecular beam

Supersonic free-jet expansion is a convenient technique used to prepare a sample in the gas phase for spectroscopic studies of isolated molecules or molecular aggregates of limited dimensions.

A supersonic jet consists of a mixture of the sample and rare gas which is expanded through an orifice or nozzle of small diameter (about 100-500 μm). The molecules are accelerated in this expansion process due to the difference in pressures between the two regions. The first stage of this process is characterized by a high number of collisions

and high velocity of the gas phase in the direction of expansion propagation. This velocity is found to be inversely proportional to the masses ($v \alpha m^{-0.5}$). In the second stage the molecules eventually gain a very narrow distribution equal to the velocity of the carrier gas (atoms such as He, Ne or Ar or "light" molecules such H_2 are generally used as a carrier gas) because of the high number of collisions. The large number of collisions in the gas expansion process has two important consequences:

- After the initial stage of the expansion all the molecules will move with the same velocity distributed on a limited solid angle.
- A significant reduction of the population in the rotational and vibrational excited levels with a consequent simplification of the measured spectrum.

There are no collisions after the first stage of the expansion as all molecules have the same velocity. Therefore, the weakly-bound molecular species formed during the first moments of the supersonic expansion survive for a long time because the collision rate decreases rapidly with the distance from the source of the expansion.

The free expanding gas can be better controlled using a skimmer assembly placed close to the nozzle. This device is used for selecting only a small part of the expanded gas (molecular beam). In an ideal spectroscopic experiment, the two collimated beams (molecular and laser) interact to significantly decrease the Doppler effect which causes inhomogeneous broad bands (the region of interaction is well-defined).

2.3 Time-of-flight mass spectrometry

Time-of-flight mass spectrometry (TOF MS) are based on a simple mass separation principle. The ions are accelerated by a constant homogeneous electrostatic field and therefore will move in the same direction. Their velocities are related to their mass-to-

charge (*m/z)* ratio; therefore the times of arrival at the detector directly indicate their masses:

$$t= (2md/eE)^{1/2} + L(m/2eV_0) \quad [2.1]$$

where m=mass of particle, e=electronic charge, E=electrostatic field applied in source, d=length of accelerating region, L=length of field free region, and V_0= accelerating potential.

The TOF instrumentation possesses a number of advantages over most other types of mass analyser:

1. Theoretically unlimited mass range
2. No need to scan the ion beam
3. Complete mass spectrum for each ionisation
4. Only a small amounts of sample are necessary

Wiley and McLaren[1] observed that ions of a particular mass-to-charge ratio would reach the detector with a spread in the arrival times, however the effects of uncertainty in the time of ion formation, location in the extraction field and initial kinetic energy result in reduced resolution. For this reason a pulsed two-grid ion source was introduced in the mass spectrometer to compensate for temporal, spatial and kinetic energy distributions.

In 1966, Mamyrin and co-workers[2] enhanced the MS-TOF instrumentation to correct for the temporal spread due to the initial velocity of the ions by using a “reflectron” (RE) which consists of a decelerating and reflecting field (a schematic representation of a RE-TOF is shown in Figure 2.1). In principle, ions of the same mass but high kinetic

energy will penetrate the decelerating field further then ions with lower kinetic energy, therefore the faster ions will spend more time within the reflecting field. Theoretically, the resolution of the peaks in the mass spectrum will only be dependent on the time-width of ion formation. The single-stage is the simplest type of reflectron; a single electric field region is created between two parallel flat grids. In a double–stage reflectron,[3] two separate homogeneous field regions of different potential gradient are utilised. The resolution is greatly improved with a double-stage reflectron, particularly for ion beams with broad kinetic energy distributions.

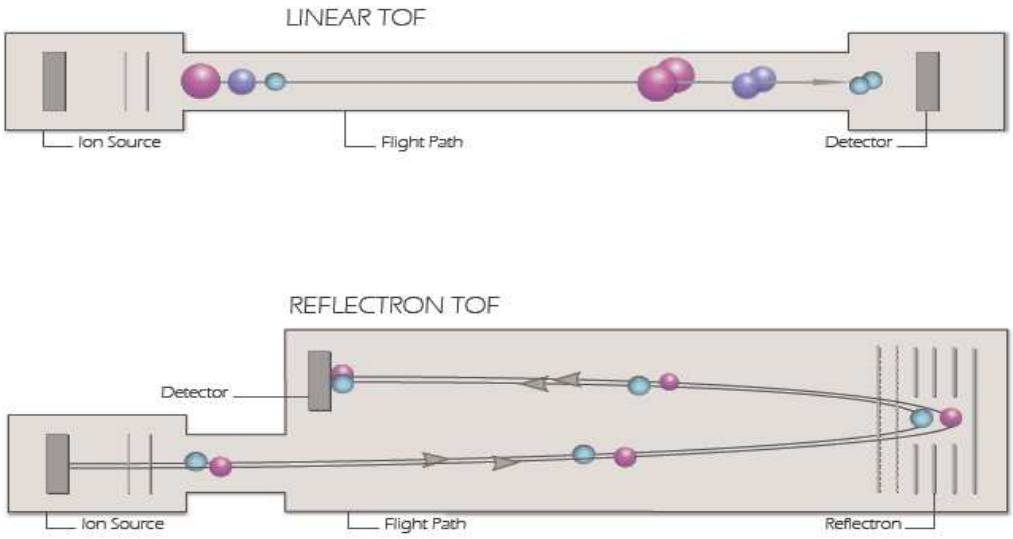

Figure 2.1: A schematic of linear time of flight and reflectron time of flight.

2.4 Resonance enhanced multi-photon ionisation

Resonance Enhanced Multi-Photon Ionisation (REMPI) spectroscopy is an appropriate technique to study the electronic levels of isolated molecules or clusters when it is combined with a method to mass separate ions such as MS-TOF.[4]

The photoionisation of a molecular system can be achieved *via* three principle mechanisms (Figure 2.2). In the direct photoionisation process a molecular system is excited to an ionisation continuum by absorption of one high energy photon. The ionisation process can be accomplished in a multi-photon ionisation (MPI) scheme *via* a virtual intermediate state. However, the absorption cross-section of such a process is very small (~ 10^{-50} cm^2) and extremely high photon fluxes are required (the application of a strong laser field is suitable) to make the scheme work.

Considerable improvement in the ionisation probability can be obtained if the first photon is in resonance with an excited state of the molecule: the one-colour (1+1) REMPI process is shown in Figure 2.2. This scheme involves one-colour two-photon ionisation and is sometime referred to R2PI. Further improvement can be achieved in two-colour (1+1') REMPI as most of the fragmentation channels otherwise present in one-colour scheme are effectively suppressed. In the (1+1') scheme, the first laser excites to the S_1 state, while a second laser takes the system slightly above the ionisation threshold. Any excess energy that could funnel into a fragmentation channel is thus kept to a minimum. Further and more complicated schemes, e.g. (2+1') REMPI where the initial excitation is achieved under simultaneous absorption of two photons are possible but lead to a lower ionisation rate.

REMPI schemes probe the excited states which are used as intermediates. With the appropriate laser source they allow the study of the vibronic and sometimes even rovibronic structure of the excited state. The ion current is monitored as a function of the frequency (ν_1). The ions are extracted by a pulsed or static field and mass selected *via* TOF before reaching the detector, which is usually a multi-channel plate (MCP).

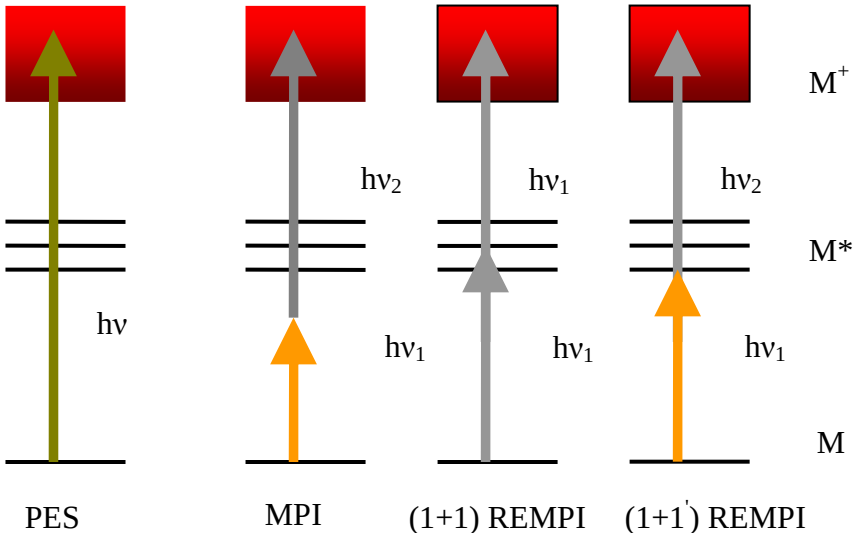

Figure 2.2: Schematic diagram of photoionisation mechanisms.

2.5 Photoionisation efficiency spectroscopy

Photoionization efficiency (PIE) spectra can be a useful tool to estimate the ionisation energy or dissociation energy prior to a ZEKE/MATI experiment.

In PIE spectroscopy[5,6] the ion yield is determined as a function of the total photon energy. For every (ro)vibronic ionisation threshold the cross-section for photoionisation rises in the form of a step-like function with the energy. However this technique is not very accurate when large molecular complexes are studied. In this case, the steps are often not pronounced[7,8], and it is only possible to give a value for the ionisation energy of the molecular systems within a range of 30-50 cm^{-1}.

The experimental process to acquire the PIE is very simple: the excitation laser is fixed onto an intermediate resonance state, whilst the ionisation laser is scanned over the ionisation threshold (Figure 2.3) and the ion signal is detected.

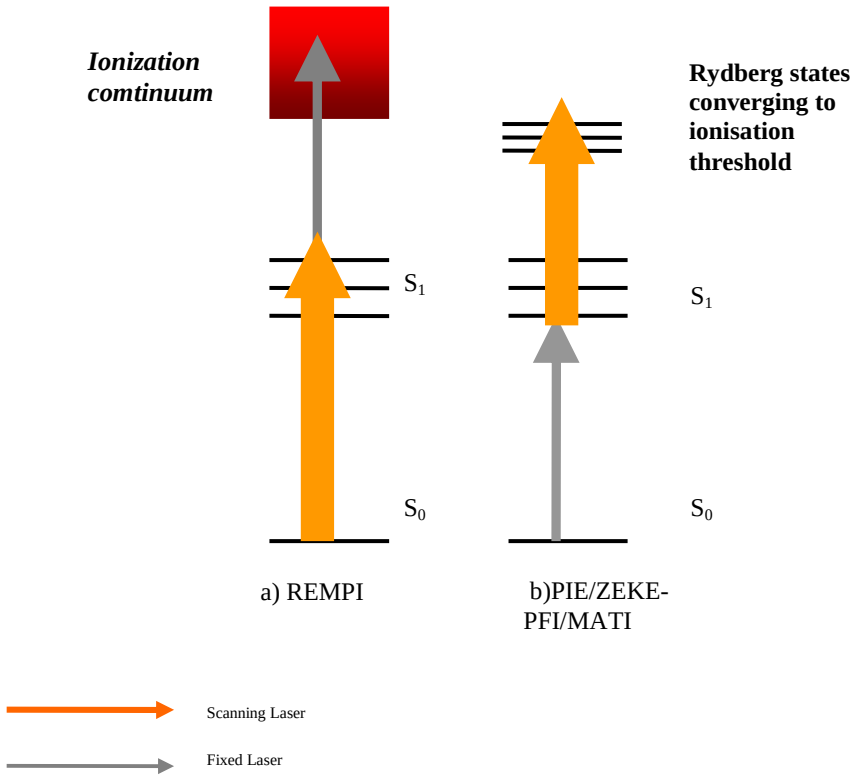

Figure 2.3: Basic principle of REMPI and PIE/ ZEKE-PFI / MATI spectroscopy.

2.6 Zero electron kinetic energy spectroscopy

The zero electron kinetic energy pulsed field ionisation (ZEKE or ZEKE-PFI) spectroscopy is a technique developed from traditional photoelectron spectroscopy (PES). In conventional PES an atom or molecule is irradiated with light of a fixed frequency, ν. The ejected electrons possess different amounts of kinetic energy

depending on which orbital they come from. This kinetic energy is the measured quantity in the PES and is related to the ionisation energy (IE) of the molecule through the equation:

$$h\upsilon = \frac{1}{2}mv^2 + IE \qquad [2.2]$$

While this approach has been used extensively to determine ion structure, it suffers from several disadvantages; the most important is a limited resolution of ~5−10 meV.

An improvement to the resolution of PES by two orders of magnitude to 0.1 meV was obtained in the 1984 with the introduction of ZEKE spectroscopy.[9] It has proven to be a valuable and very sensitive tool in the study of the rovibronic structure of cations. In ZEKE, ionisation is achieved *via* photo-excitation to a resonant intermediate state, where a second scanning, or probe laser, excites the electrons to long-lived high-*n* Rydberg states which are resistant to stray fields and lie a few wavenumbers below each rovibrational ionisation threshold of the molecular system. A pulsed field subsequently ionises the Rydberg states producing electrons and ions. The complete temporal discrimination between kinetic and these pseudo-ZEKE electrons is achieved simply by introducing a delay between the excitation and the pulsed field abstraction. ZEKE and non-ZEKE electrons can be distinguished from each other by the time difference inherent between the two types of electrons in the TOF spectrum. The presence or absence of the ZEKE electron TOF signal depends on whether or not the probe laser is in resonance with a rovibronic state of the ion. Hence the resolution of ZEKE is

theoretically only limited by the bandwidth of the laser and the distribution of the resonant Rydberg states. [10,11]

Several important consequences result from excitation to high-*n* Rydberg states just below the threshold. Firstly, the high-*n* Rydberg states have exceptionally long lifetimes,[12] which are attributed to state mixing by stray fields in the ionisation volume. Thus, a relatively long delay is used to ensure complete separation between ZEKE and non-ZEKE electrons. Secondly, there is a red shift in the ionisation energy as some of the high-*n* Rydberg states are field ionised. Additionally, the applied electric field causes a width of the ZEKE peak which is broader than the laser bandwidth.

According to a classical treatment of the ionisation process the electric field, *F* the turning point on the Coulomb potential between the ionic core and the high *n*-Rydberg electron lies 6.1 $F^{1/2}$ cm^{-1} below the ionisation threshold.[13] A quantum mechanical treatment indicates that the shift is by 3.1 $F^{1/2}$ cm^{-1}.[14] However experiments show that the red onset of the ZEKE peak appears around 4.6 $F^{1/2}$ below the ionisation threshold.[15,16]

An enhancement to the PFI scheme to reduce peak broadening from field ionisation has been obtained with the fractional Stark state selective field ionisation (FSSFI) scheme (Figure 2.4).[17] After laser excitation of a species to create Rydberg excited molecules, the manifold of Stark states present can be described in terms of two regions. The higher energy “blue’’ states (orbital dipole anti-parallel to the field) are more resilient to ionisation than the “red’’ (parallel alignment) states.

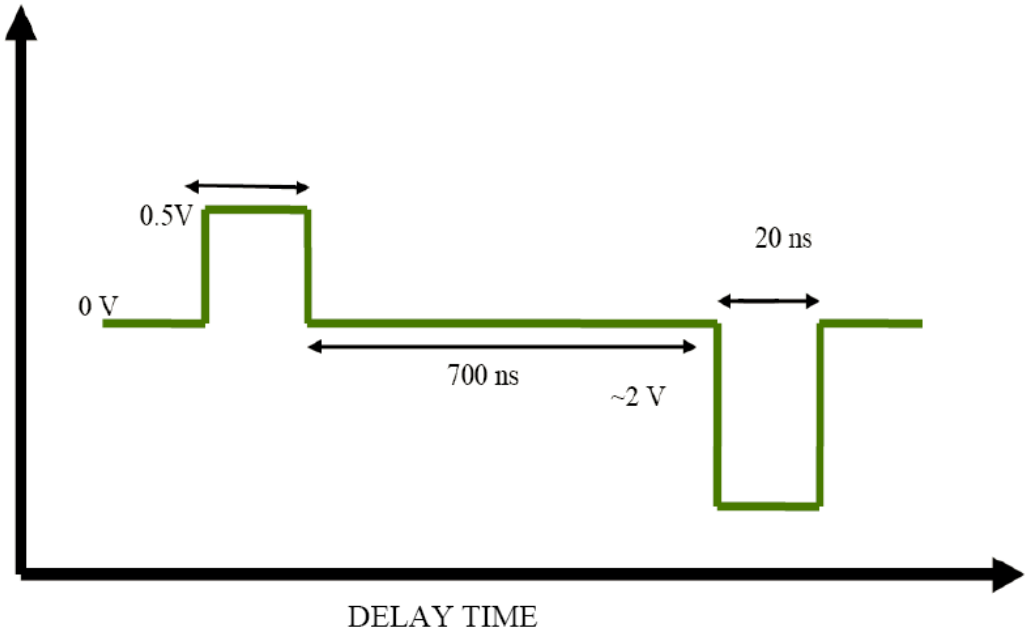

Figure 2.4: Pulse sequence for FSSFI.

On application of an offset pulse, the more fragile "red'' Stark states are ionised, while the more resilient "blue" Stark states survive. Upon application of a second pulse of opposite direction, the surviving blue states are transferred into less resilient red ones (Stark state inversion) with respect to the second field and can be ionised. The use of this method can improve the spectral resolution of peaks in the ZEKE spectrum by more than a factor of eight.[18]

2.7 Mass analyzed threshold ionisation spectroscopy

One disadvantage of the ZEKE spectroscopy is that it is not a mass-selective method; it is not possible to distinguish between ZEKE electrons originating from different species which may have similar ionisation energies.

Mass selection is an essential requirement particularly in studies of fragmentation processes of molecular complexes where the simultaneous detection of fragment and parent ion is strongly necessary. Mass analyzed threshold ionisation (MATI) spectroscopy[19] is essentially a variant of ZEKE spectroscopy; the ions generated by the field ionisation are detected instead of the ZEKE electrons, therefore MATI has the added advantage of mass selectivity. A slightly different technique is needed to separate spontaneous ions from the MATI ions compared to ZEKE spectroscopy. The spatial separation of the spontaneous ions from Rydberg states is experimentally more difficult and can only be achieved with a separation field (static or pulsed). The MATI experiment can be schematically described as follows:

After a delay of ~0.5 μs from the laser excitation an offset field of 1-3 V/cm is applied to spatially separate the neutral Rydberg molecules and prompt ions. This low voltage also field ionises a small subset of the total population of Rydberg states. After a delay time (~20 μs) a high-voltage pulsed field ionises the neutral Rydberg states and accelerates prompt and MATI ions into the TOF. As the prompt ions have been accelerated from a position of greater electric potential they have a larger kinetic energy than the MATI ions. Consequently, the prompt ions will reach the MCP first. The experimental procedure for MATI spectroscopy is illustrated in Figure 2.5 (left side).

Compared to ZEKE, MATI spectra show a considerably lower spectral resolution. As a high-voltage extraction pulse is used to field-ionise the neutral Rydberg molecules, a very large Stark shift in the ionisation energy occurs. This field ionises a very large slice of high-*n* Rydberg states and consequently generates band broadening. Similar to ZEKE spectroscopy, fractional Stark state selective field ionisation can be used in MATI spectroscopy to achieve a better resolution (this method is commonly known as high

resolution MATI).[20] The method used is shown in Figure 2.5 (right side). A schematic of the sequence of pulses used in high-resolution MATI is shown in Figure 2.6. The complete procedure to obtain the high-resolution MATI spectra can be summarised as follows: After a delay of 0.5 μs from the laser excitation, a pulse field of 0.5-1 V/cm is applied to separate the prompt ions from Ryderg-state molecules. Then a short, low-voltage pulse of inverted polarity is applied. Some Rydberg molecules are field ionised and the ions generated give rise to the high-resolution MATI signal. A third pulse is applied to separate the ions created from the previous pulse from the remaining neutral Rydberg molecules which are now also field-ionised, giving rise to the low-resolution MATI signal. Thus, a high voltage pulse is applied to accelerate prompt, high and low resolution MATI ions into the TOF so three different peaks are observed on the mass spectrum.

The high-resolution MATI signal has been shown to be directly equivalent to the ZEKE signal and is generally of better quality as there is usually minimal background noise. In addition, the ion signal is more stable than the electron signal as it is less susceptible to stray fields.

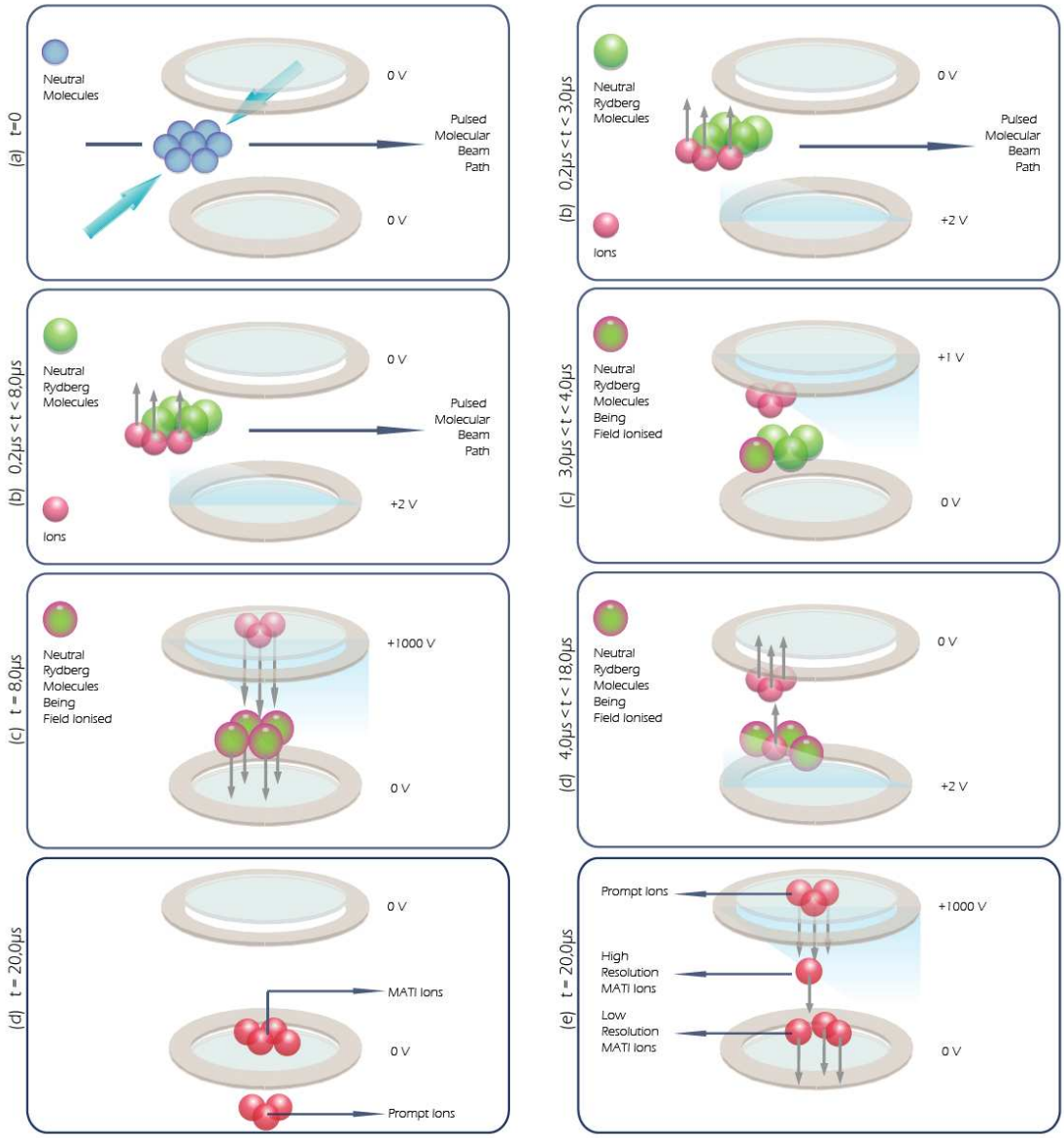

Figure 2.5: Schematic representation of the MATI principle (low-resolution MATI on the left side and high-resolution MATI on right side).

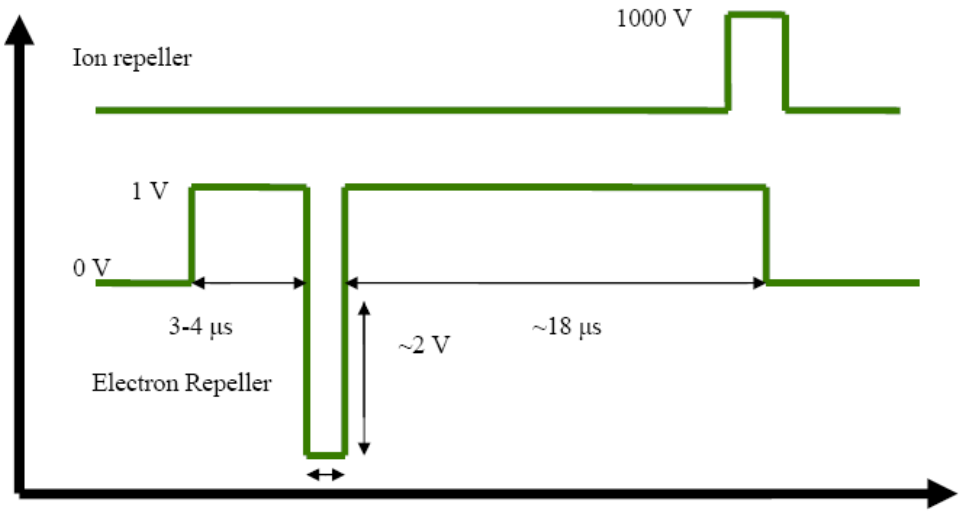

Figure 2.6: Pulses sequence in the high-resolution MATI.

2.8 Intensity of the MATI signal: correlations with the power intensity of the excitation laser

While the MATI resolution can be enhanced to reach near-ZEKE resolution using a sequence of different pulses as shown in the high-resolution MATI, the reduced signal and the signal-to-noise are still issues in the MATI experiment. These are particularly significant when:

- MATI spectra are obtained via less intensive intermediate states.
- The systems under study are VdW or hydrogen bound complexes.

In previous MATI studies on p-xylene,[21] it has been shown how the intensity of the MATI signal can be improved by increasing the intensity of the excitation laser (first laser); in these conditions it has been possible to record spectra via different, less intensive intermediate states. The MATI intensities recorded *via* $S_1 0^0$ and *via* one of the

S_1 vibration level for p-xylene and the values of the first laser are reported in Table 2.1 and 2.2. These results clearly show how the MATI intensity increases as the first laser power increases. The resolution is not affected and the signal shape is only marginally affected.

When molecular clusters are studied using MATI spectroscopy other factors must be considered. The recording of a REMPI spectrum is the first step preceding the investigation of the ion ground state by ZEKE or MATI spectroscopy and the ZEKE/MATI spectra are recorded with the same first laser intensity used in the REMPI experiment. In the REMPI experiment, the intensity of the first laser is usually selected to be as small as possible to reduce the probability of higher cluster fragmentation. As a consequence of how the experiment is carried out, the two-colour signal is much stronger than the one-colour signal.

Table 2.1: MATI signal strengths for various pump laser intensities for p-xylene when the S_1 0^0 transition is used as an intermediate state (from Ref.21).

MAT I signal (relative intensity)	**First laser power /µJ**
4	4
30	18
54	35
90	52

Table 2.2: MATI signal strengths for various pump laser intensities for p-xylene when the S_1 vibration at 553 cm^{-1} is used as an intermediate state (from Ref.21).

MATI signal (relative intensity)	**First laser power /µJ.**
4	4
15	18
55	35
65	52
115	70
170	120

Also for clusters, a change of intensity of the first laser can be responsible for an increase of the MATI intensity, as was observed in the case of molecular systems. The results obtained for phenol…Ar are an example of how the MATI signal changes as a function of intensity of the first laser for complexes.

The phenol…Ar complex was chosen for this experiment for the reason that investigations of the ion ground state of phenol…Ar are reported in detail in Ref.20, therefore the results concerning the ionisation energy and the features present in the spectrum can be compared. The apparatus and experimental details used to record the MATI spectrum of phenol…Ar cluster are described in the next chapters.

Figure 2.7 shows the intensities of the MATI signal recorded *via* the $S_1 0^0$ origin transition as a function of the different intensities of the excitation laser. The intensity of the MATI signal increases almost linearly in a 0-100 µJ range (the signal increases 50 times when the intensity of the first laser is increased from ~1 µJ to ~ 100 µJ). In the range 100-200 µJ the intensity of the MATI signal only increases by ~10 µJ. When the intensity of the first laser is increased further, the MATI signal decreases (at 400 µJ the

signal is 1/3 smaller than the value obtained at 200 µJ). The most intense signal was obtained at 200 µJ.

As already observed in the case of the isolated molecules, a higher intensity of the first laser does not have an enormous influence on the resolution and the shape of the peaks observed in the MATI spectrum. This can be easily inferred by a comparison of the two MATI spectra of phenol…Ar recorded *via* the $S_1 0^0$ origin transition at two different intensities (Figure 2.8). The signal is bigger in the spectrum where a higher intensity of the first laser is applied and an improvement in the ratio-signal-to-noise is also observed. Only a small change in the width of the peaks can be observed. In conclusion, the increase of the excitation laser intensity leads to an increase of the MATI signal and an improvement of the signal-to-noise ratio with negligible influence on the resolution.

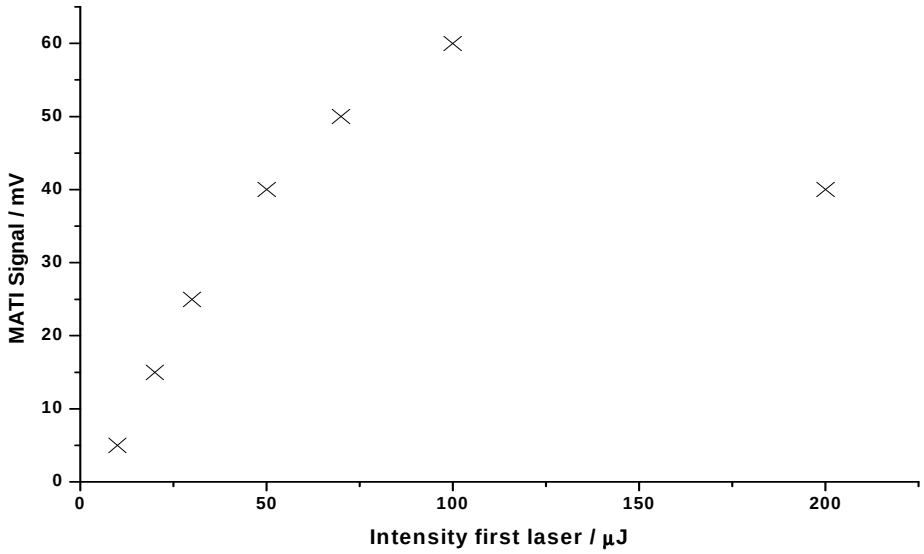

Figure 2.7: Dependence of the MATI signal relative to the intensity of the first laser in a MATI experiment on phenol…Ar recorded *via* the $S_1\ 0^0$ transition.

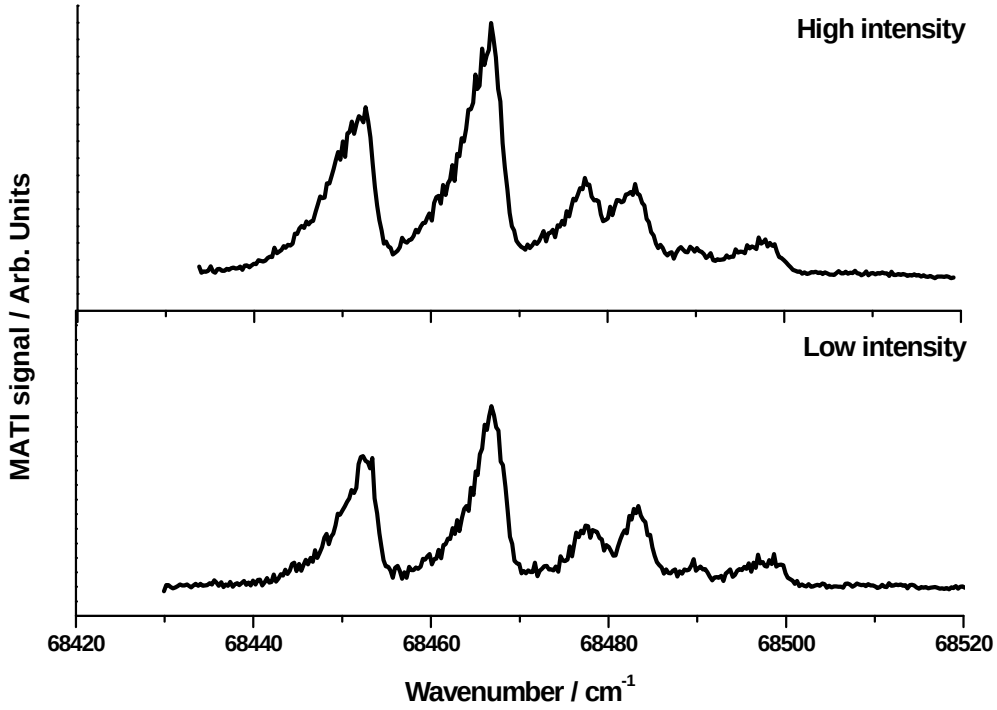

Figure 2.8: MATI spectra of phenol^{+}…Ar at two different intensities of the first laser. Stronger first laser intensity leads to an enhancement of the MATI signal while the spectral resolution is almost unchanged.

2.9 Experimental observables

The information which can be obtained from analysis of the spectra recorded using the spectroscopic methods described in this chapter is the first step towards establishing the properties and the possible structure of non-covalent interactions in the molecular clusters under study.

2.9.1 Vibrational modes frequencies

Only vibrations with favourable Frank Condon factors and allowed by the selection rules (a change in electric dipole moment has to occur during vibration and $\Delta v = \pm 1$)

can be observed, with the result that not all possible vibrations can be detected in the spectrum.

The frequencies of the intermolecular vibrations which arise upon formation of a complex are present in the sub-100 cm^{-1} region (often below 50 cm^{-1}). For a cluster constituting of two molecules, six intermolecular vibrations exist. For a cluster with a molecule and an atom, the number of intermolecular frequencies is reduced to three. However, the intermolecular frequencies cannot uniquely identify a specific complex because they are very similar for the various types of non-covalent complex.

2.9.2 Spectral shift

A comparison of origin transitions between monomer and complex is a measure of the relative differences between upper and lower states of energetic perturbations induced by clustering. A red-shift is a consequence of the fact that the complex has reduced the energy difference between two states; a blue-shift represents an increase in the difference. The spectral shift is therefore an indication of the stability in each state and whether there is a difference in stability between two states.

2.9.3 Dissociation energy

For molecular clusters the most useful application of MATI comes from the observation of the dissociation of the Rydberg state ion core which allows the determination of the dissociation and binding energy.[22,23] The simultaneously recorded MATI spectra at the mass channel of the cluster and fragments can give a very accurate value for the dissociation energy. The dissociation energy can be accurately determined by

considering the difference between the disappearance of the cluster ion and the appearance of the daughter fragment ion.

2.9.4 Rotational band contour analysis

A comparison of the high-resolution REMPI spectrum with the simulated spectra using rotational constants of calculated geometries for the cluster analysed can be an efficient method for the direct determination of the structures of a molecular cluster under study.

2.10 References

[1] W. C. Wiley, and I. H. MacLaren, *Rev. Sci. Instr.*, 1955, **26**, 1150.

[2] B. A. Mamyrin, V. I. Karataev, D. V. Shmikk and V. A. Zagulin, *Sov. Phys. JETP*, 1973, **37**, 45.

[3] V. I. Karataev, B. A. Mamyrin and D. V. Shmikk, *J. Tech. Phys*., 1971, **16**, 1498.

[4] J. M. Hollas, *High Resolution Spectroscopy*, 1998.

[5] J. Berkowitz, *Photoabsorption, Photoionization and Photoelectron Spectroscopy, Academic Press,* New York, 1979.

[6] K. H. Fung, E. W. Henke, T. R. Hays, H. L. Seize and E. W. Schlag, *J. Phys. Chem.* 1981, **85**, 3560.

[7] N. Gonohe, H. Abe, N. Mikami and M. Ito, *J. Phys. Chem.* 1985, **89,** 3642.

[8] O. Dopfer, *Dissertation*, TU München 1994.

[9] K. Müller-Dethlefs, M. Sander, and E. W. Schlag, *Z. Naturforsch. A*. 1984, **39**, 1089.

[10] K. Müller-Dethlefs and E. W. Schlag, *Annu. Rev. Phys. Chem*., 1991**, 42,**109**.**

[11] K. Müller-Dethlefs, E. W. Schlag, K. Wang and V. McKoy, *Advances in Chemical Physic,* **1**995, **XC**, 21.

[12] G. Reiser, W. Habenicht, K.Müller-Dethlefs and E. W. Schlag, *Chem. Phys. lett*., 1988, **152**, 119

[13] M. J. Watkins, *D. Phil. Thesis*, University of York, 2000

[14] D. Kleppner, M. G. Litman and M. L. Zimmermann, *Rydberg states of Atoms and Molecules*, Cambridge University Press 1983.

[15] P. Pilet, H. B. van Linden van den Heuvell, W. W. Smith, R. Kachru, N. H. Tran and T. F. Gallagher, *Phys. Rev*. A, 1980, **30**, 280.

[16]R. J. Damburg and V. V. Kolosov, *Rydberg states of Atoms and Molecules*, Cambridge University Press., 1983.

[17] H. J. Dietrich, K. Müller-Dethlefs and L. Y. Baranov, *Phys. Rev. Lett*., 1996, **76**, 3530.

[18] T. P. Softley, *Int. Rev. Phys. Chem.*, 2004, **23**, 1.

[19] L. Zhu and P. Johnson, *J. Chem. Phys.*, 1991, **94**, 5769.

[20] C. E. H. Dessent, S. R. Haines and K. Müller-Dethlefs, *Chem. Phys. Lett.*, 1999, **315**, 103.

[21] F. Gunzer and J. Grotemeyer, *Int. J. Mass. Spec.* 2002, **228**, 921.

[22] H. Krause and H. J. Neusser, *J. Chem. Phys*., 1992, **97**, 5923.

[23] H. Krause and H. J. Neusser, *J. Chem. Phys.*, 1993, **99**, 6278.

Chapter 3

Experimental set-up

3.1 Apparatus overview

Figure 3.1 shows a representation of the apparatus used to obtain the experimental results reported in this thesis.

The laser system consists of two dye lasers pumped by a Nd:YAG laser. The frequency-doubled output of the first dye laser is used to promote the excitation to the intermediate state S_1 of the molecular system under study; the output of the second dye laser promotes the ionisation or population of Rydberg states.

Two chambers are separated by a conical skimmer. In the first chamber the molecular systems are produced in a pulsed supersonic jet expansion of the sample seeded in a solvent/carrier gas mixture. In the second chamber a collimated molecular beam is produced by skimming the jet expansion. The molecular beam is perfectly perpendicular with the two collinear beams of the two dye lasers entering the main chamber from opposite sides through quartz windows. The ions produced are accelerated by ion optics separated by a reflectron time-of-flight (RE-TOF) spectrometer and detected on micro-channel plate (MCP) situated in the lower part of the chamber system. However, the

electrons are detected on MCP localized above the main chamber. Control of the whole system and data acquisition are handled by home made software.[1] This set-up can be used to perform REMPI and ZEKE/MATI spectroscopy.

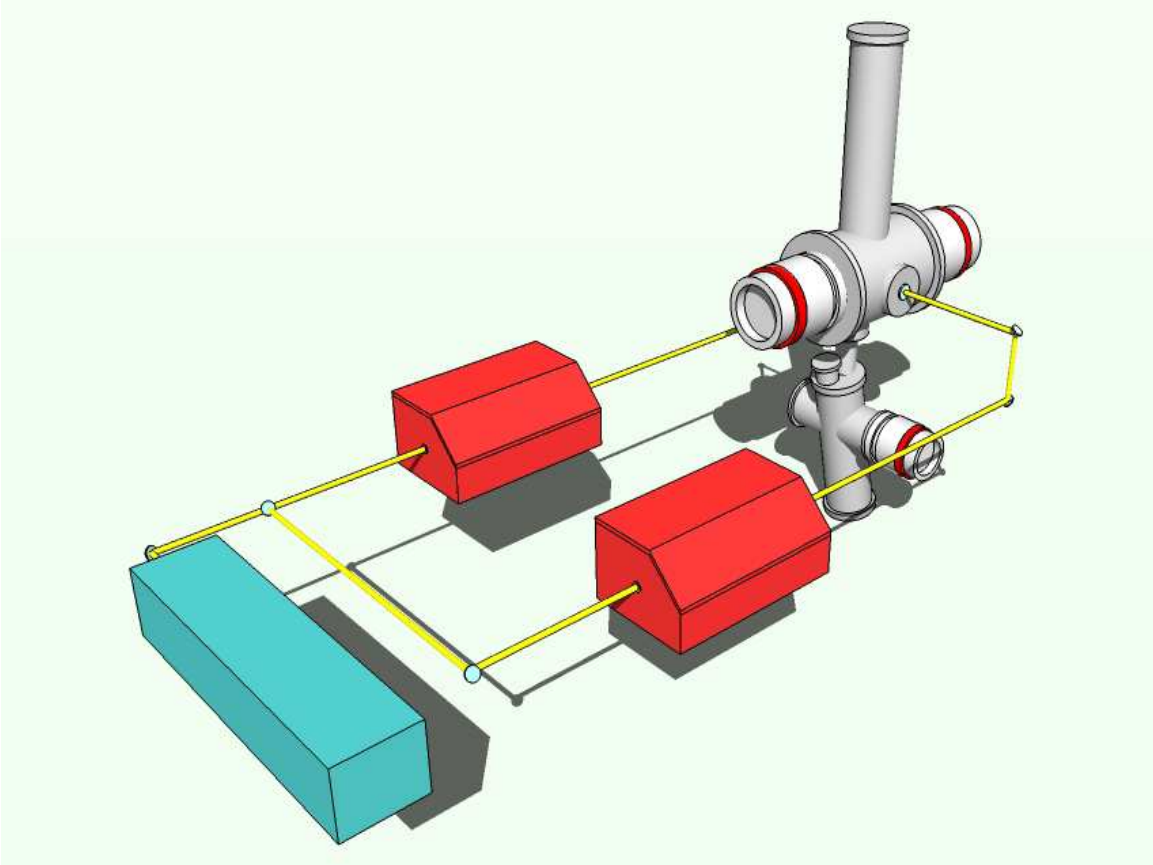

Figure 3.1: Experimental set-up, illustrating the laser system and vacuum chamber.

3.2 Laser system

A Nd:YAG laser (continuum Surelite-III) is used as a pump laser. It works at a repetition rate of 10 Hz with 3-5 ns width output. This laser is operated in the Q-switching mode by using a Pockels cell. A fundamental output of 1064 nm (maximum energy 850 mJ) is produced, a second harmonic (SHG) at 532 nm (maximum energy 400 mJ) is obtained from the fundamental emission and a third harmonic (THG) at 355 mJ (maximum energy 250 mJ) is produced via an appropriate beam separation set. Figure 3.2 shows a schematic representation of the Surelite III. [2]

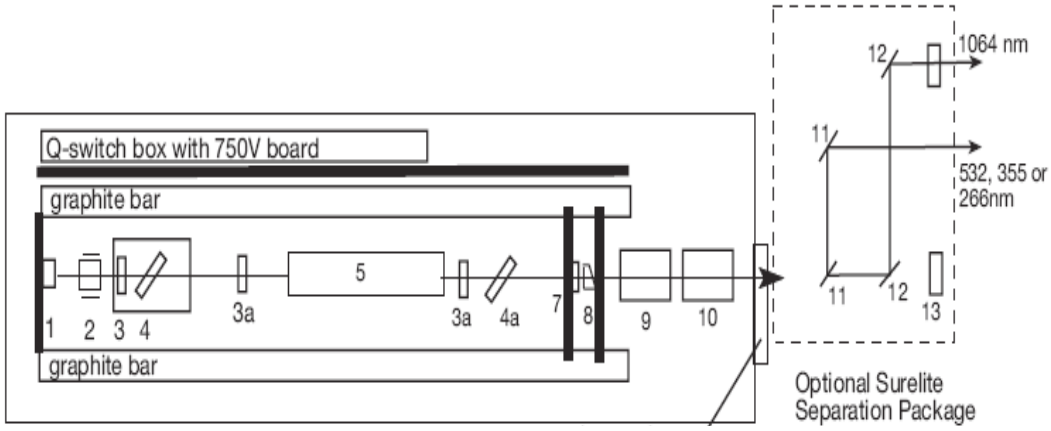

1. Rear mirror
2. Pockels cell
3. λ/4 plate
4. Dielectric polarizer
5. Flashlamp
6. Intra-cavity shutter
7. Mirror
8. Output beam compensator
9. Doupler
10.Tripler
11. Dichroics 532 nm, dichroics 355 nm
12. Dichroics 1.06

Figure 3.2: Cavity of the Surelite III (from Ref. 2).

Two commercial dye lasers (Radiant Dye, Narrowscan)[3] are used in the experimental set-up. Generally they can cover the emission spectra in the range between 320-750 nm using different solutions of organic substances (Coumarine or DCM in methanol are the most common dyes used in our experiment). The optic cavity incorporates: an output coupler (OC), a first cell (C1), the double grating (G) and beam expander (BE) (Figure 3.3). The first cell where the dye circulates is used for the oscillation and preamplifier stage. The two telescopes (L5, L6) after the grating focus the beam to the second cell (C2) which is used for the amplifier stage. The concentration of dye passing though the second cell is three times less than the one in first cell.

The two lasers have different properties. One laser has the resonator consisting of two gratings (90 mm long, 3000 lines mm^{-1}): one is used in grazing incidence and the other in Littrow order. Both gratings are illuminated through the prism expander to achieve a bandwidth of 0.04 cm^{-1}. This laser (first laser) is used to promote the excitation to the intermediate state S_1 of the molecular system under study. The second laser only has 2400 lines mm^{-1} grating and is used for the ionisation stage.

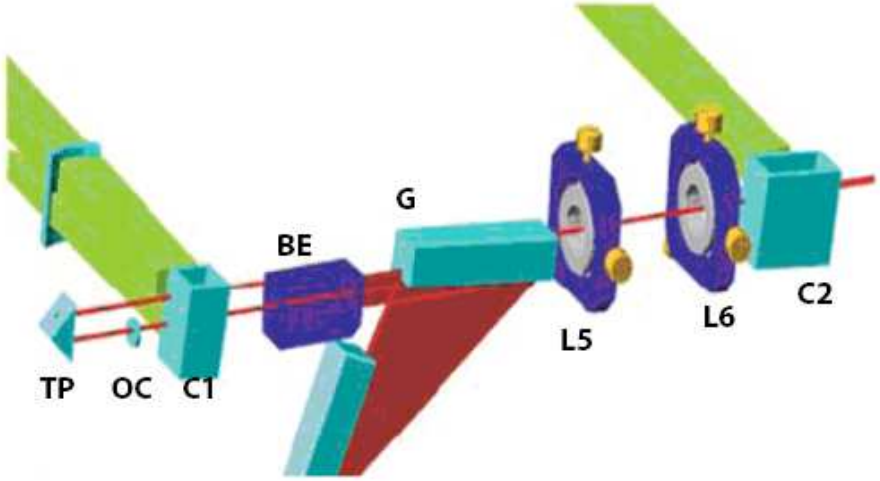

TP 180º Turning prism
C1 First Cell
G Grating
C1 Second Cell
OC Output Coupler
BE Beam expander
L5, L6 Telescope lenses

Figure 3.3: Optic cavity of the dye laser (from Ref.3).

The visible output (fundamental) of the dye lasers is frequency doubled using a non-liner crystal (Second-Harmonic Generation, SHG). To achieve optimum conversion efficiency the phase velocities of the fundamental and second harmonic have to be equal (phase matching):

$$h\upsilon_2 = h2\upsilon_1 \qquad [3.1]$$

$$\vec{k}_2 = \vec{k}_1 + \vec{k}_1 \Rightarrow (2\pi/\lambda_2)/n\upsilon_1 \qquad [3.2]$$

$$n(2\upsilon_1) = n(\upsilon_1) \qquad [3.3]$$

where k_1 and k_2 are the wave vectors, υ_1 and υ_2 are the refractive indexes. This occurs at a certain wavelength-dependent angle to the optical axis of the crystal. There are therefore two possible approaches to connect the tuning angle of the non-linear crystal with a certain wavelength of the resonator: the auto-tracker method and look-up tables.

The auto-tracker system automatically adjusts the phase matching angle to optimize the output energy. The principle used is the distortion of the beam shape once the optical non-linear process is no longer in the optimal phase matching condition. The distortion can be measured (usually with detection by photodiodes) and utilized to generate an error signal which is fed forward to the stepper motor driver controlling the crystal. Thus the crystal is rotated simultaneously and automatically while the laser is scanning. This method is particularly suitable for slow scans or fixed wavelength operation. Auto-tracking can be applied in both dye lasers using two different softwares. One auto-tracker controller is included in the Narrowscan dye laser (second laser) software which also controls the other laser functions. The other software is home made[4] (it is used for the first laser).

The look-up table is an alternative approach for the control of the tuning angle of the non-linear crystal. This method is particularly useful for fast scans. The look-up table is generated before any scan is performed. The stepper motor positions relative to certain wavelengths are stored in the software and used during the scan. The software able to apply this method is only installed in the second laser controller. The fundamental is separated from the second harmonic with a UG5 (schott) filter or a pellin–broka separation unit. Typical frequency doubled outputs of 0.5 mJ to 1 mJ are obtained for BBO crystals and 5 to 10 mJ for KDP crystals.

3.3 Vacuum chamber and molecular beam source

The vacuum consists of two stages pumped differentially with a system of two large pumps and one small pump. The first chamber hosts the gas inlet system and it is connected to the main chamber via a skimmer (height 45 mm, diameter 1.5 mm) which selects only a collimated and coolest part of the gas expansion. The second chamber consists of the analyser and the drift tubes for electrons and ions. The vacuum in the first chamber is maintained by 1400 l/s turbo-molecular pump (Pfeiffer Balzer, TPU 1500); a 1100 l/s turbo-molecular pump (Pfeiffer, TMU 1600) is located in the main chamber. A third small pump (330 l/s turbo molecular pump Pfeiffer Balzer, TPU 380) is used in the RE-TOF. The pre-vacuum necessary to support the turbo molecular pumps is obtained with a 35 m^3 h^{-1} two-stage rotary-vane pump (Pfeiffer, DUO 35). Normally a total pressure of 1×10^{-7} mbar is achieved without the valve in operation, under valve operation, this rises to ~5×10^{-5} mbar in the pre-chamber and ~5×10^{-7} mbar in the main chamber.

The sample under study is introduced into an internal sample holder located directly behind the valve (General Valve mounted inside the pre-chamber on a XYZ rotation manipulator) and expanded in a supersonic jet though a nozzle aperture of 20-800 μm. The sample can be heated using a temperature controlled thermocouple to achieve a significant vapour pressure. All the gas cylinders containing the carrier gases (usually neon or argon) are connected to a mixing bottle where additional mixtures of gas can be made. A backing pressure between 1-8 bar can be adjusted to obtain the best experimental conditions for the various molecular clusters.

3.4 Analyser, reflectron and micro-channels plates

Figure 3.4 shows a schematic representation of the analyser which is located in the main vacuum chamber and is shielded by a mu-metal tube against external electric and magnetic fields. It consists of two parts: the electron and the ion optics. The two copper meshes (70 lines $inch^{-1}$, transmission 90%) are separated by 30 mm and delimitates the ionisation region where the laser beams are perfectly perpendicular to the collimated molecular beam. The electrical pulses are applied independently to the meshes to extract ions or electrons.

The ions are repelled and accelerated perpendicular to the laser and molecular beam by applying a positive voltage (~900 V) onto the ion repeller. A voltage is applied to the capacitor to compensate the velocity component of the ions perpendicular to the extraction direction, which originates from the jet velocity.

Two different approaches can be used to apply the voltage onto the capacitor. The first approach consists of applying a homogeneous and constant voltage (usually between 1-5 V). In this case the voltage is proportional to the mass of the ions under study as shown in Figure 3.5. Table 3.1 shows how the voltage changes in the case of the phenol…Ar_n clusters. In the second method,[5] a linearly increasing voltage triggered by the extraction pulse is used. The compensation is achieved for all masses by applying 0.4 V/μs.

The ions are focussed with a constant voltage of ~500 V applied to the ion lens and then reflected through a RE-TOF. It consists of a 2 cm long breaking and 13 cm long

reflecting region. By optimisation of the ratio of breaking and reflecting voltages (typically U_{break}=450 V, U_{ref}=990V), a TOF width of 80 ns can be achieved.

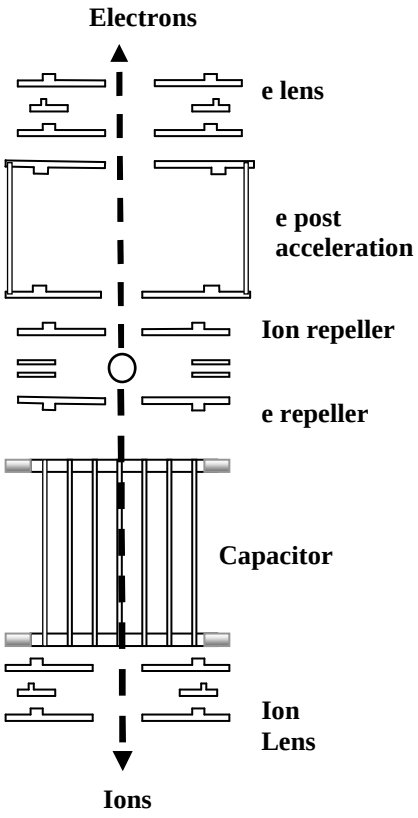

Figure 3.4: Schematic of the analyser.

Table 3.1: Static voltage applied onto the capacitor with the increase of the cluster masses for phenol…Ar_n clusters.

Number of Argon atoms in Phenol…Ar_n	**Voltage Capacitor /V**
0	1.90
1	2.30
2	2.70
3	3.20
4	4.00
5	4.50

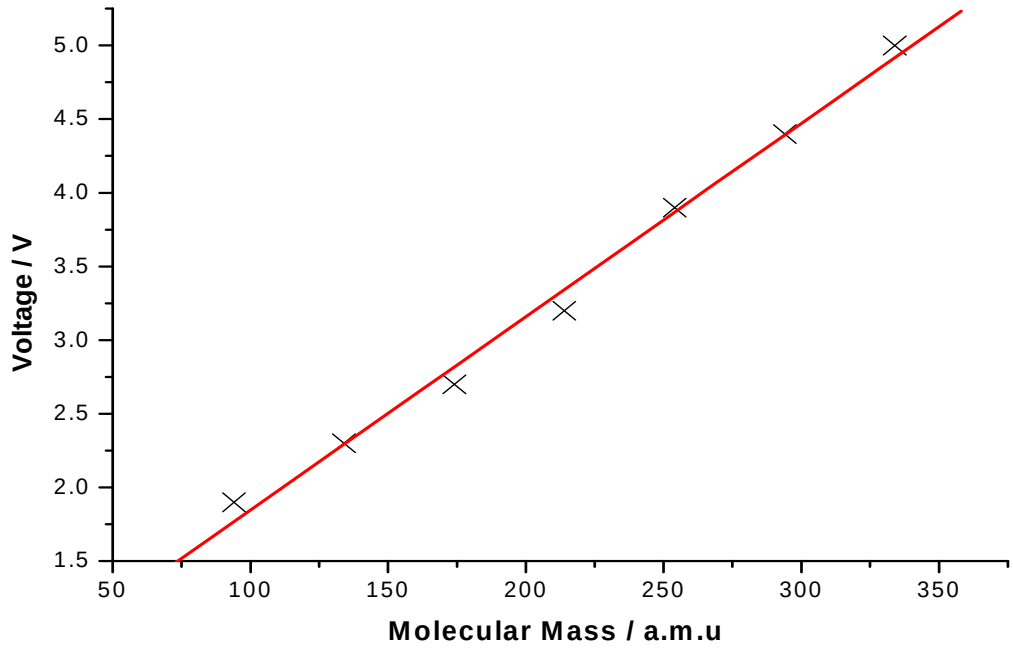

Figure 3.5: Voltage applied onto the capacitor as a function of the molecular mass.

A pulse or a pulse sequence for ZEKE and MATI experiments is produced by home-built pulse pattern generator[6] (the schematic circuit and the blocks diagram are reported in Figure 3.6 and 3.7 respectively). The pulse or the pulses sequence is applied to the

electron repeller which consists of one gold mesh and two additional rings set to the appropriate voltages.

The electrons are post accelerated in a 40 mm long cylinder which has a gold mesh on its entrance and 15 mm diameter pinhole at its exit. The ions and electrons are detected on micro-channel plates (40/15, Galileo Electro Optics Corp, active area diameter 41 mm diameter, channel diameter 10 μm).

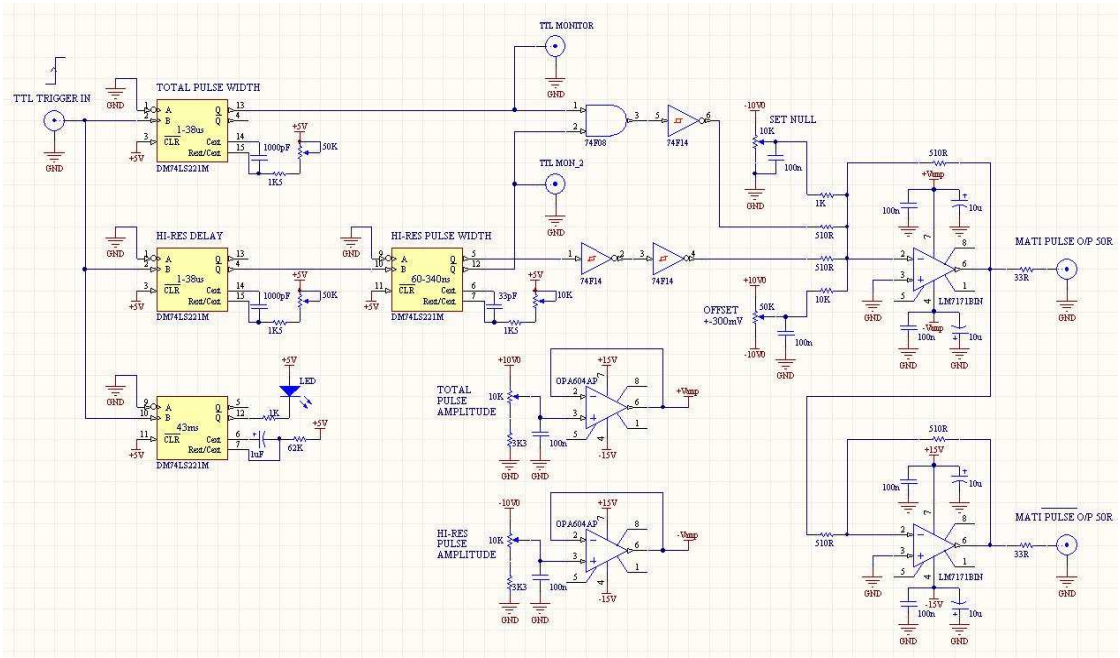

Figure 3.6: Schematic circuit for the pulse pattern generator.

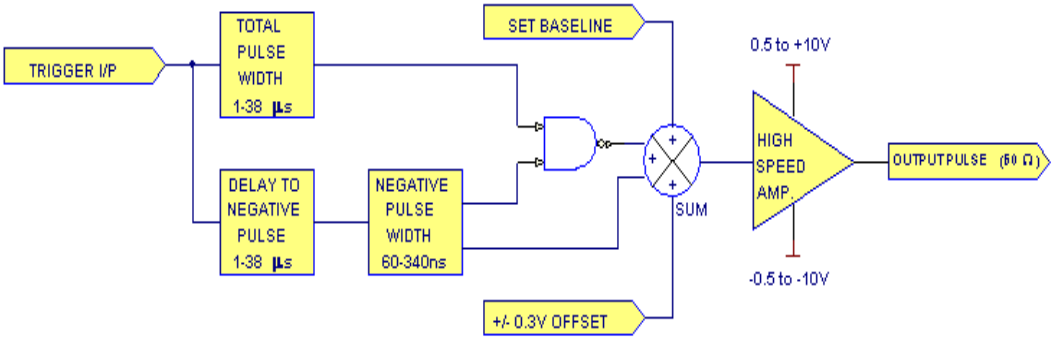

Figure 3.7: Blocks diagram for the pulse pattern generator.

3.5 Timing, system control and data acquisition

Experiments are usually run at a repetition rate of 10 Hz. A digital delay generator is used to produce delayed TTL pulses of a variable width which trigger individual devices. The overall timing of the experiments is shown schematically in Figure 3.8

The valve is triggered first to allow enough time for the molecular beam to travel to the ionisation region. After a delay of around 700 µs, a trigger is applied to the laser and after a short delay extraction pulses for either ions or electrons are applied to the corresponding plates. The signal detected on the MCP is averaged and digitised in an oscilloscope (LeCroy LT 354). The use of a home-made software permits control of all the data acquisitions and the whole process to scan the two dye lasers. Averaged signals are stored together with the current laser wavelength.

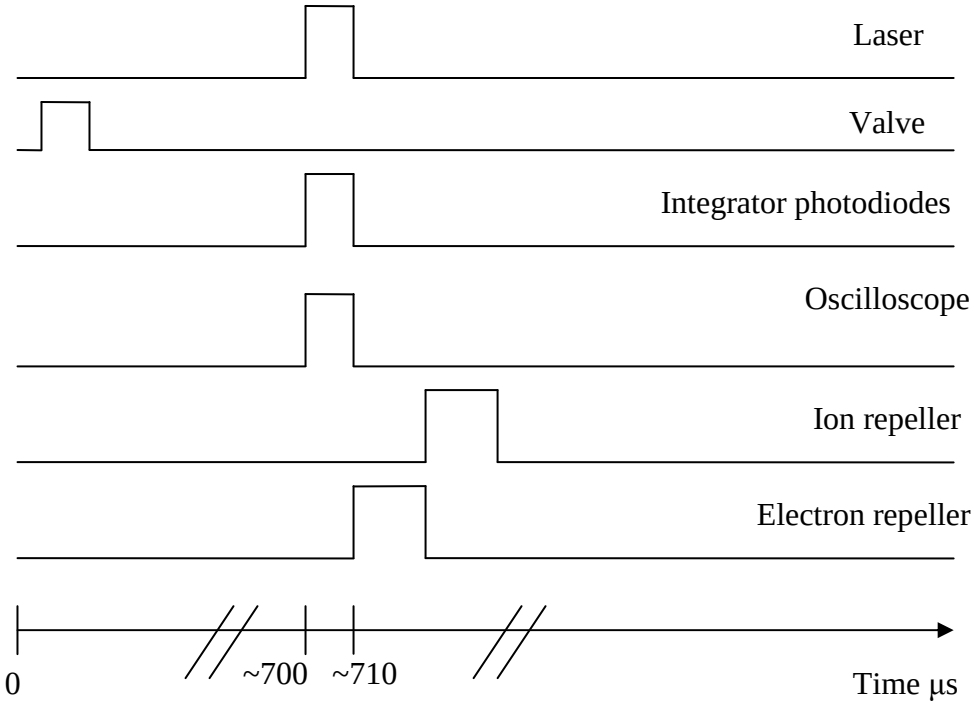

Figure 3.8: Typical timing sequence for the experiment.

3.6 References

[1] Software built by Dr M. Benyezzar (unpublished description).

[2] Continuum Surelite-III, Catalogue and instruction manual.

[3] Radiant Dyes NARROWscan, Catalogue and instruction manual.

[4] Software built and developed by Dr M. Benyezzar (unpublished description).

[5] Robert Baumann, *Dissertation*, TU München 1988.

[6] M. Benyezzar and M. Needham, poster presentation, PSI Open Day 20 Jan. 2010 and private communication (M. Benyezzar).

Chapter 4

Phenol…Ar_2: Ionisation energy and vibrational frequencies

4.1 Introduction

A variety of van der Waals complexes of mono-substituted benzene molecules with argon have been investigated in their neutral electronic ground and excited states (S_0, S_1) state as well as the cation ground state (D_0) by REMPI spectroscopy and the two equivalent spectroscopic methods for the investigation of threshold ionisation, (MATI and ZEKE) spectroscopy. Previous examples of $A^{(+)}…Ar_n$ clusters with aromatic molecules include A = benzonitrile,[1,2] fluorobenzene[3,4] and aniline. [5,6]

Phenol is another fundamental mono-substituted benzene molecule with an electron donor group (OH) and two principle binding sites for neutral ligands. One interaction can be established with the substituent by the formation of a hydrogen bond to the OH group and the other binding motif corresponds to a van der Waals interaction with the aromatic π-electron system.

A large numbers of spectroscopic investigations supported by computational methods provide information on the phenol…Ar_n structures ($n \leq 2$) in the S_0, S_1, and D_0 electronic

states. REMPI,[7] infrared (IR)[8] and Raman[9] spectroscopy suggested that π-bonding between Ar and phenol is the only possible interaction motif in the neutral S_0 and S_1 states. Recent high-level *ab initio* quantum chemical calculations[10] also support a π-bonded global minimum, whereas the H-bound structure is only a transition state in the S_0 state. Hole-burning spectroscopy of phenol…Ar_n with *n*=1 and 2 demonstrated that only one isomer is present in the molecular beam expansion.[11] Subsequent high-resolution rotationally resolved laser induced fluorescence spectra have confirmed that phenol…Ar and phenol…Ar_2 have π-bonded equilibrium structures, with Ar atoms located at opposite sides of the aromatic ring.[12]

MATI[13], ZEKE,[14] PIE,[15] and IR[16] spectroscopy are consistent with a π-bonded phenol$^+$…Ar structure also in the cation ground state. In contrast, the IR photodissociation spectrum of phenol$^+$…Ar generated in an electron impact (EI) ion source[17] shows that the most stable isomer in the D_0 state has a H-bound geometry, in line with *ab initio* calculations.[10,18,19] This has been interpreted by the fact that resonant photoionisation of the π-bonded neutral phenol…Ar precursor complex can generate only the π-bonded structure in the cation due to the Frank-Condon-Principle. Electron impact ionisation does not have such a restriction and can produce the most stable H-bound structure in the cation. The fact that in the cation state, the H-bound structure is more stable than the π-bonded isomer implies that a π→H switch in the preferred binding motif could be induced by ionisation.[20] This ionisation-induced π→H switching reaction has recently been monitored in real time for phenol$^+$…Ar_2 by picosecond pump-probe IR spectroscopy. [16,21] Ionisation of phenol…Ar_2(2π) with two π-bonded ligands triggers a dynamical process, in which one Ar atom isomerises from the π -bound site toward the H-bound site on a time scale of few picosecond, with a barrier of

less than 100 cm^{-1}. In this Chapter, the MATI spectra of phenol…Ar_2 (2π) recorded *via* different intermediate S_1 levels involving various degrees of intermolecular vibrational excitation is reported discussing the intermolecular vibrational assignment in the cation ground state, which indicates a significant geometrical change upon ionisation.

4.2 Results

4.2.1 REMPI spectrum

A (1+1') REMPI spectrum was recorded as the first step preceding the investigation of the ion ground state by MATI spectroscopy.

Phenol…Ar_2 clusters were produced in a skimmed supersonic jet expansion of phenol seeded in argon gas at a backing pressure of 2 bar. The sample was heated to 320-340 K. The excitation and ionisation steps of the clusters were performed using Coumarin 153 as a dye for the first laser (excitation) and a mixture of Sulfurhodamine B and DCM for the second laser (ionisation). The laser frequencies were calibrated (±0.02 cm^{-1}) against the simultaneously recorded iodine absorption spectrum. A two-photon, two-color (1+1') REMPI spectrum was recorded, employing a fixed frequency of 32210 cm^{-1} for the ionising laser in order to ensure soft ionisation and reduce fragmentation from higher clusters. The (1+1') REMPI spectrum of phenol…Ar_2 is shown in Figure 4.1, which is in good agreement with previous studies,[11,14] but with a large improvement in the signal-to-noise ratio. The most intense feature in the spectrum at 36282.2±0.5 cm^{-1} is assigned to the S_1 origin. The additional bands are attributed to vdW vibrational levels. A summary of the frequencies observed in the REMPI spectrum and their assignment according with the hole burning studies of phenol…Ar_2[11] are reported in Table 4.1. Figure 4.2 illustrates a schematic representation of the six

possible intermolecular modes of phenol…$Ar_2(2\pi)$, which have been deduced through comparison with the calculated intermolecular modes of the π-bound phenol…Ar cluster.[11] They are symmetric and antisymmetric linear combinations of the intermolecular stretch (s_{zs} and s_{za}), and bend along both the x and y direction (b_{xs}, b_{xa}, b_{ys}, b_{ya}).

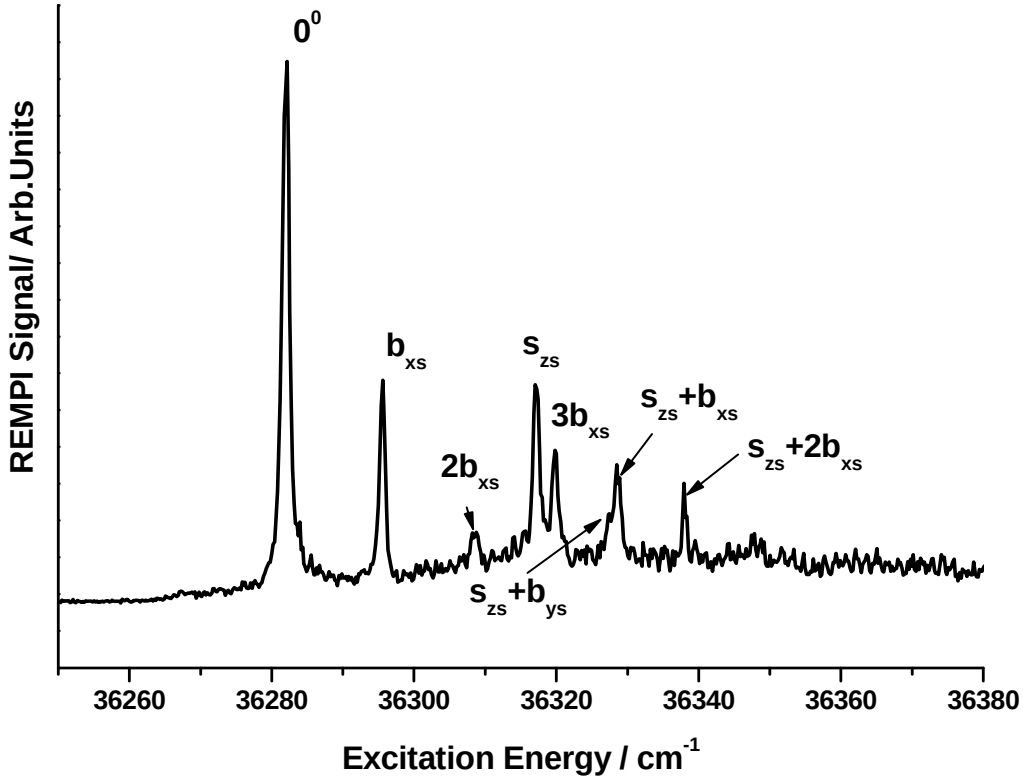

Figure 4.1: (1+1') REMPI spectrum of phenol…$Ar_2(2\pi)$ of the first electronically excited S_1 state. The assignment of the van der Waals modes is included (Table 4.1).

Table 4.1: Frequencies and assignment of the vibrational bands observed in the REMPI spectrum of phenol…$Ar_2(2\pi)$.

Frequency (cm^{-1})	Assignment
14	b_{xs}
27	$2b_{xs}$
36	s_{zs}
39	$3b_{xs}$
46	$s_{zs}+b_{ys}$
47	$s_{zs}+b_{xs}$
57	$s_{zs}+2b_{xs}$

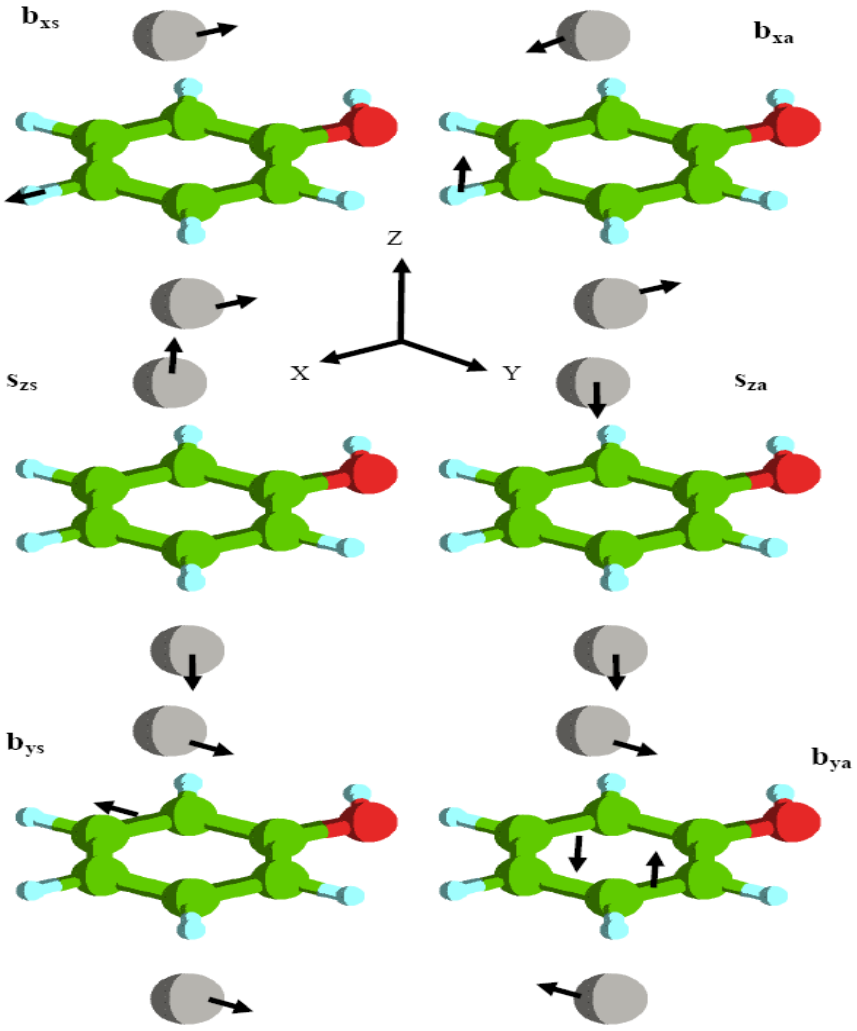

Figure 4.2: Intermolecular normal modes of phenol $^{(+)}$…$Ar_2(2\pi)$. The displacement arrows are schematic and do not indicate displacement magnitudes.

4.2.2 MATI spectra

The MATI spectra were obtained by fixing the pump laser to a suitable intermediate S_1 vibronic state, while the second laser was scanned through successive ionisation thresholds to populate long-lived high-*n* Rydberg states. The prompt photoions produced directly by the laser pulse were separated from the Rydberg states by a 0.5 μs delayed offset field of 1-3 V/cm. After a further delay of 10-20 μs, a high-voltage pulse ~300 V/cm is applied to field-ionise the long-lived Rydberg states and to extract both the spontaneous and MATI ions into the reflectron mass spectrometer.

Figure 4.3 shows the MATI spectrum of phenol$^+$…$Ar_2(2\pi)$, which was obtained *via* the $S_1 0^0$ intermediate state. The weak feature at a total photon energy of 68288±5 cm^{-1} is assigned to the field-free ionisation energy (IE) of phenol…$Ar_2(2\pi)$ and taken as zero internal energy. In addition, an almost harmonic progression with nearly equal spacing of 10 cm^{-1} is observed (Table 4.2). The IE value is confirmed by the MATI spectrum recorded via the $S_1 b_{xs}$ vibrational state (Figure 4.3). In this spectrum the origin of the D_0 state (IE) appears with much higher intensity than in the spectrum recorded via the $S_1 0^0$ state. This spectrum also displays a progression with spacing of 10 cm^{-1} but with different Franck-Condon intensities. This progression can be divided in two parts with rising and falling intensity of the observed modes. In the first part at low energy the peaks are clearly separated, while they are partially overlapped in the second part, probably due to enhanced spectral congestion. As it will be explained below, these peaks are attributed to the b_{xs}^n van der Waals modes. The progression can be observed up to *n*=8 (Table 4.3).

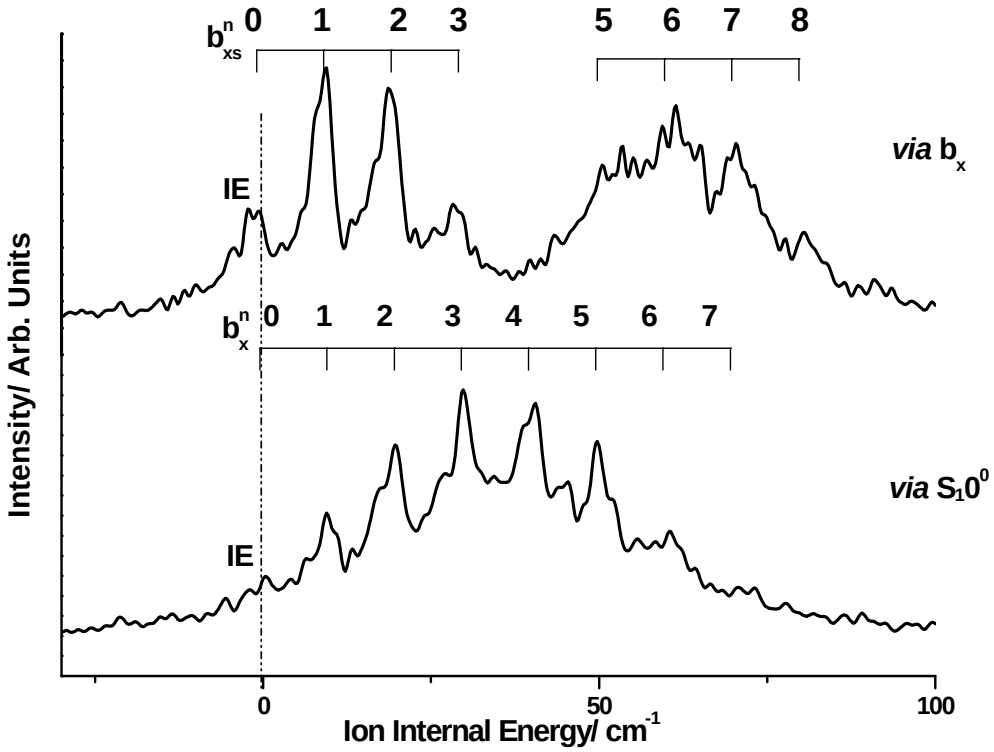

Figure 4.3: MATI spectra of phenol$^+$…Ar$_2$(2π) *via* the $S_1 0^0$ (bottom) and the $S_1 b_{xs}$ (top) intermediate states.

Table 4.2: IE and vibrational frequencies observed in the MATI spectra of phenol$^+$…Ar$_2$(2π) *via* the $S_1 0^0$ and $S_1 b_{xs}$ states (Figure 5.3).

	frequency (cm^{-1})	
Assignment	*via* $S_1 0^0$	*via* $S_1 b_{xs}$
b_{xs}	9	9
$2b_{xs}$	20	19
$3b_{xs}$	30	29
$4b_{xs}$	40	
$5b_{xs}$	50	50
$6b_{xs}$	61	61
$7b_{xs}$	71	71
$8b_{xs}$		81

The assignment of the b_x^n van der Waals progression in the MATI spectra *via* the $S_1 0^0$ and $S_1 b_x^1$ states are confirmed by fitting the experimental intensities to those obtained using one-dimensional harmonic Franck-Condon simulations. Figure 4.4 compares the observed and calculated transition intensities in the MATI spectra *via* the $S_1 0^0$ (a) and $S_1 b_{xs}^1$(b) states. The transition intensities were obtained by Franck-Condon factors based on harmonic vibrational wavefunctions. The calculated intensities were fit to the observed intensities in the MATI spectrum *via* the $S_1 0^0$ state by adjusting a displacement parameter to DL=0.84, which represents the shift of the potential minima in going from S_1 to the D_0 state in the ion. With the same value of DL=0.84, the intensity distribution *via* $S_1 b_x^1$ is well reproduced by the calculated Franck-Condon factors. In particular, the intensity maxima for *n*=2 and 6 and the minimum at *n*=4 are nicely recovered by the simulations. The consistent reproduction of the intensity distribution in the b_{xs}^n progression confirms the vibrational assignments. The calculated intensities are slightly stronger for higher vibrational levels, such as *n*=5-7. This observation may arise from a non-radiative channel, such as dissociation, which opens for the higher vibrational levels, or from limitations to the one-dimensional harmonic Franck-Condon approximation.

Figure 4.5 shows the MATI spectra recorded *via* the s_{zs} and $3b_{xs}$ intermediate states. The IE origin of the ionic ground state cannot be observed, and both spectra are characterized by a broad unresolved structure with a maximum at around 75 cm^{-1} internal energy. Even broader structures are observed in the MATI spectrum recorded *via* $s_{zs}+b_{xs}$ as shown in Figure 4.5.

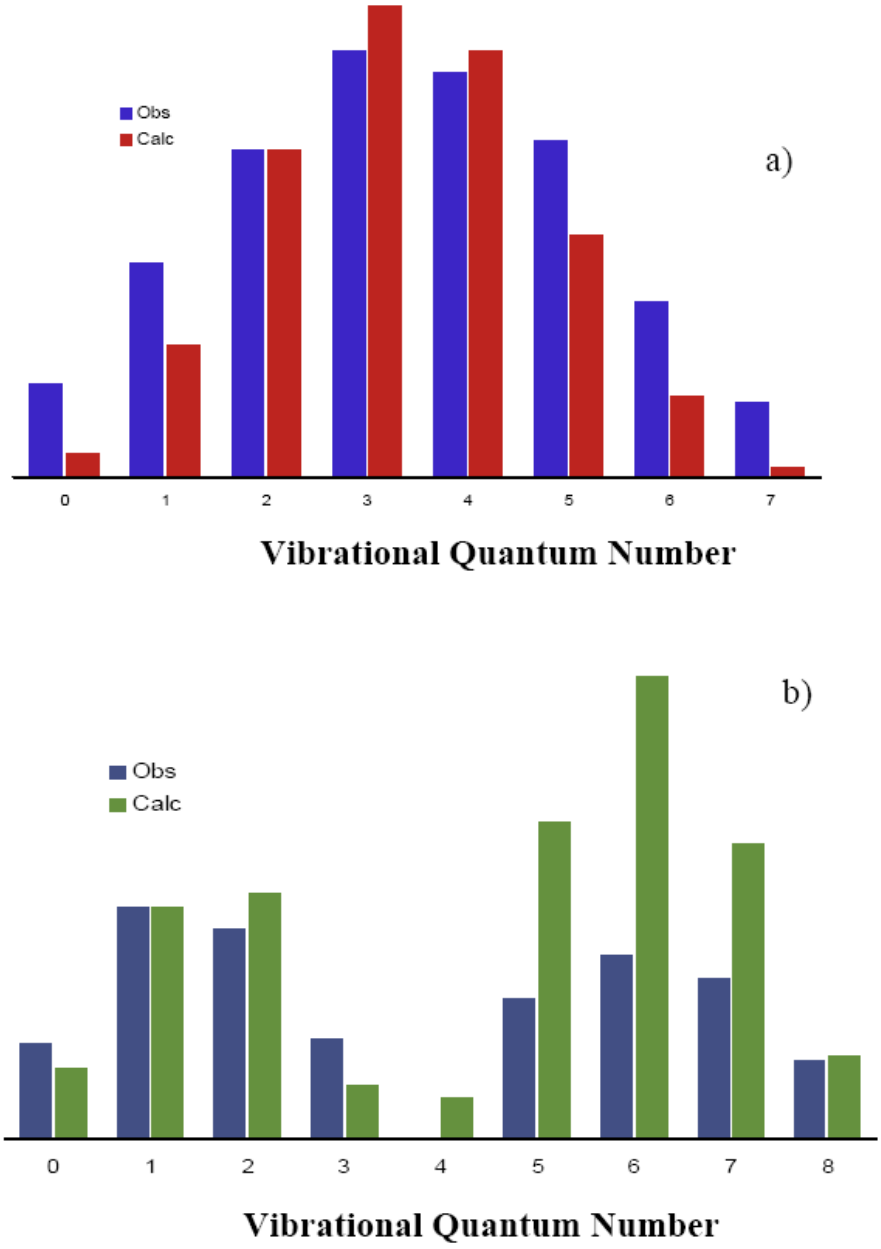

Figure 4.4: Observed and calculated transition intensities of the b_{xs}^{n} progression in the MATI spectra *via* the $S_1 0^0$ origin (a) and the $S_1 b_{xs}^{1}$ state (b).

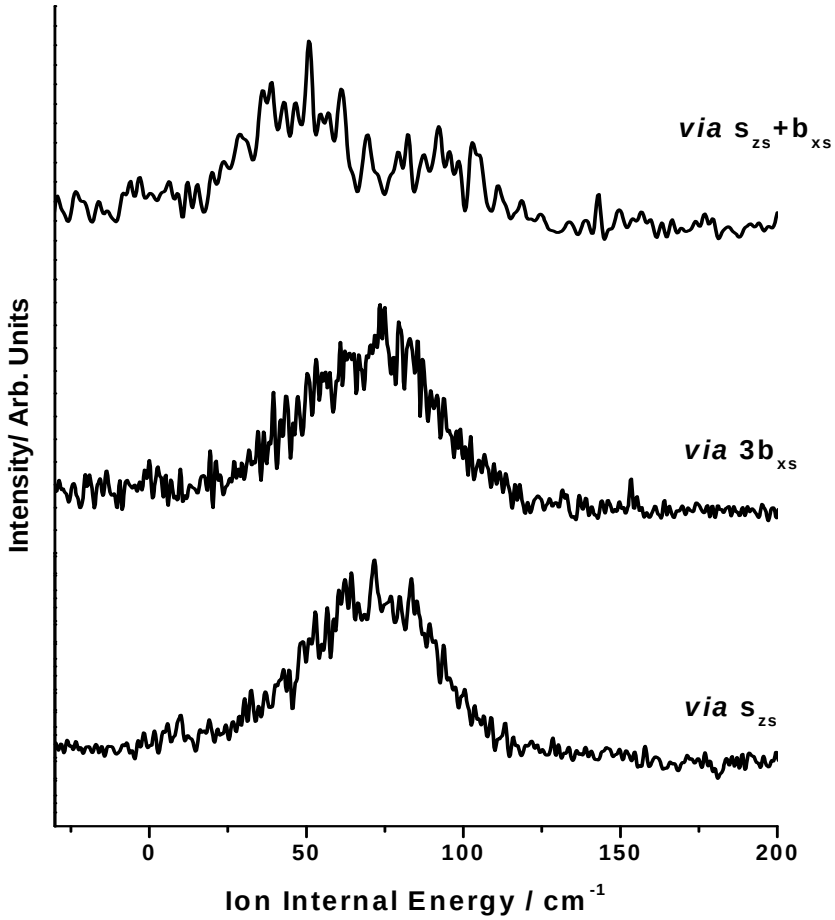

Figure 4.5: MATI spectra of phenol^{+}…Ar$_2$(2π) *via* the s_{zs}, $3b_{xs}$, and s_{zs} +b_{xs}, intermediate states.

4.3 Discussion

4.3.1 Vibrational modes assignment in the S_1 state

To support the vibrational modes assignment, calculations were performed for the S_0 state using the TURBOMOLE package version 5.10.[22] The geometry optimization was performed at the resolution-of-identity second–order Møller-Plesset perturbation theory (RI-MP2). To obtain reasonable geometries, the cc-pVTZ basis set which offers a good accuracy for geometries convergence was used. Diffuse function (aug-) were added to recover the long-range dispersion interactions between the phenol and Ar atoms moieties. In particular, it has been found that performing the same level of calculations

without diffuse function strongly underestimates the long range interactions consequently affecting the length of the vdW bonds. To improve these calculations, counterpoise corrections could be included to avoid basis set superposition error (BSSE). However, this requires additional very high computational cost (for the three moiety system, each counterpoise correction process involves seven individual energy calculations). An analytical procedure of the determination of vibrational frequencies is not implemented for the RI-MP2 method in the Turbomole package; therefore the numerical procedure for evaluation of the vibratioanl frequencies was used. The vibrational-frequency calculations were executed using the NumForce part of the Turbomole 5.10 package. The validity of the calculated geometries has been verified by the fact that no imaginary vibrational mode frequencies have been found for each structure.

The calculated frequencies listed in Table 4.3 confirm the assignment for b_{xs} and s_{zs}, with experimental/theoretical values of 14/12 and 36/30 cm^{-1}, respectively.

Table 4.3: Intermolecular vibrational modes and frequencies in the S_0 state of phenol…$Ar_2(2\pi)$ calculated at the RI-MP2 level.

mode	frequency (cm^{-1})
b_{xs}	12
b_{ys}	14
b_{xa}	25
s_{zs}	30
b_{ya}	44
s_{za}	45

4.3.2 Ionisation Energy

The IE value can conclusively be assigned as 68288±5 cm^{-1} by taking the first band in the MATI spectra obtained *via* $S_1 0^0$ and *via* $S_1 b_{xs}$. Although the intensity of the IE band as the first member of the b_{xs}^n progression is weak, comparison with the very similar ZEKE spectra of fluorobenzene$^+$…$Ar_2(2\pi)$ supports this assignment [3]. In the case of fluorobenzene$^+$…Ar_2, a one-dimensional Franck-Condon simulation confirmed the intensity distribution of the b_{xs}^n progression and the assignment of the *n* quantum number to the individual vibrational transitions, including *n*=0 for the IE band.

The IE of phenol$^+$…$Ar_2(2\pi)$ is red-shifted by 340 cm^{-1} from the IE of phenol$^+$.[23] This shift is almost twice the red-shift for the phenol$^+$…Ar(π)) cluster (176 cm^{-1}). This observation indicates the similarity of the intermolecular bonding type in phenol$^{(+)}$…Ar(π) and phenol$^{(+)}$…$Ar_2(2\pi)$. This relationship reflects the same trend as was already observed in the case of aniline$^{(+)}$…$Ar_n(n\pi)$[6] and fluorobenzene$^{(+)}$…$Ar_n(n\pi)$ [3] with $n \leq 2$, where the additivity rule also holds almost strictly(ΔIE= -111 (*n*=1) and -219 (*n*=2) cm^{-1} for aniline, and ΔIE=-223 (*n*=1) and -422 (*n*=2) cm^{-1} for fluorobenzene).

4.3.3 Vibrational modes: interpretation in cationic state

The structure of the progression with a spacing of 10 cm^{-1} observed in the MATI spectrum *via* the $S_1 0^0$ state of phenol…$Ar_2(2\pi)$ is similar to those seen in aniline$^+$…$Ar_2(2\pi)$,[6] benzonitrile$^+$…$Ar_2(2\pi)$,[2] and fluorobenzene$^+$…$Ar_2(2\pi)$.[3.] The vibrational spacing was found to be 9 cm^{-1} for the case of benzonitrile and fluorobenzene, and 11 cm^{-1} for aniline. In all these A^+…$Ar_2(2\pi)$ clusters the fundamental mode of these progressions was assigned to the symmetric bending mode, b_{xs}. In analogy, the vibrational progressions in the MATI spectra of phenol$^+$…$Ar_2(2\pi)$

via $S_1 0^0$ and $S_1 b_{xs}$ are also assigned to b_{xs}^n. This interpretation supports the b_{xs} assignment in the S_1 state, because the MATI spectrum *via* $S_1 b_{xs}$ displays also a progression of the b_{xs}^n mode but with different Franck-Condon intensities.

The MATI spectrum of phenol$^+$…Ar(π) *via* the $S_1 0^0$ state shows a harmonic progression in b_x^n (15, 31, 46 cm^{-1} for n=1-3). The ratio of b_x/b_{xs} observed in phenol$^+$…Ar$_n$($n\pi$) for (n=1)/(n=2) of 15/10 is similar to the case of isoelectronic aniline (16/11). These ratios are a bit larger than those observed for fluorobenzene and benzonitrile (12/9). The b_x and b_{xs} assignments for phenol$^+$…Ar$_n$($n\pi$) with n=1 and 2 can be further confirmed by considering the following simple model. The reduced mass μ_{bx} and μ_{bxs} for the vibrational modes b_x and b_{xs} are given by the equations 4.1 and 4.2,

$$\mu_{bx}=(1/mR_0^2+1/MR_0^2+1/I_{yy})^{-1} \quad [4.1]$$

$$\mu_{bxs}=(1/mR_0^2+2/MR_0^2)^{-1} \quad [4.2]$$

where M and m are the masses of phenol and Ar respectively, I_{yy} is the moment of inertia (y axis) of phenol, and R_0 is the equilibrium distance between phenol and Ar. The frequencies ν_{bx} and ν_{bxs} of the b_x and b_{xs} modes are then given by equation 4.3 and 4.4,

$$\nu_{bx}=(1/2\pi)(k_{\Phi\Phi}^{bx}/\mu_{bx})^{1/2} \quad [4.3]$$

$$\nu_{bxs}=(1/2\pi)(k_{\Phi\Phi}^{bxs}/\mu_{bxs})^{1/2} \quad [4.4]$$

where $k_{\Phi\Phi}^{bx}$ and $k_{\Phi\Phi}^{bx}$ are the force constants for the b_x and b_{xs} modes, respectively. The angle Φ represents the angle between the y axis and the vector connecting Ar and the ring centre (Figure 4.6). If the two force constants are equal, the ratio of the two bending frequencies is given by the equation:

$$\nu_{bxs}/\nu_{bx}=(\mu_{bx}/\mu_{bxs})^{1/2} \qquad [4.5]$$

For phenol$^+$…Ar(π) and phenol$^+$…Ar_2(2π) equation 4.5 holds very well if we use the values as listed in Table 4.4. For both sides of equation 4.5 we obtain 0.7, which means that the force constants $k_{\Phi\Phi}^{bx}$ and $k_{\Phi\Phi}^{bxs}$ are essentially identical, supporting again the vibrational mode assignments. The broad structures observed in the MATI spectra recorded *via* s_{zs}, $3b_{xs}$ and $s_{zs}+b_{xs}$,(Figure 4.4) do not give any further information on the vibrational modes in the the D_0 state of phenol$^+$…Ar_2(2π).

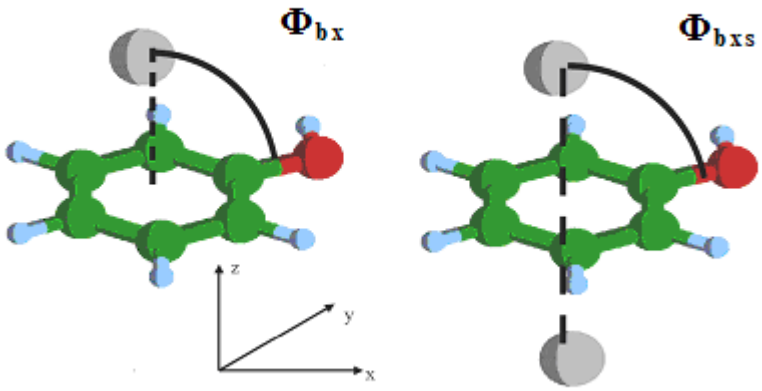

Figure 4.6: The angle between the y axis and the vector connecting Ar and the ring centre.

Table 4.4: Structural parameters, the calculated reduced masses and vibrational frequencies of the b_x and b_{xs} modes for phenol$^+$…Ar(π) and phenol$^+$…Ar$_2$(2π).

M (u)	94
m (u)	40
R_0 (Å) [19]	3.3
I_{yy} [24]	193
MR_0^2 (uÅ^2)	1024
mR_0^2 (uÅ^2)	436
μ_{bx} (u)	125
μ_{bxs} (u)	250
υ_{bx} (cm^{-1})	15
υ_{bxs} (cm^{-1})	10

4.4 Summary

The MATI spectra of phenol$^+$…Ar$_2$(2π) recorded via the different S_1 intermediate states were analyzed and the ionisation energy could be determined to be 68288±5 cm^{-1}. The observed progression in the MATI spectrum *via* the $S_1 0^0$ intermediate state shows a strong similarity with those of other mono-substituted benzene clusters with Ar (e.g., fluorobenzene, benzonitrile, aniline). The fundamental mode was assigned to the symmetric bending vibrational mode b_{xs} with a frequency of 10 cm^{-1}. The long progression in the b_{xs} mode indicates a large change of the geometry upon ionisation along this coordinate. The change in the vdW interaction energy upon the ionisation may be mainly due to the difference in the charge-charge induced–dipole interaction energy between the neutral ground state and the cationic ground state. Upon ionisation, the Ar atoms are more attracted towards the OH group of phenol due to the increase in positive charge on the C atom bonded to the OH group.[21,25]

4.5 References

[1] T. Kobayashi, K. Honma, O. Kajimoto and S.Tsuchiya, *J. Chem. Phys.,* 1987, **86,** 1111.

[2] M.Araki, S. Sato and K. Kimura, *J. Phys. Chem.,* 1996, **100,** 10542.

[3] H. Shinohara, S Sato and K. Kimura, *J. Phys. Chem. A*, 1997, **101,** 6736.

[4] G. Lembach and B. Brutschy, *J. Chem. Phys.*, 1997, **107**, 6156.

[5] E. J .Bieske, M. W. Rainbird, I. M. Atkinson and A. E. Knight, *J. Chem. Phys*., 1989, **91,** 752.

[6] M. Takahashi, H. Ozeki and K. Kimura, *J. Chem. Phys*., 1992, **96,** 6399.

[7] M. S. Ford, S. R. Haines, I. Pugliesi, C. E. H. Dessent and K. Müller-Dethlefs, *J. Electron. Spectrosc. Relat. Phenom.*, 2000, **112**, 231

[8] T. Ebata, A. Iwasaki and N. Mikami, *J. Phys. Chem. A*, 2000, **104**, 7974.

[9] G. V. Hartland, B. F. Henson, V. A. Venturo and P. M. Felker, *J. Phys. Chem.*, 1992, **96**, 1164.

[10] J. Cerny, X. Tong, P. Hobza and K. Müller-Dethlefs, *J. Chem. Phys*., 2008, **128**, 114319

[11] S. Ishiuchi, Y. Tsuchida, O. Dopfer, K. Müller-Dethlefs and M. Fujii, *J. Phys. Chem. A*, 2007, **111**, 7569.

[12] I. Kalkman, C. Brand, T. B. C. Vu, W. L. Meerts, Y. N. Svartsov, O. Dopfer, X. Tong, K. Müller-Dethlefs, S. Grimme and M.Schmitt, *J. Chem. Phys*., 2009, **130**, 224303.

[13] C. E. H. Dessent, S. R. Haines and K. Müller-Dethlefs, *Chem. Phys. Lett.*, 1999, **315**, 103.

[14] S. R. Haines, C. E. H. Dessent and K. Müller-Dethlefs, *J. Electron Spectrosc. Relat. Phenom.*, 2000, **108**, 1.

[15] N. Gonohe, H. .Abe, N. Mikami and M. Ito, *J. Phys. Chem.*, 2007, **89**, 3642.

[16] S. Ishiuchi, M. Sakai, Y. Tsuchida, A.Takeda, O. Dopfer, K. Müller-Dethlefs and M. Fujii, *J. Chem. Phys.*, 2007, **127**, 114307

[17] N. Solcá and O. Dopfer, *J. Phys. Chem. A*, 2001, **105**, 5637; N. Solcá and O. Dopfer, *Chem. Phys. Lett.*, 2003, **369**, 68.

[18] N. Solca, and O. Dopfer, *J. Mol. Struct.*, 2001, **563/564**, 241.

[19] J. Cerny, X. Tong, P. Hobza and K. Müller-Dethlefs, *Phys. Chem. Chem. Phys*., 2008, **10**, 2780.

[20] O. Dopfer, *Z. Phys. Chem*., 2005, **219**, 125.

[21] S.I. Ishiuchi, M. Sakai, Y. Tsuchida, A.Takeda, Y. Kawashima, M. Fujii, O.Dopfer and K. Müller-Dethlefs, *Angew. Chem., Int. Ed.* 2005, **44**, 6149.

[22] R. Ahlrichs, M. Bär, M. Häser, H. Horn and C. Kölmel. *Chem. Phys. Lett.* 1989, **162**, 165.

[23] G.Lembach, Diplomarbeit, Technische Universität München, 1994.

[24] E. Mathier, D. Welti, A. Bauder and Hs. H. Günthard, *J. Mol. Spectrosc.*, 1971, **37**, 63.

[25] X. Tong, S. Ullrich, C. E. H. Dessent and K. Müller-Dethlefs, *Phys. Chem. Chem. Phys.*, 2002, **4**, 3578.

Chapter 5

Dissociation energetics of phenol...Ar_2 cluster ion: The role of π→H isomeration

5.1 Introduction

The intermolecular fragmentation energetics and dissociation processes of van der Waals clusters have been an intense area of study. The first investigation on fragmentation process by using MATI spectroscopy were carried out by Krause and Neusser for benzene$^+$…Ar complex.[1,2]

The dissociation process of phenol$^+$…Ar(π) was also studied by means of MATI spectroscopy obtaining an accurate value for the dissociation energy for the loss of one Argon[3] atom of 535 cm^{-1} which is in agreement with the value determined by recent high-level *ab initio* calculations (D_0=542 cm^{-1}).[4]

Very surprising results have been recently observed analysing the dissociation energetics aniline$^+$…Ar_2. Gu and Knee[5] found a value of 380 ± 5 cm^{-1} for the dissociation threshold for the loss of one Argon atom from aniline$^+$…Ar_2. This value is substantial smaller than the value obtained for the dissociation energy of 495 cm^{-1} for

Aniline$^+$…Ar(π). The entire dissociation process was explained considering a $\pi \rightarrow$H isomerisation.

In the present Chapter, the energetics for the isomeration and dissociation processes of phenol$^+$…Ar_2 in the cationic ground state are investigated in detail using PIE and MATI spectroscopy.

5.2 Results

5.2.1 PIE spectra

The experimental conditions to produce the phenol…Ar_2 cluster to record the PIE/ MATI spectra are identical to those reported in the previous chapter.

Figure 5.1 shows the PIE spectra of phenol$^+$…Ar_n (n=0-2) obtained for resonant ionisation *via* the S_1 origin of phenol…$Ar_2(2\pi)$ at 36282.2 cm^{-1}.[6] The first step in the PIE spectrum of the phenol$^+$…Ar_2 parent occurs at a total photon energy of 68250±30 cm^{-1} and is assigned to the ionisation threshold of phenol$^+$…$Ar_2(2\pi)$. At approximately 400 cm^{-1} above the ionisation threshold the signal starts to significantly rise in the phenol$^+$…Ar fragment channel and provides a rough upper limit for the dissociation threshold for the loss of one Ar atom from phenol$^+$…$Ar_2(2\pi)$. The threshold at around 1180 cm^{-1} above the ionisation observed in the phenol$^+$ channel yields an upper limit for the dissociation energy for the loss of two Ar atoms from phenol$^+$…$Ar_2(2\pi)$. The observed threshold spectra are consistent with those reported in the previous work for n=1 and 2.[7]

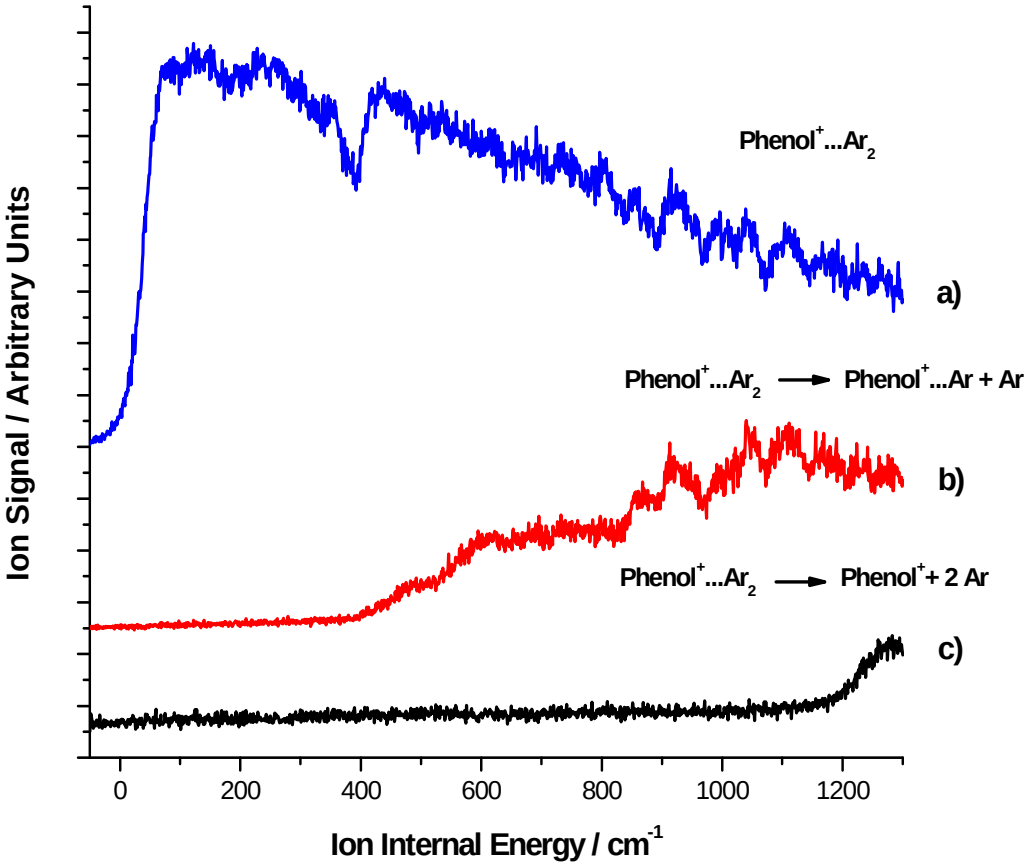

Figure 5.1: PIE spectra recorded in the phenol$^+$…Ar_2 parent (blue, a) and the phenol$^+$…Ar (red, b) and phenol$^+$ (black, c) fragment channels obtained *via* the $S_1 0^0$ origin of phenol…$Ar_2(2\pi)$.

5.2. 2 MATI spectra

For an accurate determination of the dissociation thresholds, MATI spectra have been recorded in the mass channels of phenol$^+$…Ar_2 (Figure. 5.2a) and the phenol$^+$…Ar fragment channel (Figure 5.2b) obtained for resonant ionisation *via* the S_1 origin of phenol…Ar_2. The first feature in the MATI spectrum recorded at the parent mass (indicated by an arrow in Figure 5.2a) appears at a total photon energy of 68288±5 cm^{-1} (taken as zero internal energy) and is assigned as the adiabatic ionisation energy (IE) of phenol$^+$…$Ar_2(2\pi)$. The band displays some vibrational fine structure, which is attributed to a progression of an intermolecular vibration with 10 cm^{-1} width. No intramolecular

vibration of phenol$^+$…Ar$_2$(2π) is detected in the MATI spectrum of the parent mass channel, implying that dissociation occurs in the very low energy range above the IE. This is quite different from phenol$^+$…Ar(π), where the dissociation energy of the cation occurs at 535 cm^{-1} above the IE, and various intramolecular vibrational modes can be observed in the MATI spectrum of the parent ion channel below this dissociation threshold. [3]

The spectrum recorded in the phenol$^+$…Ar daughter mass channel (Figure 5.2b) displays a series of broad bands in the higher energy range, displaying a similar intermolecular fine structure as the IE band in Figure 5.2a. The first signal appears at 210 cm^{-1} and provides an upper limit for the dissociation threshold for one Ar ligand from phenol$^+$…Ar$_2$(2π). The deviation from the threshold value of around 400 cm^{-1} derived from the PIE spectrum (Figure 5.1) and the binding energy of 535 cm^{-1} for phenol$^+$…Ar(π) will be discussed below. Signal in the phenol$^+$…Ar daughter mass channel can be detected up to an excess energy of ~1050 cm^{-1} above the IE, which gives a lower limit for the dissociation energy for the loss of the two Ar atoms from phenol$^+$…Ar$_2$(2π).

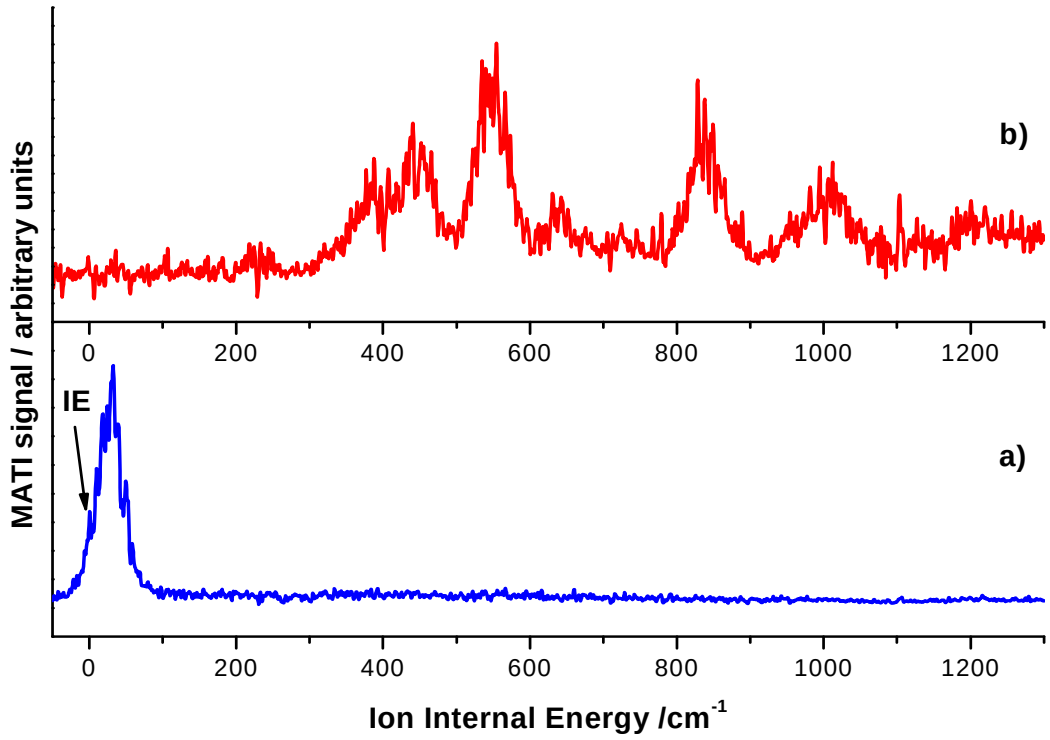

Figure 5.2: MATI spectra recorded in the phenol^{+}…Ar_2 parent (blue, a) and phenol^{+}…Ar fragment channels (red, b) obtained *via* excitation of the $S_1 0^0$ origin of phenol…$Ar_2(2\pi)$.

5.3 Discussion

5.3.1 IE and van der Waals vibrational structure

As already explained, the adiabatic IE of phenol…$Ar_2(2\pi)$ of 68288±5 cm^{-1} is red-shifted by 340 cm^{-1} from the monomer value of 68628 cm^{-1}, which is almost twice the red-shift observed for phenol…Ar(π) cluster (176 cm^{-1}). This observation indicates the similarity of the intermolecular bonding type in phenol$^{(+)}$…Ar(π) and phenol$^{(+)}$…$Ar_2(2\pi)$, and confirms once more the (1/1) structure of phenol…$Ar_2(2\pi)$. As mentioned above, the IE band displays vibrational fine structure attributed to intermolecular vibrations. The dominant features are assigned to a relatively harmonic progression of 6 quanta in the symmetric bending mode (b_{xs}), with a fundamental

frequency of ~10 cm^{-1}. Such progressions are commonly observed in the MATI/ZEKE spectra of $A^+…Ar_2(2\pi)$ (where A= aniline$^+…Ar_2(2\pi)$,[8] benzonitrile$^+…Ar_2(2\pi)$,[9] and fluorobenzene$^+…Ar_2(2\pi)$).[10] The fundamental frequency was found to be 9 cm^{-1} for the case of benzonitrile and fluorobenzene, and 11 cm^{-1} for aniline.

6.3.2 Intramolecular vibrational modes

Intramolecular vibrations of phenol$^+…Ar_2(2\pi)$ are only observed in the MATI spectrum recorded in the phenol$^+…$Ar fragment mass channel. Similar to the IE band, all intramolecular vibrational transitions occur in combination with the intermolecular vibrational structure, leading to a certain amount of spectral congestion. Figure 5.3 compares the MATI spectrum of phenol$^+…Ar_2(2\pi)$ recorded in the phenol$^+…$Ar channel with the MATI spectrum of bare phenol$^+$ as a function of the ion internal energy. Table 5.1 lists the observed bands in phenol$^+$ and phenol$^+…Ar_2$, along with their assignment.[11] As the frequencies of most intramolecular modes are hardly affected by Ar complexation (few cm^{-1}), the peaks observed for phenol$^+$ are located at the red edge of the intramolecular bands of phenol$^+…Ar_2(2\pi)$. This is true for all observed peaks except for the first one, which is close to the dissociation threshold (ν_{11}). For this mode, the peak observed in phenol$^+$ (177 cm^{-1}) appears around 33 cm^{-1} below the maximum of the peak in phenol$^+…Ar_2$ (210 cm^{-1}). This may in part be due to the low intensity of ν_{11} itself, and the limited signal-to-noise ratio may be too low to detect $\nu_{11}+n\nu_{bx}$ with small *n*. Second, the frequency of the ν_{11} fundamental may be substantially increased upon Ar complexation due to the additional retarding force arising from repulsive forces of Ar and phenol$^+$ for this out-of-plane ring mode.

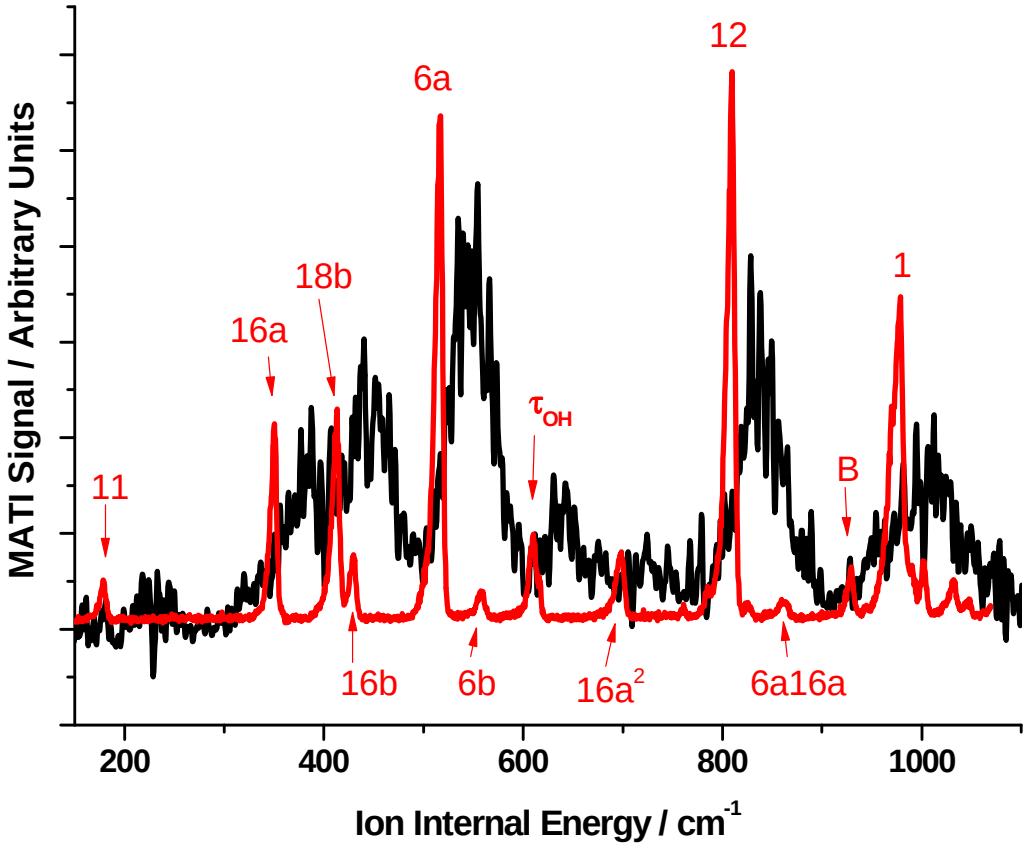

Figure 5.3: MATI spectrum of phenol$^+$…Ar$_2$(2π) recorded at the phenol$^+$…Ar mass (black) compared to the MATI spectrum of phenol$^+$ (red).

Table 5.1: Frequencies and assignments of the intramolecular vibrations in phenol$^+$ and phenol$^+$…Ar$_2$(2π).

Assignment	Frequencies / cm^{-1}	
Mode	Phenol$^+$	Phenol$^+$…Ar$_2$(2π)
11	178	210±10
16a	349	320±10
18b	411	400±10
6a	515	500±10
τ_{OH}	608	605±10
12	808	795±10
B	927	930±10
1	978	970±10

5.3.3 Dissociation energetics

Figure 5.4 summarizes the energy diagram for phenol$^+$…Ar$_n$ ($n\leq2$) obtained from the results of this work together with those from previous work. [3,7]

The lowest-energy signal observed in the MATI spectrum of phenol$^+$…Ar$_2$(2π) recorded in the phenol$^+$…Ar channel at 210 cm^{-1} gives an upper limit for the dissociation threshold. This value is much smaller than the value obtained for the dissociation energy of 535 cm^{-1} for phenol$^+$…Ar(π).[3] The dissociation energies of A$^+$…Ar(π) dimers with aromatic ions A$^+$ are typically of the order of 500 cm^{-1} (Table 5.2). The strong deviation observed here for phenol$^+$…Ar$_2$(2π) can be explained, when the $\pi\rightarrow$H isomeration is taken into account. As a consequence of this phenol$^+$…Ar$_2$(2π) $\rightarrow$ phenol$^+$…Ar$_2$(H/ π) isomerisation, the difference of the binding energy of the H-bound and π-bound site is released into other degrees of freedom of the cluster and becomes available for dissociation of the second π-bound Ar ligand. This implies that the dissociation of the second π-bound Ar ligand can be observed even when the excess energy used for ionisation of phenol$^+$…Ar$_2$(2π) is smaller than the binding energy of the π-bound Ar ligand in phenol$^+$…Ar(π). A similar isomerisation and dissociation process has recently been observed for the isoelectronic aniline$^+$…Ar$_2$ cluster. [5]

For the dissociation energy for the loss of two Ar atoms, the results obtained from MATI and PIE spectroscopy are in good accordance. The lower limit is ~1050 cm^{-1}, as obtained from the MATI spectrum recorded at the mass channel of phenol$^+$…Ar, and the upper limit is ~1180 cm^{-1}, as obtained from the PIE spectrum recorded at the mass channel of phenol$^+$. This gives a value of around 1115±65 cm^{-1}. This is nearly twice the value of the binding energy of the π-bound Ar ligand in phenol$^+$…Ar(π)[3] of 535 cm^{-1}

and can be explained by the fact, that any rearrangement has no effect on the total binding energy.

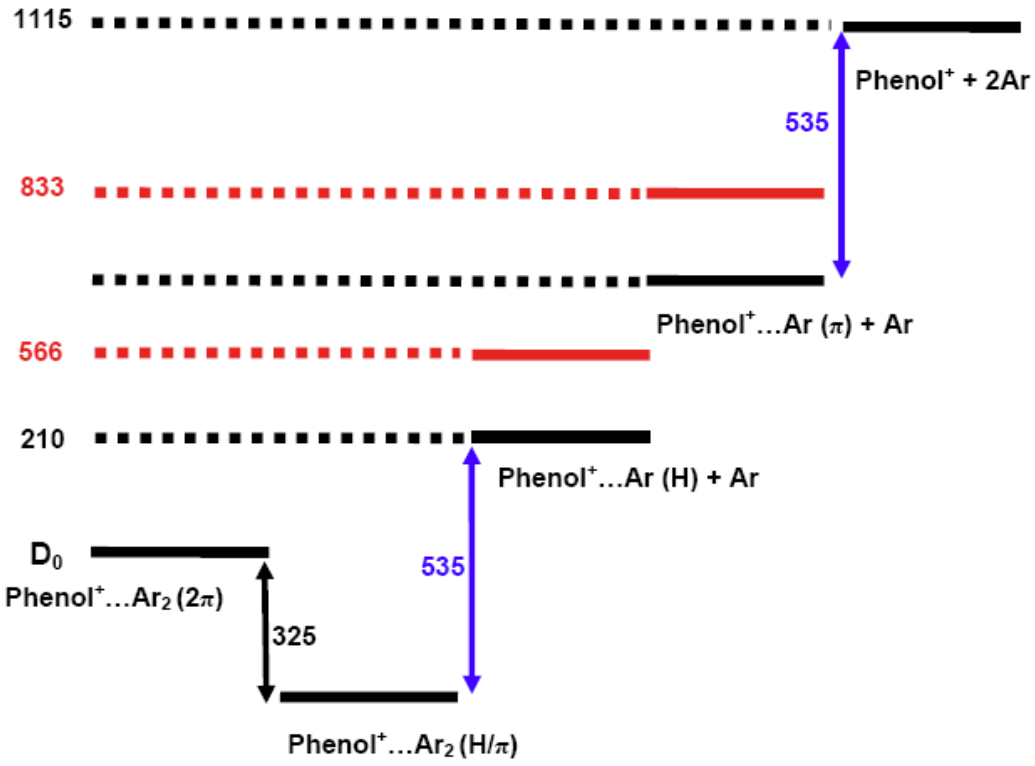

Figure 5.4: Energy diagram for phenol$^+$…Ar_2 in the cation ground electronic state, illustrating the dissociation energetics. All energies are given in cm^{-1}. The levels reported in the red colour correspond to the n6a and n12 vibrations, which were previously used to probe the isomerisation dynamics in phenol$^+$…Ar_2(2π).[7] The values of the levels reported in black colour have been obtained in this work. The value 535 cm^{-1} obtained in previous work represents the dissociation energy for the loss of one Argon atom from phenol…Ar (π). [3]

This result is also in good accordance with those for aniline$^+$…Ar_2(2π).[5] Under the reasonable assumption of negligible interaction between the two π-bonded Ar ligands in phenol$^+$…Ar(2π), the dissociation energy for the loss of both Ar ligands should be two times the dissociation energy of phenol$^+$…Ar(π) (2x(535±3)=1070±6 cm^{-1}). In fact, the

binding energy will be slightly less than this value due to small non-additive three-body forces arising from induction interactions.

The energy difference between the phenol$^+$…$Ar_2(2\pi)$ isomer, where both Ar atoms are π-bound, and the phenol$^+$…$Ar_2(H/\pi)$ isomer, where one Ar atom is π-bound and the other H-bound, can be estimated in the following way (Figure 5.4). If we assume that a H-bound Ar atom has nearly no effect on the π-bound Ar ligand, then the energy difference can be estimated as 535-210 = 325 cm^{-1}.

Table 5.2: Binding energies of aromatic van der Waals cluster ions (all values are given in cm^{-1}).

Cluster	**BE(D_0)**
Benzene$^+$…Ar[12]	486
Fluorobenzene$^+$…Ar[13]	569
p-difluorobenzene$^+$…Ar[14]	576±4
Chlorobenzene$^+$…Ar[15]	522-714
p-fluorotoluene$^+$…Ar[16]	510
o-dichlorobenzene$^+$…Ar[17]	581±76
m-dichlorobenzene$^+$…Ar[17]	529±125
p-dichlorobenzene$^+$…Ar[17]	617±15
Pyrazine$^+$…Ar[17]	630±20
Phenol$^+$…Ar[3]	535

Previous IR spectra demonstrated that ionisation of phenol$^+$…$Ar_2(2\pi)$ at excess energies below 566 cm^{-1} (lower red level in figure 5.4) generate only H-bound phenol$^+$…Ar(H) fragments, according to: [7]

$$\text{phenol}^+\ldots\text{Ar}_2(2\pi) \rightarrow \text{phenol}^+\ldots\text{Ar(H)} + \text{Ar}$$

At an excess energy of 833 cm^{-1} (higher red level in figure 5.4) also π-bound phenol$^+$…Ar(π) fragments are observed because a higher-energy fragment channel opens up:

$$\text{phenol}^+\ldots\text{Ar}_2(2\pi) \rightarrow \text{phenol}^+\ldots\text{Ar}(\pi) + \text{Ar}$$

This observation implies that the binding energy of phenol$^+$…Ar(H) is higher than that of phenol$^+$…Ar(π). From these values the binding energy of the H-bound Ar can be estimated to be around 890-1160 cm^{-1}. As the binding energy of phenol$^+$…Ar(π) is accurately measured as 535±3 cm^{-1} from the dissociation energetic of phenol…Ar(π),[3] it can further estimated that the phenol…Ar(π) fragment should be at an energy of 1115±65 – 535±3 = 580 cm^{-1} (the difference between the dissociation energy for the loss of two Ar atoms from phenol$^+$…$Ar_2(2\pi)$ and the dissociation energy of phenol$^+$…Ar(π)).

If this value is added to the energy difference between the phenol$^+$…$Ar_2(2\pi)$ and the phenol$^+$…$Ar_2(H/\pi)$ isomers, this procedure yields a value of 580+325= 905 cm^{-1} for the dissociation energy of the H-bound Ar atom in phenol…$Ar_2(H/\pi)$, which is consistent with the results obtained from IR spectroscopy (890-1160 cm^{-1}). [7]

5.4 Summary and further discussion

The investigation of the phenol$^+$…Ar$_2$(2π) cluster ion with different spectroscopic techniques such as PIE, MATI, and IR spectroscopy revealed the dissociation dynamics and energetics in great detail. In particular, the influence of the $\pi \rightarrow$H isomerisation on the appearance energies for different fragment channels could be explained. For example, ionisation of phenol$^+$…Ar$_2$(2π) with a low excess energy of 210 cm^{-1} is already sufficient to induce fragmentation into phenol$^+$…Ar(H) + Ar, although the binding energy of phenol$^+$…Ar(π) is as large as 535 cm^{-1}. The best values for the binding energies for the Ar ligands are D_0=535±3 cm^{-1} for phenol$^+$…Ar(π) and 905 cm^{-1} for phenol$^+$…Ar(H), implying that the H-bond in phenol$^+$…Ar is around 325 cm^{-1} more stable than the π-bond. These values are in accord with recent high-level *ab initio* calculations at the CCSD(T)/CBS level, yielding D_0=542 and 946 cm^{-1} for phenol$^+$…Ar(π) and phenol$^+$…Ar(H), respectively.[4] As the $\pi \rightarrow$H switch is now recognized as a common phenomenon for ionisation of clusters of rare gas atoms (or other nonpolar hydrophobic ligands)[18] and acidic aromatic molecules, similar effects of the $\pi \rightarrow$H isomerisation process analysed here for phenol…Ar$_n$ and previously for aniline…Ar$_n$ will be observed in the future for related cluster systems.

5.5 References

[1] H. Krause and H. J. Neusser, *J. Chem. Phys.*,1992, **97**, 5923.

[2] H. Krause and H. J. Neusser, *J. Chem. Phys*., 1993, **99**, 6278.

[3] C. E. H. Dessent, S. R. Haines and K. Müller-Dethlefs, *Chem. Phys.Lett.* 1999, **315**, 103.

[4] J. Cerny, X. Tong, P. Hobza and K. Müller-Dethlefs, *Phys. Chem. Chem. Phys*., 2008, **10**, 2780.

[5] Q. Gu and J.L. Knee, *J. Chem. Phys*., 2008, **128**, 064311.

[6] S. R. Haines, C. E. H. Dessent and K. Müller-Dethlefs, *J. Electr. Spec. and Rel. Phenom.*, 2000, **108**, 1.

[7] S. Ishiuchi, M. Sakai, Y. Tsuchida, A. Takeda, Y. Kawashima, O. Dopfer, K. Mülle-Dethlefs and M. Fujii, *J. Chem. Phys*., 2007, **127**, 114307.

[8] M. Takahashi, H. Ozeki and K. Kimura, *J. Chem. Phys*., 1992, **96,** 6399

[9] M.Araki, S. Sato and K. Kimura, *J. Phys. Chem.,* 1996, **100,** 10542.

[10] H. Shinohara, S Sato and K. Kimura, *J. Phys. Chem. A*, 1997, **101,** 6736.

[11] O. Dopfer, PhD Thesis, 1994, Technische Universität München, München.

[12] R. G. Satink, H. Piest, G. von Helden and G. Meijer, *J. Phys. Chem*., 1990, **111**, 10750.

[13] T. L. Grebner, P. Unold and H. J. Neusser, *J. Phys. Chem.* A, 1997, **101**, 158.

[14] S. M. Bellm, J. R. Gascooke and W. D. Lawerence, *Chem. Phys. Lett.*, 2003, **330**, 103.

[15] T. Wright, S. Panov and T. Miller, *J. Phys. Chem.*, 1995,**102**, 4793.

[16] S. Georgiev, T. Chakraborty and H. J. Neusser, *J. Phys. Chem*., 2004, **108**, 3304 .

[17] A. Gaber, M. Riese, F. Witte and J. Grotemeyer, *Phys. Chem. Chem. Phys*., 2009, **11**, 1628.

[18] O. Dopfer, *Z. Phys. Chem.*, 2005, **219**, 125.

Chapter 6

Phenol…Ar_n Clusters: Structures and Spectral Shifts

6.1 Introduction

In this chapter a spectroscopic analysis (carried out using REMPI, PIE and MATI spectroscopy) is extended to the higher clusters of phenol…Ar_n (n=3-6). Our experimental results are compared with results obtained from other aromatic clusters to propose initial structures of these complexes.

6.2 Results

6.2.1 REMPI Spectra

Two–colour (1+1') REMPI spectroscopy was used to obtain the spectra of the S_1 state of the different complexes. An appropriate second photon energy (32210 cm^{-1}) has been chosen to minimize fragmentations of higher mass species. Coumarine 153 was used for the excitation and a mixture of Sulfurhodamine B and DCM for the ionisation. The argon gas backing pressure was adjusted from 1 bar to 3 bar for the best formation of clusters.

The two–colour (1+1') REMPI spectra of phenol…Ar_n (*n*=2-6) are shown in Figure 6.1. The spectral shifts of the S_1 origins compared to the monomer origin are listed in Table 6.1. The frequencies of the intermolecular vibrations observed in the spectra are reported in Table 6.2. The results for phenol…Ar_n (*n*=2-3) are in good accordance with previous studies[1] but with a large improvement in the signal to noise ratio of the spectra. A complete analysis of the REMPI spectrum of phenol…Ar_2 can be found in Chapter 4.

For phenol…Ar_3 the origin of the $S_1 0^0$ transition is assigned to the most intense band at 36373.5 ± 0.5 cm^{-1}. The S_1 origin is therefore blue-shifted by 25 cm^{-1} from the origin of the phenol monomer. Intermolecular modes can be observed at 20 cm^{-1}, 38 cm^{-1} and 43 cm^{-1}.

The REMPI spectrum of phenol…Ar_4 displays a prominent feature at 36338.8 cm^{-1} ± 0.5 cm^{-1} that has been assigned to the $S_1 0^0$ transition. The spectral shift relative to the monomer origin is -10 cm^{-1}. Three peaks corresponding to the vibrational intermolecular modes can be clearly observed in the spectrum at 13 cm^{-1}, 20 cm^{-1} and 24 cm^{-1}.

The broad background in the spectra for *n*=5 and 6 is possibly due to fragmentation of higher masses into the observed channels. The origin transitions for those complexes are both red-shifted relative to the origin of the phenol monomer by 20 cm^{-1} and 44 cm^{-1} respectively. Intermolecular vibrational modes cannot be conclusively assigned due to the broad background.

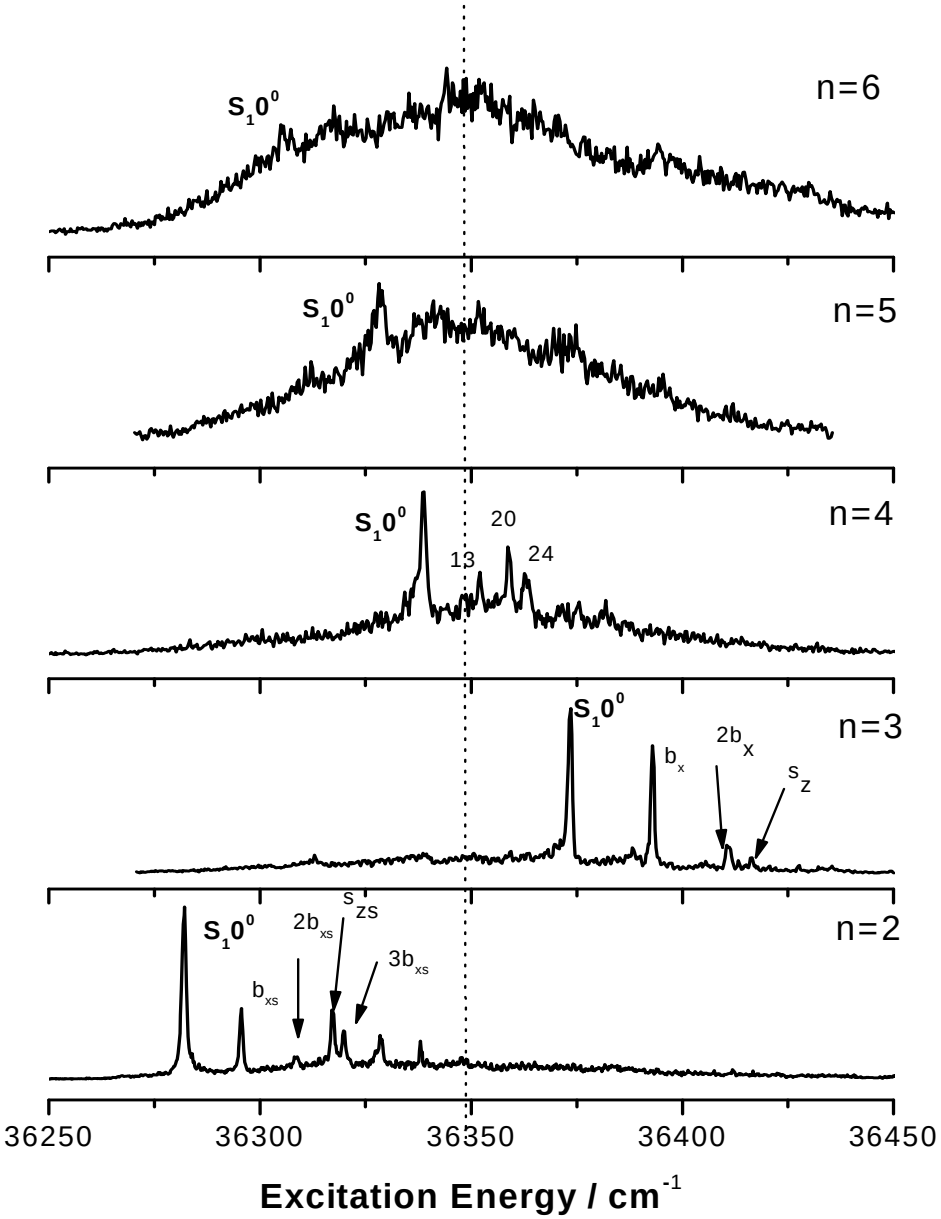

Figure 6.1: REMPI spectra of phenol…Ar_n (*n*=2-6). The dashed vertical line indicates the value of the origin transition of the phenol monomer.

Table 6.1: Shift of the S_1 origin transition and the IE of phenol…Ar_n (*n*=1-6) compared to those of the monomer.

Number of argons	S_0		D_0
	Blue shift / cm^{-1}	Red shift / cm^{-1}	Red shift / cm^{-1}
1		33	176
2		67	340
3	25		551
4		10	867
5		20	
6		44	

Table 6.2: Frequencies and assignments of the van der Waals vibrational bands observed in the REMPI spectra of phenol…Ar_n (*n*=1-4) (all values given in cm^{-1}).

Phenol…Ar		**Phenol…Ar_2**		**Phenol…Ar_3**		**Phenol…Ar_4**	
Frequency	Mode	Frequency	Mode	Frequency	Mode	Frequency	Mode
21	b_x	14	b_{xs}	20	b_x	13	
37	$2b_x$	27	$2b_{xs}$	37	$2b_x$	19	
47	s_z	36	s_{zs}	43	s_z	23	
		39	$3b_{xs}$				
		47	s_{zs} +b_{xs}				

6.2.2 PIE and MATI spectra

PIE and MATI spectroscopy was used to record spectra of the D_0 state of the phenol$^+$…Ar_n (*n*=3, 4) clusters. The pulse sequence timings and field strengths used to obtain the MATI spectra are identical to those previously described.

The PIE and MATI spectra of phenol$^+$…Ar_3, recorded by ionising *via* the $S_1 0^0$ intermediate state, are presented in Figure 6.2. From the PIE spectrum the IE can be determined to be 68055 ± 50 cm^{-1}. The MATI spectrum is characterized by a broad

structure, however a first feature can be observed at 68077 ± 15cm^{-1} which is in good accordance with the result obtained from the PIE spectrum. The IE is red-shifted by about 551 cm^{-1} from the phenol^{+} IE.

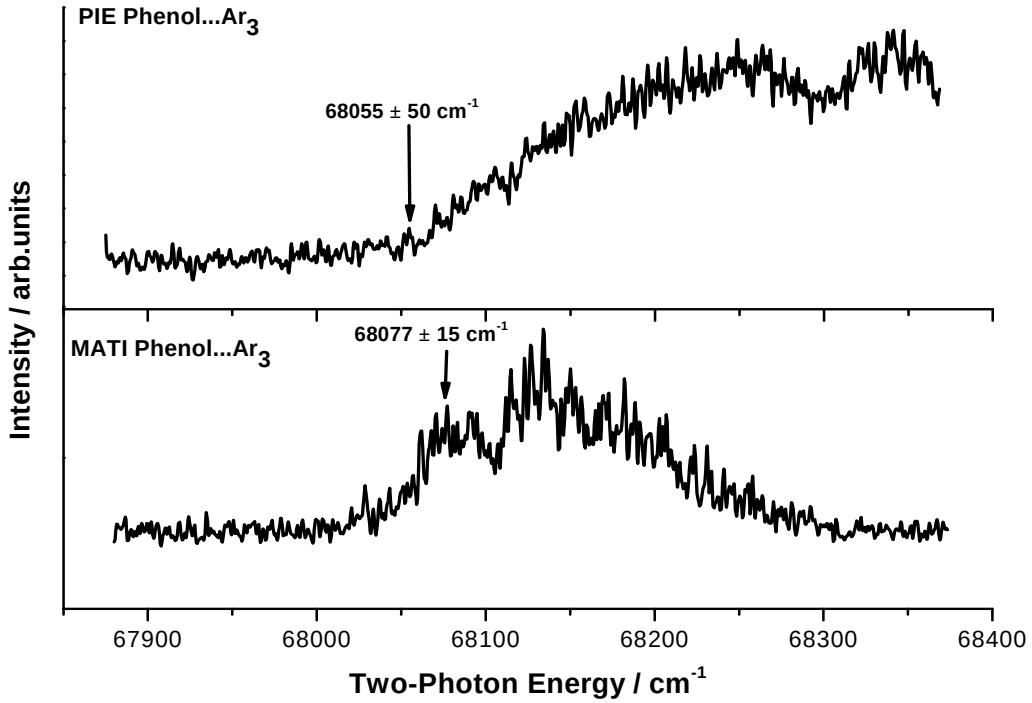

Figure 6.2: PIE and MATI spectra of phenol^{+}…Ar_3 recorded by ionising *via* the origin $S_1 0^0$ transition at 36377.5 cm^{-1}. The arrows show the position of the IE in the spectra.

Figure 6.3 shows the PIE and MATI spectra of phenol^{+}… Ar_4 recorded by ionising *via* the $S_1 0^0$ intermediate state at 36388.5 cm^{-1}. While the PIE spectrum yields a value of 67761 ± 50 cm^{-1} for the IE, no spectral features are observed in the MATI spectrum in this region. The first peak in the MATI spectrum, observed at 67948 cm^{-1} is about 187 cm^{-1} higher than the IE value determined by PIE spectroscopy, and is followed by a broad unresolved structure. It is not clear whether the MATI spectrum identifies the threshold or perhaps is just accessing the Frank-Condon region above the real ionisation potential. We propose that the value obtained with the PIE spectroscopy is a more likely

candidate for the IE. The IE of phenol…Ar_4 is red-shifted by 867 cm^{-1} compared to the IE of the monomer. The peak at 187 cm^{-1} (assuming that the value of the IE determined by PIE spectroscopy is right) corresponds to a peak observed in the ZEKE spectrum of the phenol monomer at 178 cm^{-1}.[2] This peak can be assigned as the 10b or 11 mode following Wilson's[3] or Versanyi's[4] nomenclature respectively. The broad structure may be attributed to a progression of van der Waals vibrational modes.

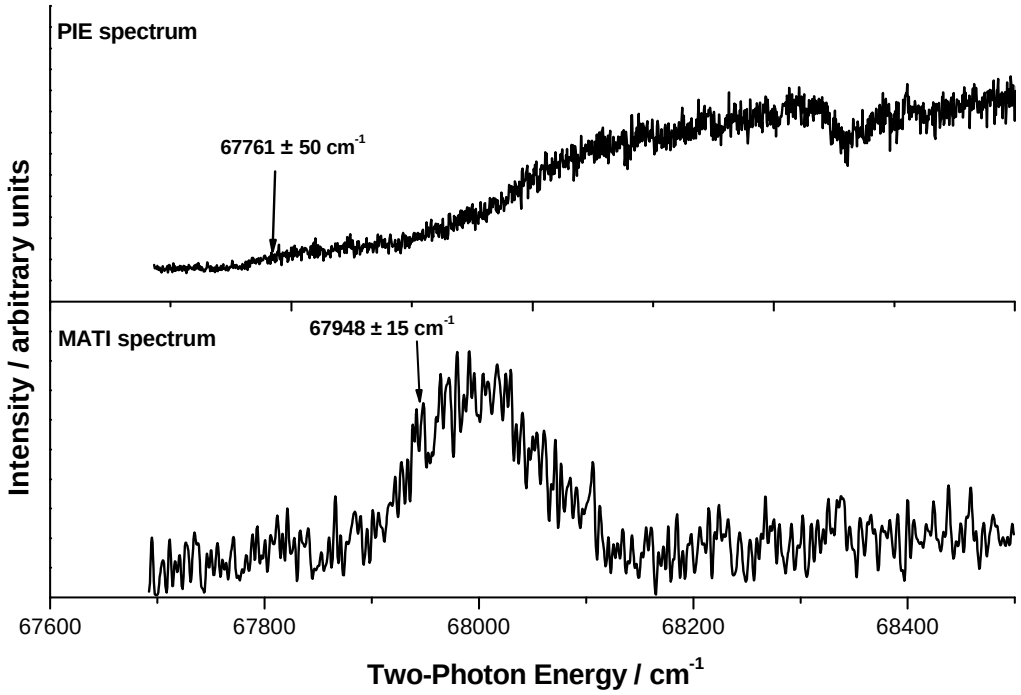

Figure 6.3: PIE and MATI spectra of phenol$^+$…Ar_4 recorded by ionising *via* the origin $S_1 0^0$ transition at 36338.5cm^{-1}. The arrows show the position of the ionisation energy in the spectra.

6.3 Spectral shifts in the S_1 and the D_0 states

6.3.1 The first electronically excited state

Figure 6.4 shows the spectral shifts for the $S_1 0^0$ transition as a function of the number of argon atoms. It can be seen that the values can be fitted by two linear curves with different slopes. The shifts for *n*=0-2 show a perfect linear dependence on the number of argon atoms. For *n*=3 a jump of the shift is observed. While up to *n*=2 a red-shift is observed, for *n*=3 we observe a blue-shift however the values for *n*=3, 5 and 6 show also a perfect linear dependence on *n*. However *n*=4 does not match this fitted curve perfectly, suggesting that the interaction between the argon atoms is 'marginally' different in comparison with all the other phenol…Ar_n (*n*=3, 5, 6) clusters.

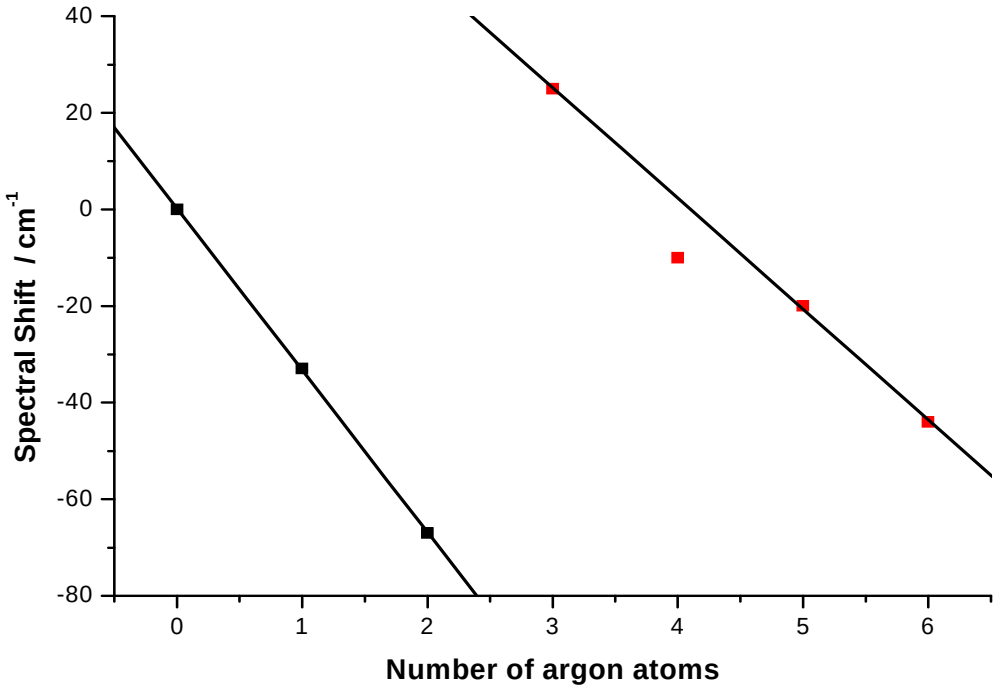

Figure 6.4: Spectral shifts of the $S_1 0^0$ electronic transition as a function of *n* (*n*=0-6) for phenol…Ar_n.

6.3.2 The ionic ground state

Contrary to the S_1 origin bands, a red-shift of the IE with comparison to the IE of the monomer is observed for all phenol$^+$…Ar$_n$ clusters, as shown in Figure 6.5. For *n*=0-3 the measured values show a very good linear dependence on the number of argon atoms. These values suggest an increasing stabilization of the cluster upon ionisation with increasing number of argon atoms. A similar trend for the ionisation energies was observed for fluorobenzene$^+$…Ar$_n$ (223 cm^{-1}, 422 cm^{-1} and 560 cm^{-1} respectively for *n*=1, 2 and 3). [5]

Only the value for the phenol$^+$…Ar$_4$ cluster does not show the same linear dependence, as it was also observed for the spectral shift of the $S_1 0^0$ transition.

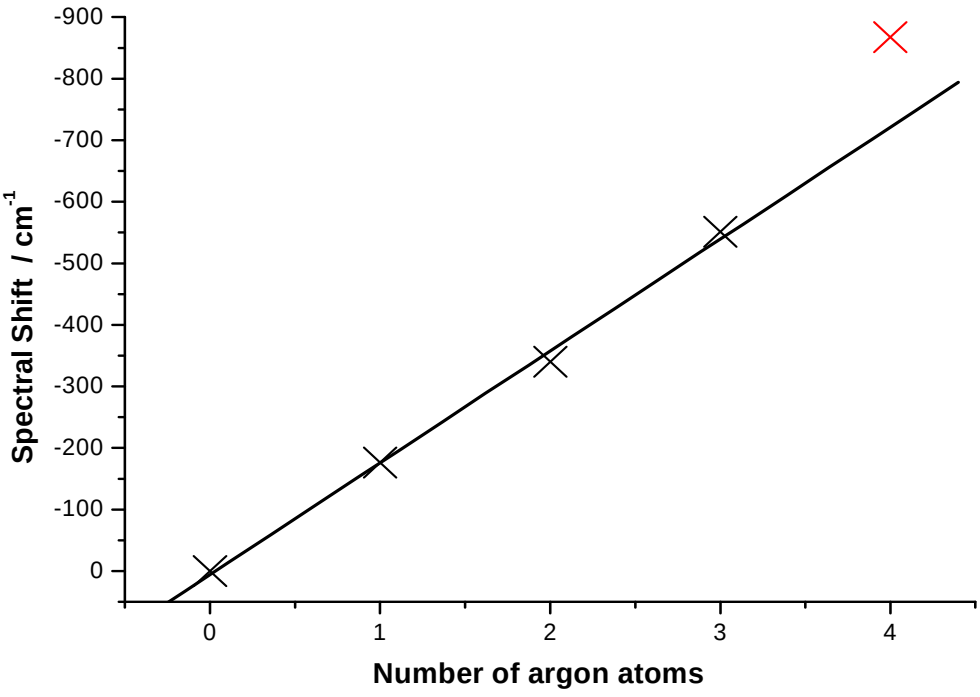

Figure 6.5: Spectral shifts of the IE as a function of *n* (*n*=0-4) for phenol$^+$…Ar$_n$

6.4 Discussion

6.4.1 Spectral shifts in benzene…Ar_n and aniline…Ar_n clusters

For a comparison of the results reported in this chapter with those obtained for benzene…Ar_n and aniline…Ar_n clusters, a brief summary of the observed spectral shifts and the interpretations is described as given by Schmidt *et al.*[6] and Douin *et al.*[7] REMPI studies of benzene…Ar_n showed the existence of two different isomers. The first group is characterized by a structure where all the argon atoms are on the same side of the ring (*n*/0) for *n*=2-7. In this case the spectral shifts of the origins were found in the range from -21 cm^{-1} to 0 cm^{-1} and a linear decrease of this red-shift was observed. In the second group the clusters have argon atoms on both sides of the ring (*m / m-n*). Up to *n*= 4 the red-shift decreases linearly in a range between ~ -42 and ~ -35 cm^{-1}. The linear curve fitting these values is parallel to that observed for the (*n*/0) isomers. For *n* > 4 the spectral shift of the (*m/m-n*) no longer shows a linear dependence on the number of argon atoms. This indicates that for *n*>5 the isomers have a significantly different structure from the isomers observed up to *n*=4. A comparison of the spectral shift between those two groups clearly revealed that the red-shift is smaller for the (*n*/0) clusters.

While only two isomers were observed for all *n* for benzene…Ar_n, in the case of aniline…Ar_n all possible π–bound isomers were found for $n \geq 2$. In figure 6.6 a reproduction of some of anilne…Ar_n (*n*=2-6) structures is shown to better visualise the most representative conformers of these clusters. There is a correlation between the spectral shift of the band origin and the position of the argon atoms: an argon atom located in the vicinity of the amino group is responsible for a blue-shift (around 32-38 cm^{-1}), whereas an argon atom close to the centre of the aromatic ring gives a red-shift of

about 53 cm^{-1}. The value for the contribution to a red-shift can be easily determined (-53 cm^{-1} is the shift for aniline…Ar and exactly double, 107 cm^{-1}, is the spectral-shift for the (1/1) isomer in aniline…Ar_2). The value for a contribution to the blue-shift can be deduced by considering the two conformers (3/0) and (2/1) for aniline…Ar_3.

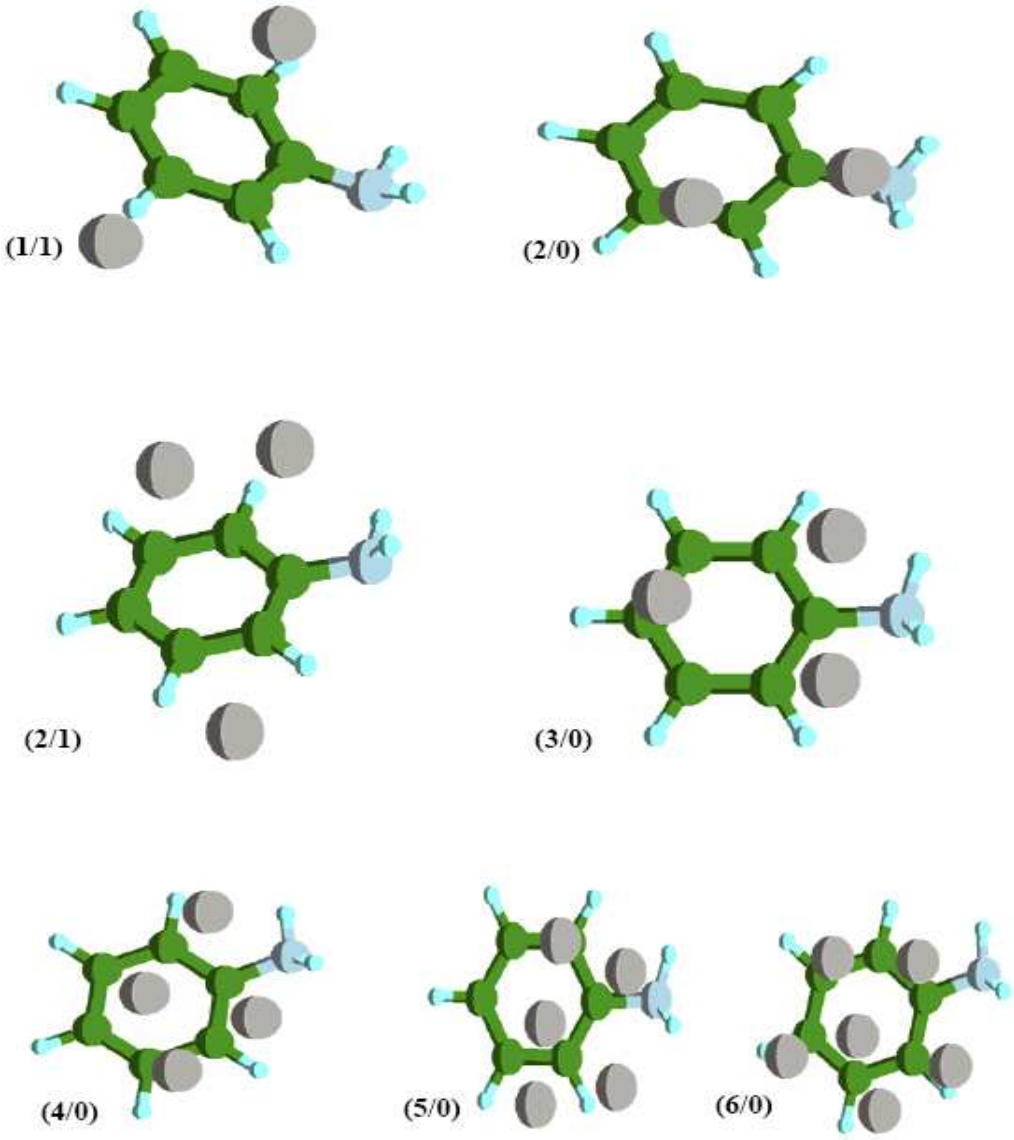

Figure 6.6: A representation of isomers structures for aniline…Ar_n (*n*=2-3): the two sides isomers (2/1) and (3/0) and the one-side isomers (2/0) and (3/0). The other structures are the one side isomers for aniline…Ar_n (*n*= 4-6) which correspond to the most stable structures.

In the case of the (3/0) structure one argon atom interacts with the ring (red-shift of -53 cm^{-1}) and two argon atoms are close to an amino group. Considering that the shift for this isomer is 23 cm^{-1}, it is possible to obtain the blue-shift: [+ 23 - (-53)] /2= 38 cm^{-1}. In the case of the (2/1) conformer (red-shift= -75 cm^{-1}), one argon atom is close to the substituent and the other two argon atoms are close to the ring (contribution to the red-shift of 107 cm^{-1}) revealing a similar value for the blue-shift contribution: (-75+107) =32 cm^{-1}. Based on these considerations a spectral shift for the (2/0) isomer of aniline…Ar_2 can be immediately estimated to be around -20 cm^{-1}: -53 cm^{-1} + (-32<x<-38 cm^{-1}) which corresponds to an observed feature in the REMPI spectrum.

These rules to determine the spectral shift on the basis of only two kinds of binding sites (the ring site and the $–NH_2$ site) seem to work very well up to n=4. For n>4 a new type of site appears: one argon atom interacting preferentially with a peripheral hydrogen atom of the aromatic ring, which gives a contribution to the red-shift of -20 cm^{-1}.

Interesting information is obtained by analysing Figure 6.7 where the electronic shift is reported as a function of the number of argon atoms in aniline…Ar_n. In particular, a perfect linear correlation is found in the case of the conformers (n/0) for n=3-6.These isomers correspond to the most stable structures (see Figure 6.6).

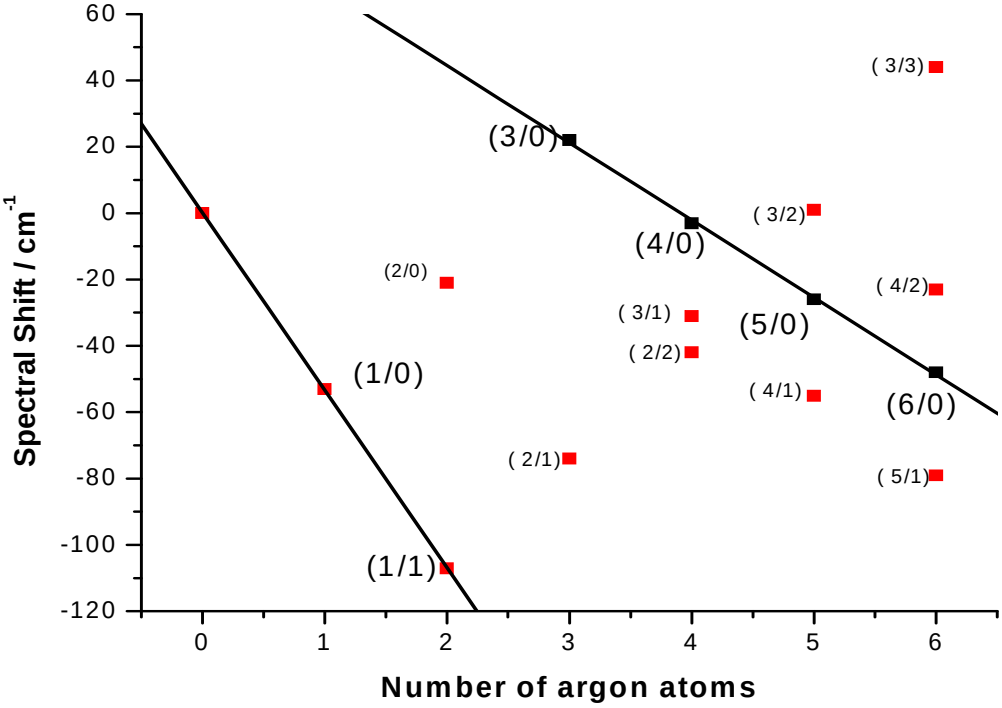

Figure 6.7: Spectral shifts of $S_1 0^0$ electronic transition as a function of *n* (*n*=0-6) for aniline…Ar_n.

6.4.2 Phenol…Ar_3

Possible structures of phenol…Ar_3

Based on geometric and energetic considerations, four possible configurations are plausible. Two structures that are characterized by only van der Waals interactions are possible: the first configuration is a (2/1) structure with a single argon atom on one side and two argon atoms on the opposite side of the ring. The second one is the (3/0) structure, where all three argon atoms are π-bound to the same side of the aromatic ring. Additionally two structures with van der Waals and H-bound are possible: the first includes one H-bound argon and two π-bound argon atoms on the same side of the aromatic ring. The next one has one H-bound argon atom and two π-bound argon atoms on opposite sides of the aromatic ring.

Intermolecular Vibrations

A very similar vibrational pattern in the REMPI spectra between phenol…Ar_3 and phenol…Ar was found by Haines *et al.* [1] Similar values were observed for b_x (21 cm^{-1} for phenol…Ar and 20 cm^{-1} for phenol…Ar_3), 2 b_x (37 cm^{-1} for phenol…Ar and 38 cm^{-1} for phenol…Ar_3) and they are in good accordance with the values found in our REMPI spectrum. The value of 43 cm^{-1} for phenol…Ar_3 present in our spectrum was not observed by Haines *et al*. and compared to the vibrational mode frequency of phenol…Ar, it may be assigned to the vibrational mode s_z.

Structure in the S_1 state

A possible structure of phenol…Ar_3 can be obtained by analysing the spectral shift of the S_1 band compared to the monomer origin.

In contrast to the red-shift observed in the case of phenol…Ar and phenol…Ar_2, the $S_1 0^0$ is blue-shifted by 25 cm^{-1} for phenol…Ar_3. Analogous results have been observed in the case of other aromatic systems.[5,7,8] In A…Ar_3 (where A = fluorobenzene[5], paraxylene[8] and aniline[7]) the REMPI spectra of these systems contain at least one prominent peak which is blue-shifted relative to the $S_1 0^0$ transition of the monomer (see Table 6.3). For fluorobenzene…Ar_3 a (2/1) structure was proposed, based on the argument that a (2/1) structure can be more stable than a (3/0) structure if the gas atoms attachment in the adiabatic expansion is sequential.

The results obtained from PIE spectroscopy of benzene…Ar_3 [9] also pointed to a (2/1) isomer instead of a (3/0) structure. However, in these studies only one isomer was observed.

Table 6.3: Shift of the origin of the S_1 origin transition compared to the monomer origin for aniline…Ar_n and fluorobenzene…Ar_n (all values given in cm^{-1})

N (Numbers of argon atoms)	1	2	3	4	5	6
Fluorobenzene…Ar_n	-24	-47	7			
aniline…Ar_n	-53	-108	23	-3	-26	-48
	(1/0)	(1/1)	(3/0)	(4/0)	(5/0)	(6/0)
para-xylene	-30	-58	3	-29	-30	-4

The observed blue-shift was explained by the fact that two argon atoms form a dimer (binding energy of Ar_2 is around 100 cm^{-1}) [10] and the strong Ar…Ar interaction reduces the red-shift compared to the *n*=2 cluster. However, the blue-shift has to be discussed in a more detailed way to attribute it to the dimer interaction. The spectral shift only gives information about the difference in the stabilisation in the S_0 and the S_1 state of one cluster compared to the monomer cluster. Without further information it is not possible to compare the binding energy in a specific state between two different clusters based only on the observed shift.

The substituent plays a crucial role when the energies of the above mentioned systems are considered. A common point in molecules such as flurobenzene, aniline or phenol is some degree of resonance (charge delocalization) between substituent and the aromatic ring. The bond of one argon atom with the substituent is responsible for a change of this resonance effect. As mentioned above for aniline…Ar_3, a blue-shift was observed for the (3/0) isomer and a red-shift for the (2/1) isomer. In the case of benzene…Ar_3, the two (3/0) and (2/1) isomers both have a spectral red-shift, however the value for the red-shift for the (2/1) isomer is almost three times bigger than the one for the (3/0) isomer. Analogously, in phenol…Ar_3 this points to a (3/0) structure with two argons adjacent to the O-H group and one atom argon interacting with the aromatic ring.

Structure in the D_0 State

A broad structure characterizes the MATI spectrum of phenol$^+$…Ar_3. The first part of this structure, of lower intensity, gives a resolved band revealing a value for the IE. The second part can be described as a congested progression of structures due to the presence of a significant number of intermolecular modes (three argon atoms give a total number of intermolecular modes equal to nine). The low intensity of the origin and the broad shape of the MATI peak due to the strong and multiple appearances of van der Waals modes indicate a structural change upon ionisation.

6.4.3 Phenol…Ar_4

Structure in the S_1 state

In contrast to phenol…Ar_3, the phenol…Ar_4 S_1 origin is red-shifted compared to the monomer origin. This value is only 10 cm^{-1} and substantially less than the red-shift found for phenol…Ar_n (n=1-2). This reduced red-shift has been observed in the same way in one of the conformers of aniline…Ar_4.[7] Computational calculations have suggested a structure for this isomer where four argons build a rhombus-like structure (see Figure 6.6) and are located in the same part of the ring. A possible evaluation regarding the structure of phenol…Ar_4 can be obtained by analysis and comparison of Figure 6.4 and 6.7. Figure 6.7 shows the shift of the origin transition for aniline…Ar_n[7] as a function of the number of argons. The conformers (3/1) and (2/2) in aniline…Ar_4 have a much bigger red-shift in common (-31 cm^{-1} and -42 cm^{-1} respectively) than the (4/0) conformer. However, contrary to phenol…Ar_4, the value of the spectral shift for (4/0) in aniline… Ar_4 can be linearly fitted with the other (n/0) isomers (n=4-6).

Combining the comparison between those two systems and the similarity of the spectral shifts, it suggests that also in phenol…Ar_4 the four atoms argons may be located on the same side of the aromatic ring.

Structure in the D_0 state

Unfortunately from the very broad structure observed in the MATI spectrum it is not possible to determine features corresponding to intermolecular modes. The broad shape of this spectrum, as observed for phenol$^+$…Ar_3, can be interpreted as a significant change of geometry in cation state. The absence of the feature relative to the IE is an additional confirmation of a strong change of the geometrical structure between S_1 and D_0.

6.4.4 Phenol…Ar_5 and phenol…Ar_6

A possible interpretation of the results found for phenol…Ar_5 and phenol…Ar_6 can be determined by comparing Figure 6.4 and 6.7. A similarity with our molecular clusters is observed when we consider the isomers (*n*/0) in aniline…Ar_n (*n*=1, 3-6) and the (1/1) isomer for aniline …Ar_2. The same considerations reported for *n*=3-4 can be extended for *n*=5-6. A possible plausible structure for these clusters is described by the argon atoms located on the same side of the ring.

6.4.5 Observed conformers in phenol…Ar_n and aniline…Ar_n

The spectral shifts observed for phenol…Ar_n and aniline…Ar_n suggest a similarity between the two systems, however a similarity does not seem to hold when the different conformers are regarded. For aniline…Ar_n all possible π-bound conformers are observed but for phenol…Ar_n only one conformer is found for each cluster. This may be

explained by the different thermodynamic conditions used in the experiments.[11] As example we consider aniline…Ar_3. The REMPI spectrum recorded by Hermine *et al.*[11] using pure argon at a pressure of 1.6 bar showed the presence of the conformer (3/0) and by only changing the experimental conditions (10% Ar in He at the pressure of 3 bar), both (3/0) and (2/1) isomers were observed.

6.5 Summary and further discussion

In this chapter, the REMPI spectra revealed that the origins of the S_1 0^0 transition of phenol…Ar_n (n = 2-6) are red-shifted from the origin monomer for all clusters with the only exception of phenol…Ar_3, where a blue shift of 25 cm^{-1} was observed. A comparison with aniline…Ar_n demonstrated that the origin spectral shifts of (n/0) conformers (n=3-6) show the same trend of those of phenol…Ar_n (n=3-6). This points to similar structures for phenol…Ar_n (n=3-6) where argon atoms are located on one side of the aromatic ring. Furthermore, the recorded PIE/MATI spectra of phenol$^+$…Ar_3 and phenol$^+$…Ar_4 allowed the determination of the IE for those clusters. The values for the IE are red-shifted by about 551 cm^{-1} and 867 cm^{-1} compared to the IE of the phenol$^+$, respectively. The broad structures observed in spectra of phenol$^+$…Ar_3 and phenol$^+$…Ar_4 suggest that a strong geometrical change occurs upon ionisation. The spectral shift of the phenol$^+$…Ar_4 cluster does not match the trend observed for the other phenol$^+$…Ar_n clusters. It has to be mentioned that the values of the IE of this cluster determined by PIE and MATI spectroscopy are not the same as usually expected. This can be due to the fact that the strong signal to noise ratio does not allow establishing if the small sequences of peaks present in the lowest energy of the spectra are indeed noise.

6.6 References

[1] S. R. Haines, C. E. H. Dessent and K. Müller-Dethlefs, *J. Electron Spectrosc. Relat. Phenom.*, 2000, **108**, 1.

[2] O. Dopfer, PhD Thesis, 1994, Technische Universität München, München.

[3] E. B. Wilson, *J. Phys. Rev.*, 1934, **45**, 706.

[4] G. Versanyi, *Assignment for Vibrational Spectra of 700 Benzene Derivates*, 1974, Wiley, New York.

[5] G. Lembach and B. Brutschy, *J. Chem Phys.*, 1997, **107**, 6156.

[6] M. Schmidt, J. Le Calvé and M. Mons, *J. Chem. Phys.*, 1993, **98**, 6102.

[7] S. Douin, P. Parneix, F. G. Amar and P. Brechignac, *J. Phys. Chem.* A, 1997, **101**, 122.

[8] P. D. Dao, S. Morgan and A. W. J. Casleman, *Chem. Phys. Lett.*, 1985, **113**, 219.

[9] B. Kamke, W. Kamke, Z. Wang, E. Rühl and B. Brutschy, *J. Chem Phys.*, 1987, **86**, 2525.

[10] P. R. Herman, P. E. Larocque and B. P. Stoicheff, *J. Chem. Phys*., 1988, **89**, 4535.

[11] P. Hermine, P. Parneix, B. Coutant, F. G. Amar and P. Bréchignac, *Z.Phys.D:At. Mol. Cluster*, 1992, **22**, 529.

Chapter 7

Fragmentation energetics phenol$^+$...Ar$_3$

7.1 Introduction

In this chapter the dissociation process for phenol$^+$…Ar$_3$ is considered, comparing the results obtained for this molecular system with the data earlier analysed for phenol$^+$…Ar$_2$. Also in this case the entire process is explained supposing a possible isomeration process upon ionisation.

7.2 Results

7.2.1 PIE spectra

The experimental conditions to produce the phenol…Ar$_3$ cluster to record the PIE/ MATI spectra are identical to those reported in the previous chapter.

Figure 7.1 shows the PIE spectra recorded *via* the $S_1 0^0$ intermediate state of phenol$^+$…Ar$_3$ at 36373.5 cm^{-1} simultaneously recorded at the mass of the phenol$^+$…Ar$_3$ parent ion channel (214 u), and phenol$^+$… Ar$_n$ (*n*=0-2) fragment ion channel masses.
A first clear step in the spectrum at the phenol$^+$…Ar$_3$ parent mass is observed at 68055 ± 50 cm^{-1} and assigned to the adiabatic ionisation threshold and in agreement with the results reported in Chapter 6. The first signal in the PIE spectrum monitored in the

phenol$^+$…Ar_2 mass appears at ~68255 cm^{-1} ± 30 cm^{-1} (~ 200 cm^{-1} above the ionisation threshold of phenol$^+$…Ar_3), providing an upper limit for the dissociation threshold for the loss of one argon from phenol$^+$…Ar_3. The first threshold seen in the PIE spectrum recorded at the phenol$^+$…Ar channel occurs 68875 cm^{-1} ± 30 cm^{-1} yielding an upper limit value of 850 ± 50 cm^{-1} for the dissociation threshold for the loss of two argon atoms. Finally the dissociation energy for the loss of all three atom argon atoms is observed at 1730 ± 50 cm^{-1} in the PIE spectrum recorded at the phenol$^+$ monomer channel.

7.2.2 MATI spectra

In order to obtain more accurate values for the individual threshold dissociation of phenol$^+$…Ar_3 (3π), MATI spectra were recorded via the origin of the first excited state of phenol$^+$…Ar_3(3π), monitored simultaneously in the phenol$^+$…Ar_n mass channels with *n*=1-3 (Figure 7.2).The pulse sequence, timing and field strengths used in the MATI experiment are identical to those reported in Chapter 3.

The MATI spectrum of the *n*=3 parent cluster is characterized by a single broad and nearly unresolved feature with a width of ~190 cm^{-1}. The first signal appears at 68077 ± 15 cm^{-1}, which is assigned to the adiabatic IE. This value is in full agreement with that previously obtained in the PIE spectrum.

The spectrum recorded for the *n*=2 fragment channel displays a first broad peak beginning to rise at 130 cm^{-1} above the IE of phenol$^+$…Ar_3. A further even broader feature can be seen at higher energy, covering the range 350-700 cm^{-1}. The spectrum

recorded at the *n*=1 fragment channel shows two broad structures in the range 780-1115 cm^{-1} and 1195-1340 cm^{-1} above the IE of phenol$^+$…Ar_3.

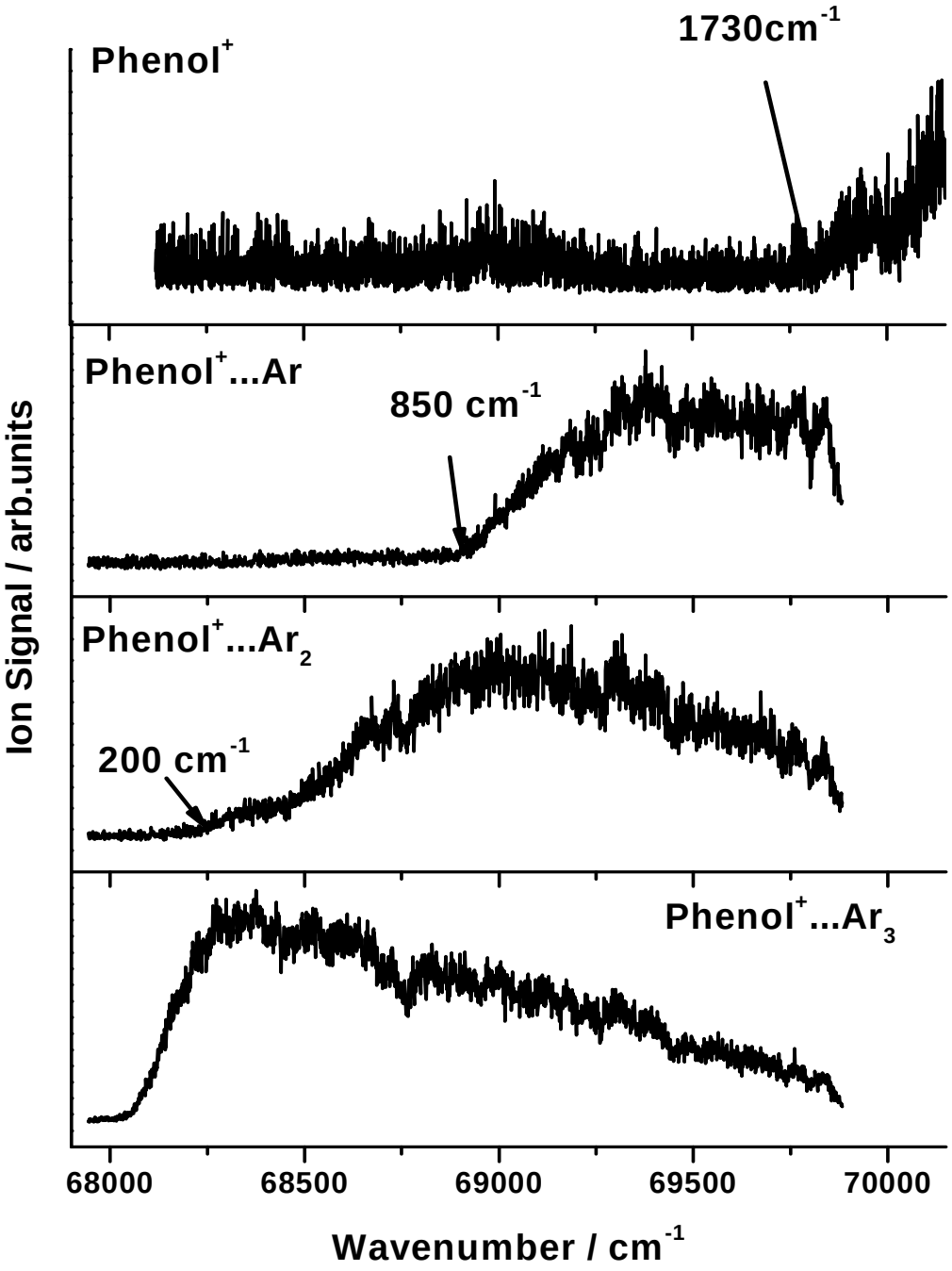

Figure 7.1: PIE spectra of phenol$^+$…Ar_3 recorded at the cluster mass and the fragment masses phenol$^+$…Ar_n (*n*=0-2).

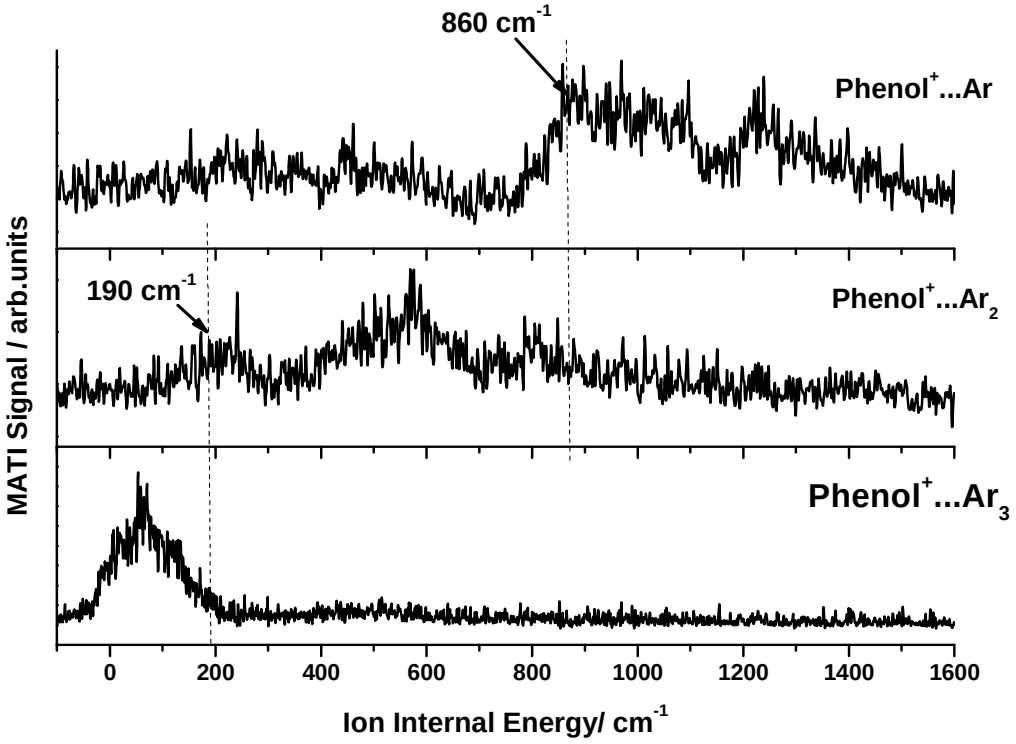

Figure 7.2: MATI spectra recorded in the phenol$^+$…Ar_3 parent and phenol$^+$…Ar_n (*n*= 1,2) fragments channels obtained *via* excitation of the $S_1 0^0$ origin of phenol$^+$…Ar_3.

7.3 Discussion

7.3.1 Spectral shift in ion ground state

As discussed in Chapter 6, the spectral red-shift of phenol$^+$…Ar_3 compared to the monomer in the cation state is 551 cm^{-1}. This value is almost three times the red-shift for phenol$^+$…Ar (176 cm^{-1})[1] and fits almost perfectly the linear trend characterizing the ionisation energies of phenol$^+$…Ar_n (*n*=1-3). This result is consistent with 3 π-bound Ar atoms in phenol$^+$…Ar_n. A similar trend was already observed in the case of fluorobenzene$^+$…Ar_n cluster (223 cm^{-1}, 422 cm^{-1} and 560 cm^{-1} respectively for *n*=1, 2 and 3).[2]

7.3.3 Intramolecular vibrations

The very broads peaks observed in the MATI spectra at the mass channel of phenol…Ar_n (n=1, 2) do not allow a precise determination of the intramolecular vibrations frequencies of the phenol$^+$ moiety associated with these transitions. Also for phenol$^+$…Ar_2(2π), the intramolecular vibrational bands were broad in the MATI spectra, however it was still possible to recognize that the width of these bands are a consequence of combination bands of an intramolecular mode with a progression of several quanta of the low-frequency van der Waals mode b_{xs} with a frequency of 10 cm^{-1}. The MATI peaks in phenol$^+$…Ar_3 (3π) are even broader (>100 cm^{-1}), than those of phenol$^+$…Ar_2(2π) (~50 cm^{-1}), as the n=3 complex has three more van der Waals modes than the n=2 complex. Due to the lack of resolved structure, the frequencies of the van der Waals vibrations of phenol$^+$…Ar_3(3π) cannot be determined. On the other hand, the bare intramolecular frequencies can be associated with the red edge of the MATI peaks. To demonstrate this assignment, the MATI spectrum of phenol$^+$ is compared in Figure 7.3 and 7.4 to the MATI spectra recorded *via* the S_1 origin of phenol$^+$…Ar_3(3π) monitored in the n=2 and n=1 fragment channels, respectively.

The derived intramolecular frequencies of phenol$^+$…Ar_n (n =1, 2) are listed in Table 7.1, along with the frequencies determined for bare phenol$^+$ and the assignment given by Dopfer.[3]

It is interesting to note that the intensity of ν_{11} in the MATI spectrum of phenol$^+$…Ar_3(3π) recorded in the n=2 channel is relatively high compared to, for example, the ν_{6a} intensity, I_{6a}:I_{11}~2:1. For bare phenol$^+$ and also for phenol$^+$…Ar_2(2π), this ratio is much larger, I_{6a}:I_{11}~12:1. This enhancement in the ν_{11} intensity may be

attributed to a reduction in symmetry. While phenol$^+$ and phenol$^+$…$Ar_2(2\pi)$ have C_s symmetry, for which the ν_{11} out-of-plane mode is Franck-Condon forbidden, phenol$^+$…$Ar_3(3\pi)$ has C_1 symmetry, and ν_{11} becomes Franck-Condon allowed.

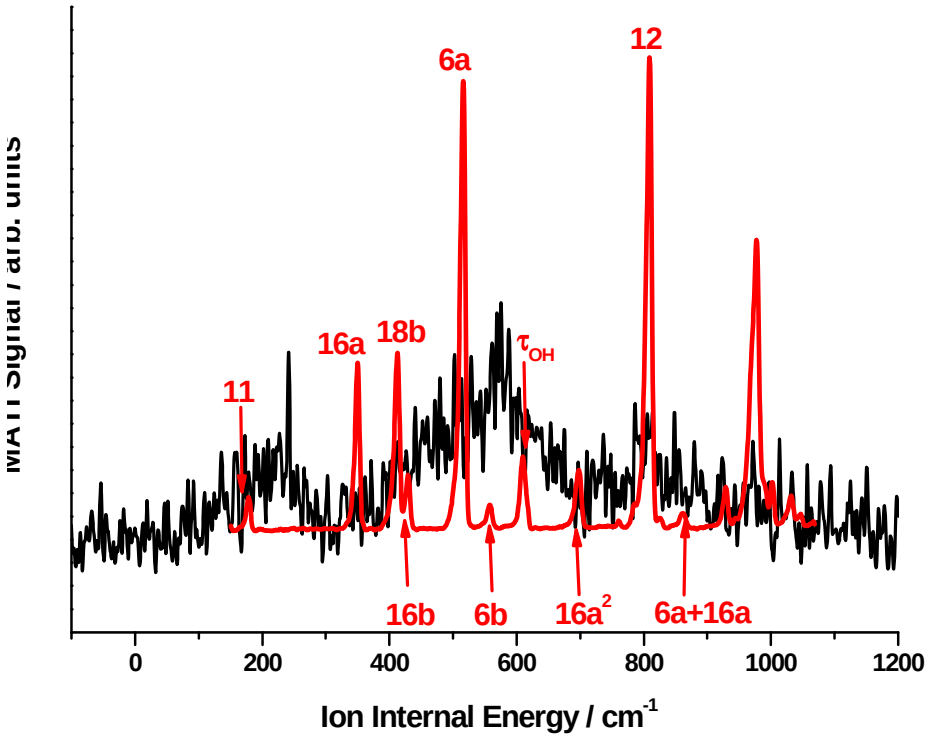

Figure 7.3: MATI spectra of phenol$^+$ (red) and phenol$^+$…Ar_2 from dissociated phenol$^+$…Ar_3. Assignments for the vibrational modes of phenol$^+$ are included, as given by Ref. 3.

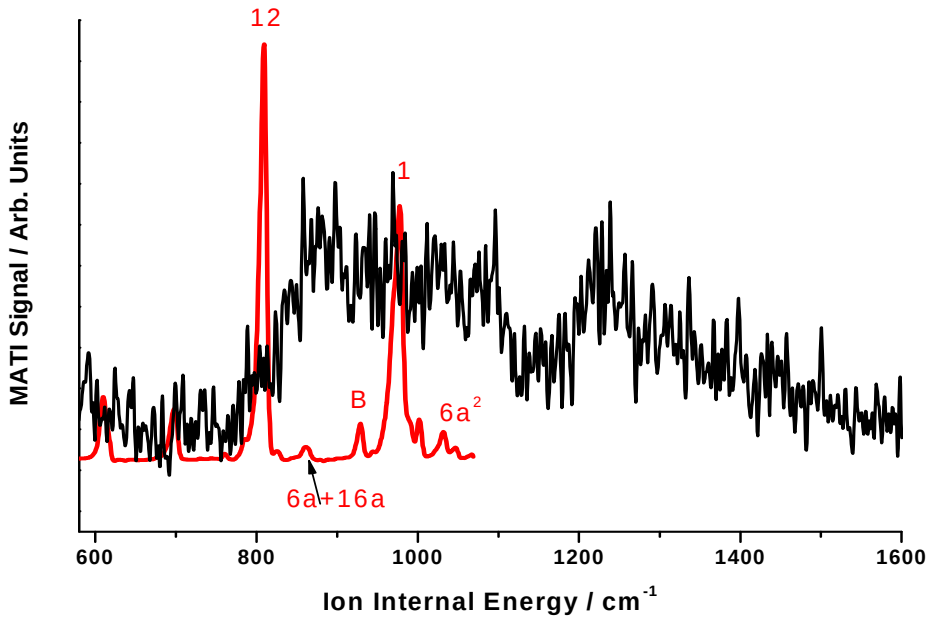

Figure 7.4: MATI spectra of phenol$^+$ (red) and phenol$^+$…Ar from dissociated phenol$^+$…Ar$_3$. Assignments for the vibrational modes of phenol are included, as given by Ref 3.

7.3.4 Dissociation energetics

Figure 7.5 summarizes the energetics derived from the dissociation thresholds observed in the PIE and MATI spectra of phenol$^+$…Ar$_3$(3π) in Figures 7.1 and 7.2

Dissociation threshold for the loss of one argon atom

From the PIE spectrum recorded in the n=2 channel, an upper limit for the dissociation threshold for the loss of one Ar atom is estimated as 200±60 cm^{-1}. A more accurate value is derived from the MATI spectrum observed in the n=2 and 3 channels. MATI signals are simultaneously detected in both channels in the ~130-190 cm^{-1} range due to the coupling of Rydberg states.[4,5]

Table 7.1: Assignment of the intramolecular vibration in phenol$^+$ of the phenol monomer and phenol$^+$…Ar/ phenol$^+$…Ar$_2$ / phenol$^+$…Ar$_3$ from dissociated phenol$^+$…Ar$_3$

Mode	**Vibrational frequency / cm^{-1}**			
	Phenol$^+$	**Phenol$^+$…Ar$_3$** recorded at the mass of		
		Phenol$^+$…Ar$_3$	**Phenol$^+$…Ar$_2$**	**Phenol$^+$…Ar**
0^0	0	0-210	130-290	
11	178			
16a	349		360-700	
18b	411			
16b	429			
6a	515			
6b	557			
τ_{OH}	608			
$16a^2$	697			
12	808		785-850	780 -1115
6a+16a	862			
B	927			
1	978			
F	1002			
$6a^2$	1032			
$16a^3$	1043			
6a + 6b	1071			

Grebner *et al.*[4] demonstrated for the case of fluorobenzene…Ar clusters that the measured value of the fragment ion appearance energy depends on the strength of the applied ionisation field. For low electric fields (125 V/cm) the appearance of peaks in the fragment channel was shifted towards higher internal energy (some few 10 cm^{-1}) compared to high electric fields (975 V/cm). This observation was explained by a coupling of the originally excited high Rydberg levels of series converging to a vibrational state below the field-free dissociation threshold to lower Rydberg states converging to a vibrational state above the dissociation threshold of the ionic core. The coupling is induced by the pulsed electrical ionisation field. The coupling results in a transfer of electronic energy from the excited high Rydberg electron to the vibrational

degrees of freedom of the cluster ion core, causing dissociation of the cluster, even when the total energy is less than IE+D_0^+. Here it is assumed that the Rydberg states survive the dissociation, as shown in Ref 5. The dissociation can be detected if the ionising field strength is sufficient to ionise the low Rydberg states of the fragment Rydberg molecule.

The appearance of MATI signal in the fragment channel depends on the strength of the ionising field, whereas the signal of the parent cluster is not affected by the field. Therefore the disappearance of the signal in the parent ion channel, rather than the appearance in the fragment channel, provides the true value for dissociation energy. As the signal in the *n*=3 channel disappears at ~190 cm^{-1}, an accurate value for the dissociation energy of one Ar atom from phenol$^+$…Ar_3(3π) is determined as 190±20 cm^{-1}, which is compatible with the value obtained from the PIE spectrum. This value is also very similar to that found for phenol$^+$…Ar_2 (210 cm^{-1}). Both values are, however, much smaller than the dissociation energy for a π-bound ligand of phenol$^+$…Ar(π), D_0=535±3 cm^{-1}.[6] This apparent discrepancy for phenol$^+$…Ar_n(*n*π) with n=1-3 differs qualitatively from the case of related clusters such as fluorobenzene$^+$…Ar_n(*n*π) (n=1-3),[2] for which almost equal Ar binding energies are determined, namely D_0=567, 546, and 502 cm^{-1} for n=1-3, respectively (Table 7.2). For phenol$^+$…Ar_2(2π), the rather low dissociation threshold for Ar loss was rationalised by a π→H isomerisation process induced by ionisation, in which one of the π-bound ligands isomerises to the OH binding site yielding phenol$^+$…Ar_2(H/π).[7,8] A similar π→H isomerisation process occurs also after ionisation of the *n*=3 complex, namely phenol$^+$…Ar_3(3π) → phenol$^+$…Ar_2(H/2π). As a consequence of the π→H isomerisation, the difference of the binding energy of the H-bound and π-bound site is released into

other degrees of freedom of the cluster and becomes available for dissociation of a further π-bound Ar ligand. This implies that the dissociation threshold for the elimination of the π-bound Ar ligand can be observed even when the excess energy used for ionisation of phenol$^+$…Ar$_3$(3π) is smaller than the binding energy of the π-bound Ar ligand in phenol$^+$…Ar(π) (535 cm^{-1}).[6] A similar isomerisation and dissociation process has recently also been observed for the aniline$^+$…Ar$_2$ cluster. [9]

Assuming a value of 535 cm^{-1} for a π-bound Ar ligand[6] (dissociation energy for the loss of one argon atom from phenol$^+$…Ar(π)), the threshold of 190 cm^{-1} (dissociation threshold for the loss of one argon atom from phenol$^+$…Ar$_3$(3π)) implies that the dissociation energy of an H-bound ligand is 345 cm^{-1} larger than the binding energy of the π-bound ligand i.e. D_0(H)-D_0(π) = (535-190)= 345 cm^{-1}.

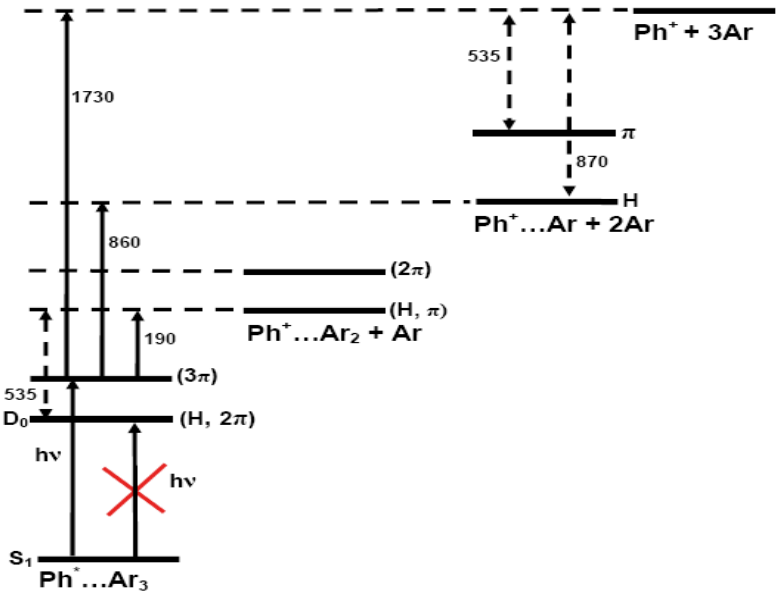

Figure 7.5: Diagram of dissociation process for phenol$^+$…Ar$_3$. All energies are given in cm^{-1}. The energy values 190, 860 and 1730 cm^{-1} have been directly determined by the MATI/PIE spectra reported in this chapter. The value 535 cm^{-1} represents the dissociation energy for the loss of one Argon atom from phenol$^+$… Ar(π) according to Ref. 1.

Table 7.2: Summary of the dissociation thresholds (in cm^{-1}) for the loss of one (D_0), two (D_1) and three (D_2) Ar atoms for phenol$^+$…Ar_n and fluorobenzene$^+$…Ar_n (*n*=1-3).

Cluster	D_0	D_1	D_2
Phenol$^+$…Ar	535		
Phenol$^+$…Ar_2	210	1115	
Phenol…Ar_3	180	860	1730
Fluorobenzene$^+$…Ar	567		
Fluorobenzene$^+$…Ar_2	546	1164	
Fluorobenzene$^+$…Ar_3	502	1066	/

Dissociation threshold for the loss of two argon atoms

The dissociation energy for the loss of two Ar atoms from phenol$^+$…Ar_3 (3π) is derived from the MATI spectra recorded in the *n*=2 and *n*=1 fragment channels (Figure 7.2). Spectral overlap is observed in the 780-860 cm^{-1} frequency range, corresponding to excitation of ν_{12} and $\nu_{6a}+\nu_{16a}$ with intermolecular modes. The dissociation threshold of 860 cm^{-1} obtained from the MATI spectrum is consistent with the PIE threshold of ~850 cm^{-1} (Figure 7.1).

Dissociation energy for the loss of three argon atoms

Further information on the dissociation energies of phenol$^+$…Ar_3(3π) is provided by the first threshold observed in the PIE spectrum recorded in the phenol$^+$ channel at 1730 cm^{-1}. This energy is actually only an upper limit for the elimination of all three π-bound ligands from phenol$^+$…Ar_3(3π) . However, as the density of states is quite high in the frequency range, this upper limit is probably close to the true value. Indeed, this threshold is only slightly higher than three times the binding energy of phenol$^+$…Ar$(\pi)^6$, (3 x 535 = 1605 cm^{-1}), indicating that the incremental Ar binding energy for π-bonding does not depend much on the cluster sizes for $n \leq 3$. Some cooperative effects arise from additional Ar…Ar interactions, while non-cooperative effects are due to non-additive

induction forces and steric hindrance. Any intracluster rearrangement during the presumably sequential dissociation process, such as the π→H isomerisation described above, does not affect this value, as the process is barely described by phenol$^+$…Ar$_3$(3π) → phenol$^+$ + 3 Ar. As can be seen from Figure 7.5, the experimental binding energy for the H-bound Ar ligand in phenol$^+$…Ar(H) can be derived as the difference between the dissociation energy for the loss of three Ar Atom and the dissociation threshold for the loss of two Ar atoms from phenol$^+$…Ar$_3$(3π) (D_0(H)=1730-860=870 cm^{-1}). This value is also close to binding energy derived from a similar analysis of the dissociation processes in phenol$^+$… Ar$_2$(2π), D_0(H) = 905 cm^{-1}.

7.4 Summary and further discussion

The Ar binding energies to the phenol$^+$ cation have been determined for various ligand binding sites by analysing the PIE and MATI spectra of phenol$^+$…Ar$_3$(3π) recorded in the parent and fragment ion channels via resonant excitation of the S_1 origin. The energy diagram is complicated by a π→H isomerisation process induced by ionisation of neutral phenol…Ar$_3$ (3π), yielding a relatively low appearance energy of 190 cm^{-1} for the phenol$^+$…Ar$_2$(H/π) fragment. Analysis of the various dissociation thresholds observed result in binding energies of D_0(H)=870 cm^{-1} and D_0(π)=535 cm^{-1} for phenol$^+$…Ar, which are in good agreement with the best available theoretical values D_0(H)=946 cm^{-1} and D_0(π)=542 cm^{-1}, respectively.[10] The dissociation energy for all three π-bound ligands in phenol$^+$…Ar$_3$(3π) of 1730 cm^{-1} is roughly three times the value of D_0(π)=535 cm^{-1} obtained for phenol$^+$…Ar(π). This observation suggests that incremental bond energies for π-bonded ligands in phenol$^+$…Ar$_n$ (nπ)) are roughly independent of the cluster size n in the size range n≤3. Clearly, the ionisation-induced π

$\rightarrow$H switch observed for phenol…$Ar_3(3\pi)$) yielding phenol…$Ar_3(H/2\pi)$) confirms that prior to ionisation all Ar ligands must occupy π binding sites.

7.5 References

[1] S. R. Haines, C. E. H. Dessent and K. Müller-Dethlefs, *J. Electron Spectrosc. Relat. Phenom.*, 2000, **108**, 1.

[2] G. Lembach and B. Brutschy, *J. Chem. Phys.*, 1997, **107**, 6156.

[3] O. Dopfer, PhD Thesis, 1994, Technische Universität München, München

[4] Th. L. Grebner and H. J. Neusser, *Chem,. Phys. Lett.*, 1995, **245**, 578.

[5] Th. L. Grebner, P. V. Unold and J. Neusser, *J. Phys. Chem*. A, 1997, **101,** 158.

[6] C. E. H. Dessent, S. R. Haines and K. Müller-Dethlefs, *Chem. Phys. Lett.*, 1999, **315**, 103.

[7] S. Ishiuchi, M. Sakai, Y. Tsuchida, A.Takeda, O. Dopfer, K. Müller-Dethlefs and M. Fujii, *J. Chem. Phys.*, 2007, **127**, 114307

[8] S.I. Ishiuchi, M. Sakai, Y. Tsuchida, A.Takeda, Y. Kawashima, M. Fujii, O.Dopfer and K. Müller-Dethlefs, *Angew. Chem., Int. Ed.* 2005, **44**, 6149.

[9] Q. Gu and J.L. Knee, *J. Chem. Phys*., 2008, **128**, 064311.

[10] J. Cerny, X. Tong, P. Hobza and K. Müller-Dethlefs, *Phys. Chem. Chem. Phys*., 2008, **10**, 2780.

Chapter 8

Rotational band contour analysis in REMPI: elucidating the structures of phenol…Ar_3

8.1 Introduction

An isolated analysis of experimental results obtained from REMPI spectroscopy is not generally sufficient to give conclusive information regarding the structure of molecular systems. *Ab initio* calculations can furnish a good idea of the possible structures for the systems where multiple conformers exist. The general approach of comparing vibrational modes observed in REMPI and ZEKE spectra with *ab initio* calculation can provide reliable structural information. However it is not possible to determine a unique geometry for the systems studied with absolute certainty. The rotational band contour analysis of the $S_1 \leftarrow S_0$ transition can be an efficient tool to suggest the possible structure of isolated molecules or clusters. In particular, this method of matching calculated and experimental band contours represents a procedure for determining the band type (a, b, c or hybrid) and the assignment of the symmetry of the molecules or clusters analysed. A large number of geometric structures of hydrogen bonded and vdW complexes of aromatic molecules[1,2,3] have been determined using this method. In the case of

phenol…Ar_n (n=1-2), the simulation of the rotational band structure of the $S_1 \leftarrow S_0$ transition was the final proof to establish the π-bond interaction.[4,5]

The phenol molecule behaves as a near-prolate asymmetric top giving rise to a b-type band contour. As a consequence the direction of the transition dipole is in the short axis of the aromatic ring.[6] Complexation may cause rotation of the inertial frame and/or the transition dipole and consequently a change in polarization. As an example, the spectra of aniline and the aniline…Ar cluster recorded using high-resolution laser induced fluorescence (LIF) is cosidered.[3] While the spectrum of the bare molecule displays a b-type character, the rotational profile of the cluster is c-type. The difference in the contour shape can be explained by the change of direction of the inertial axis which is associated with the argon atom located on the aromatic ring. No effects can be observed because of the transition moment. The transition moment in the complex should be polarized in the same direction as in the bare aniline.

In Chapter 6, an assumption for the structure of phenol…Ar_3 in the intermediate state S_1 was made on the basis of considerations on the spectral shift of the origin transition $S_1 0^0$ compared to the phenol monomer. In this chapter an analysis of the rotational band contour will support the geometry deduced for phenol…Ar_3 in chapter 6.

8.2 Results and discussion

8.2.1 Isomers

To determine possible structures of phenol…Ar_3 clusters *ab initio* calculations were performed using the resolution of identity second-order Møller-Plesset perturbation theory (RI-MP2). This method was used as implemented in the Turbomole package

5.10.[7] The cc-pVDZ and cc-pVTZ basis sets were employed for the calculations. Diffuse functions (aug-) for the argon atoms were added to recover the long-range dispersion interaction between the phenol and the argon atoms moieties. The validity of the calculated geometries has been verified by the fact that no imaginary vibrational mode frequencies have been found for each structure (the vibrational-frequency calculations were performed using the NumForce, part of the Turbomole 5.10 package).

The most stable structures for phenol…Ar_3 are presented in Figure 8.1. The structure in Figure 8.1 labelled 1/1/1, has one argon with hydrogen bonded interaction and the other two argon atoms having a π-interaction located on the opposite side of the aromatic ring. The other two structures present only π-interactions. The structure reported in Figure 8.1 labelled 2/1 has two argon atoms on one side of the aromatic ring and the other on the opposite side. The structure in Figure 9.1 labelled 3/0 has the three argon atoms on the same side of the ring with two argon atoms located in the vicinity of the O-H group. Finally the last structure (labelled 2/1H, Figure 9.1), is represented by two argon atoms having a π-bond on one side of the ring and another argon atom having hydrogen interaction.

The rotational constants in S_0 state for each of the possible conformers obtained from the *ab initio* calculations are listed in Table 8.1

Table 8.1: Rotational constants in the S_0 state of the phenol…Ar_3 complex for the four different isomers obtained from *ab initio* calculations using cc-pVTZ basis sets.

Isomer	**A**	**B**	**C**
3/0	703.5	481.9	467.1
2/1	942.4	358.0	286.3
1/1/1	929.4	361.5	296.1
2/1H	692.2	447.2	369.5

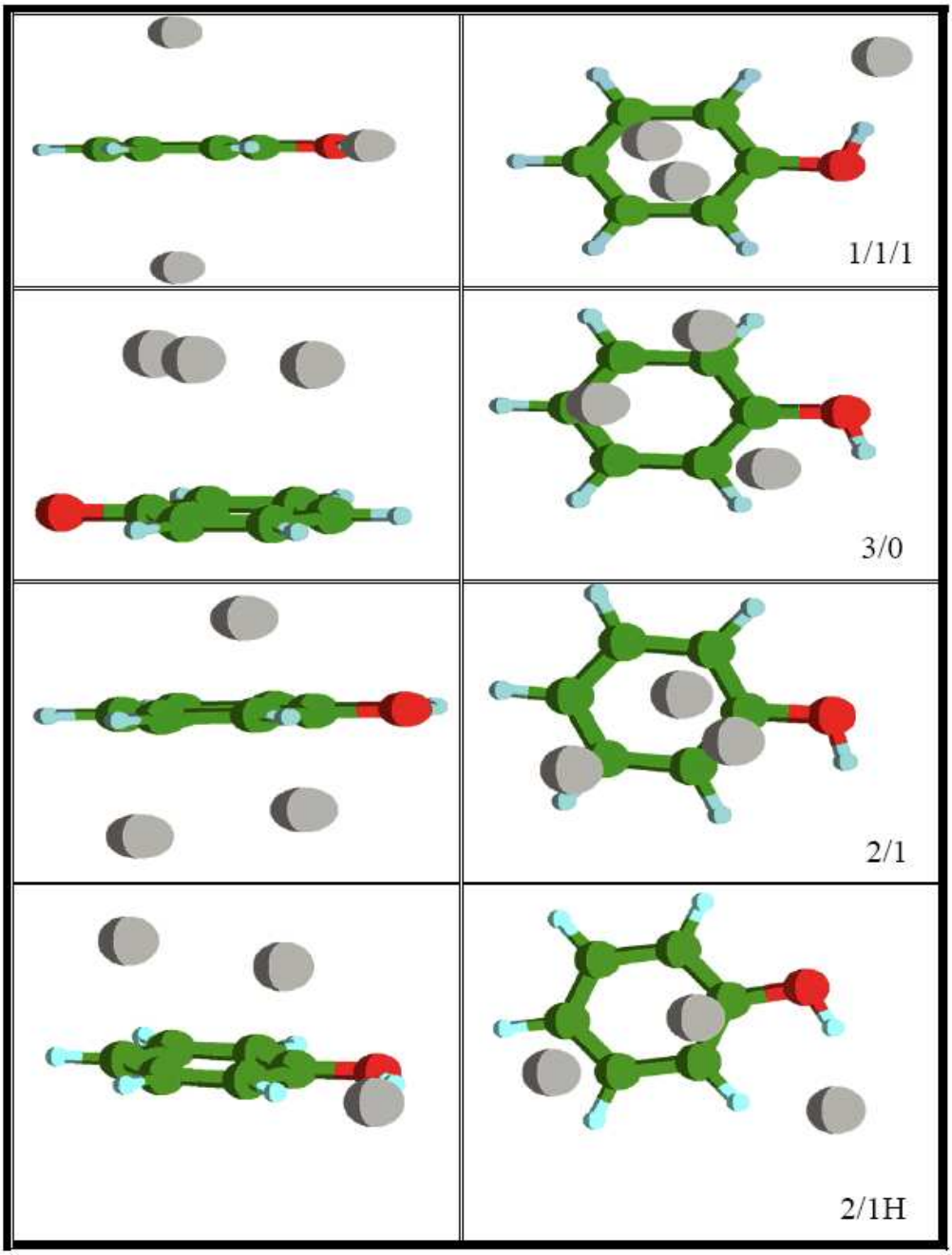

Figure 8.1: Schematic diagram of the geometric structures of phenol…Ar_3. All the geometries are calculated using RMP2/aug-cc-pDZ level and RMP2 / aug-cc-pTZ for the argon atoms.

The energies for each isomer (Table 8.2) are calculated relative to the 1/1/1 isomers, which represents the most stable isomer. Unexpectedly, while the geometries 2/1 and 2/1H almost maintain the same relative energy using the two different basis sets, a significant change in relative energy is observed for the conformer 3/0 (3.4 kJ/ mol^{-1} and 0.4 kJ/ mol^{-1} for the geometries calculated using RI-MP2/aug-cc-pVDZ and RI-MP2/aug-cc-pVTZ level, respectively).

Table 8.2: Relative energies for the isomers of the neutral phenol…Ar_3 complex.

Isomer	**RI-MP2/aug-cc-pVDZ kJ mol^{-1}**	**RI-MP2/aug-cc-pVTZ kJ mol^{-1}**
1-1-1	0	0
3-0	3.4	0.4
2-1	0.8	1
2-1H	3.5	3.4

8.2.2 High resolution REMPI spectrum

The high resolution two colour (1+1') REMPI spectrum of the origin band of the $S_1 \leftarrow S_0$ transition (36373.5 ± 0.5 cm^{-1}) shown in Figure 9.2 was obtained using the same experimental set-up and conditions described before (Chapter 3 and 6) and recorded by scanning the laser in increments of 0.005 cm^{-1}. The spectrum has been normalised to dye laser intensity and is smoothed by a three point average. The laser was calibrated with reference to simultaneously recorded iodine absorption spectra, corrected from air to vacuum.

The high resolution REMPI spectrum of phenol…Ar_3 reported in Figure 8.2, differently from the case of phenol…Ar and phenol…Ar_2,[4,5] where a strong Q-branch can be

observed (c-type band profile) in the high resolution spectra gives a hybrid type rotational contour.

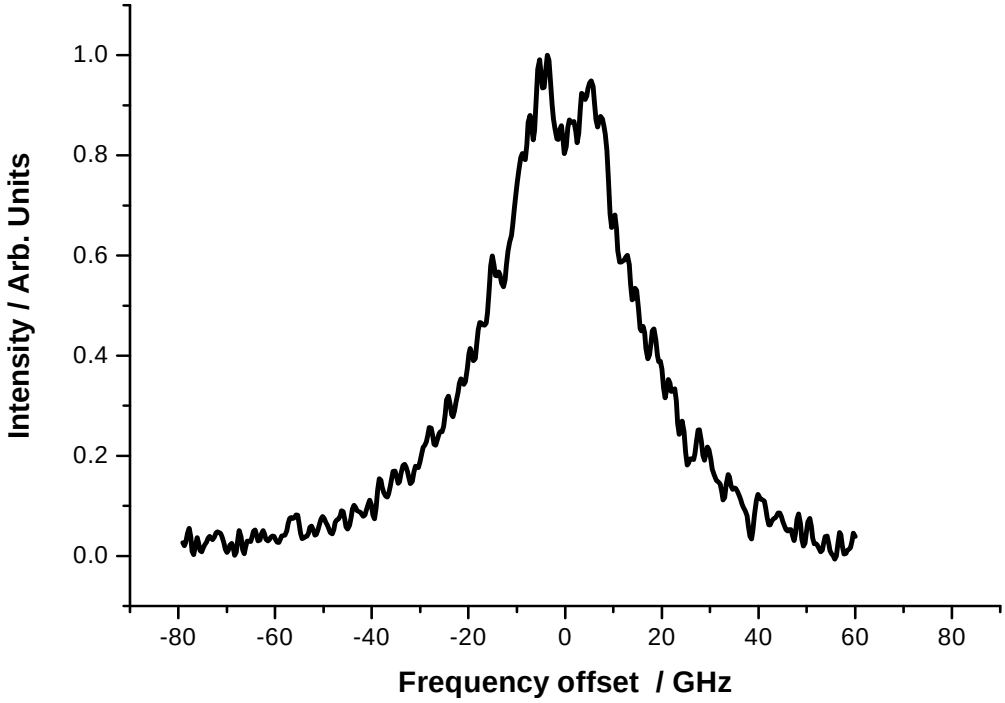

Figure 8.2: High resolution two-colour (1+1') REMPI spectrum of the $S_1 0^0$ band origin of phenol…Ar_3.

8.2.3 Analysis of the rotational profile of the origin band measured in the REMPI spectrum

The best-fit simulated rotational contour spectra reported in Figure 8.3 were generated with in-house software[8] (see appendix). The origin band rotational profile was determined assuming the transition moments of bare phenol (practically once we know the orientation of the transition moment in the bare phenol molecule, we can transfer this information to the complex due to the fact that the transition involved is located inside the phenol molecule and it is only slightly affected by solvation of the argon atom).

The *ab initio* simulations employ S_1 rotational constants which are 2% smaller than the S_0 rotational constants. The transition dipole moment and the temperature used for the simulation spectra are reported in Table 8.3. The simulated band contours presented in Figure 8.3 were obtained using a laser line width of 1200 MHz and a Lorentzian line shape function. Experimental and simulated spectra are presented relative to the band centre which occurs at 36373.5 ± 0.5 cm^{-1}.

The 3/0 structure of phenol…Ar_3 gives a simulated spectrum which follows the shape of the experimental data and, for the most part, the intensity very well offering the most reasonable hybrid rotational contour (see figure 8.3b and μ_a^2:μ_b^2:μ_c^2 =43:23:24). For the 2/1 and 1//1/1 (figure 8.3a and 8.3b), the spectra are very similar shape each other and the rotational contour is dominated by a c-type (it also confirmed by $\mu_c^2 > \mu_a^2$ and μ_b^2). The 2/1 H structure also gives a reasonable rotational contour, however the rotational constants obtained from the fit simulation are far from the computed *ab initio* values (a change of 25 %, 15%, 10% is observed on A, B, C respectively while a changes < 8% are observed for the rotational constants for the other structures). The significant change is a limit for the reliability of this last fit simulation. Additionally, according to the *ab initio* calculations employing the higher level of theory (RI-MP2/aug-cc-pVTZ level), this geometry represents the least stable structure.

It seems conclusive that phenol…Ar_3 adopts a structure 3/0 even if the *ab initio* calculations supported a 1/1/1 structure. The fact that as the conformers of phenol…Ar_n (*n*=1-2) in the neutral and in the first excited state, in the phenol…Ar_3 cluster, the argon atoms largely prefer to interact with the aromatic ring, instead of hydrogen bond with

the O-H substituent, can be explained with a possible mechanism of formation of this cluster, which involves the argon atoms creating a bond before interact with phenol.

Table 8.3: Transitional dipole moment and temperatures used to calculate the fit simulated spectra for each isomer.

Isomer	μ_A	μ_B	μ_C	T / °K
3/0	1.6	1.4	1.2	3
2/1	0.5	1.4	1.9	3
1/1/1	0.4	1.2	2	3
2/1H	2.1	0.4	1.1	3

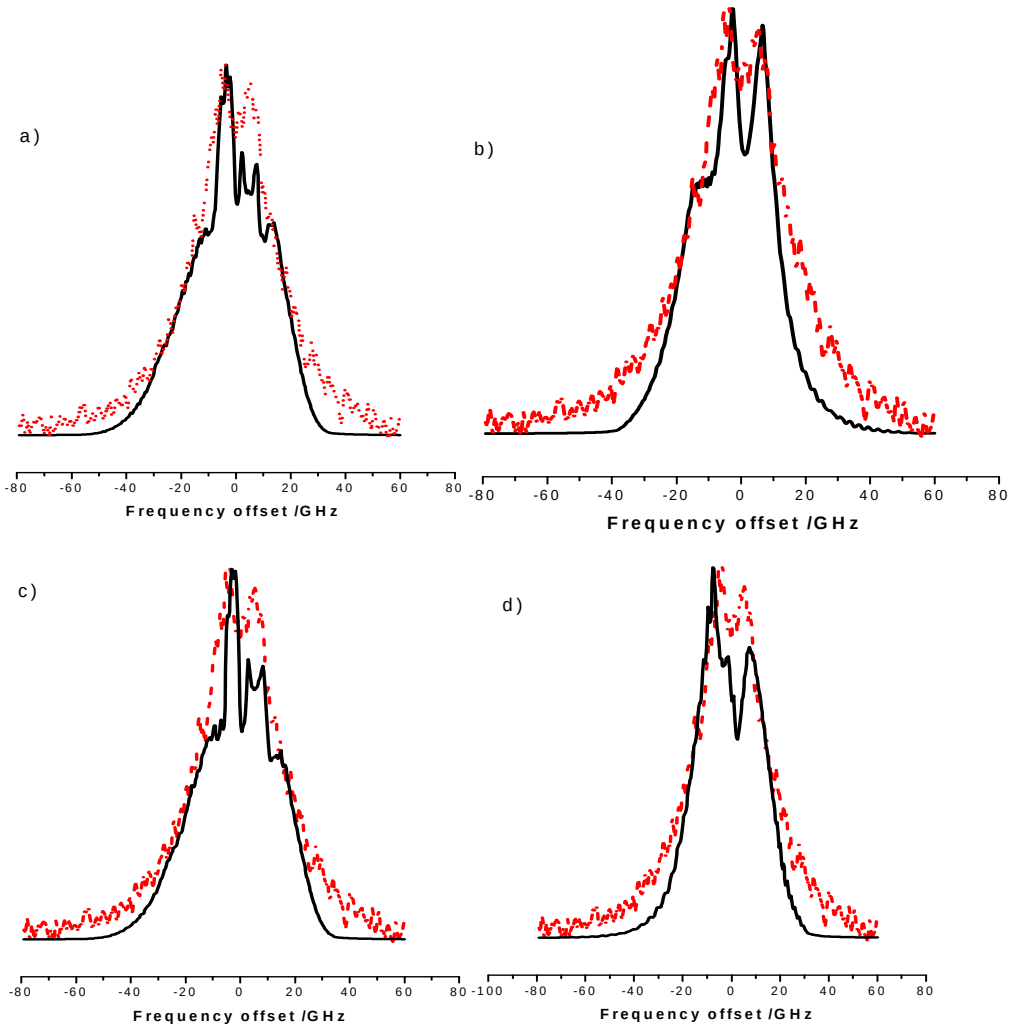

Figure 8.3: Comparison of the experimental (dotted line) and simulated (continuous line) origin band rotational profiles using S_0 ab initio parameters from a) 2/1 structure, b) 3/0 structrure, c) 1/1/1 structure and d) 2/1H structure.

8.3 Summary and further discussion

The structure for phenol…Ar_3 was determined by comparison between the experimentally obtained rotational band contour and the ones calculated with the rotational constants which were determined from the different isomers. From this comparison, the structure with three argon atoms located on the same side of the ring was assigned as the structure best describing this cluster. This result supports the assumption made from an analysis of the lower resolution REMPI studies (chapter 6). It has been demonstrate again that in a context of spectroscopic study, rotational band contour analysis gives additional information on the structure of the cluster.

8.5 References

[1] D. W. Pratt, *Annu. Rev. Phys. Chem.*,1999, **49,** 481.

[2] M.R. Hockiridge, S. M. Knight, E. G. Robertson, J. P. Simons, J. McCombie and M. Walker, *Phys. Chem. Chem. Phys*., 1. 1999, **1**, 407.

[3] A. Bacon and J. M. Hollas, *Faraday Discuss. Chem. Soc*., 1988, **86**, 129.

[4] M. S. Ford, S. R. Haines, I. Pugliesi, C. E. H. Dessent and K. Müller-Dethlefts, *J. Electron Spectrosc. Relat. Phenom*., 2000, **112,** 231.

[5] I. Kalkman, C. Brand, T. C. Vu, W. L. Meerts, Y. N. Svartsov, O. Dopfer, X. Tong K. Müller-Dethlefts, S. Grimme and M Schmitt. *J. Chem. Phys.*, 224303, **130**, 2009.

[6] G. Bedern, W. L. Meerts, M. Schmitt and Kleinermanns, *J. Chem. Phys.*, 1996, **104**, 972.

[7] R. Ahlrichs, M. Bär, M. Häser, H. Horn and C. Kölmel, *Chem. Phys. Lett*., 1989, **169**, 165.

[8] M. S. Ford, *Ph.D thesis*, University of York, 2002.

Chapter 9

Dissociation pathways in the Phenol…Ar_4 cation complex

9.1 Introduction

In this Chapter the dissociation process of phenol$^+$…Ar_4 is investigated using PIE/MATI spectroscopy. An interpretation of the surprising values for the dissociation thresholds is given, focusing on the possible geometry and interactions adopted by the argon atoms in the cluster.

9.2 Results

9.2.1 PIE spectra

The experimental conditions employed to produce phenol…Ar_4 cluster for recording PIE and MATI spectra are identical to those described in Chapter 6.

Figure 9.1 shows the PIE spectra *via* the origin of the S_1 state of phenol$^+$…Ar_4 at 36338.8 cm^{-1} simultaneously recorded at the mass channel of the phenol$^+$…Ar_4 parent ion (254 u), and phenol$^+$… Ar_n (n=0-3) fragment ion channels. The first rise in the PIE spectrum of phenol$^+$…Ar_4 is observed at 67760 ± 50 cm^{-1} and is assigned to the IE in very good agreement with the value obtained in Chapter 6. The structures of the PIE

spectra at the mass channel of phenol$^+$… Ar_3, phenol$^+$… Ar_2, phenol$^+$… Ar and phenol$^+$ rise at 67980 ± 50 cm^{-1}, 68180 ± 50 cm^{-1}, 68380 ± 50 cm^{-1} and 68595 ± 50 cm^{-1}, respectively.

9.2.2 MATI spectra

To obtain more accurate values for the dissociation thresholds of phenol$^+$…Ar_4, the MATI spectra at the phenol$^+$…Ar_4 mass channel and at the phenol$^+$ fragment channel *via* the origin of S_1 state of phenol…Ar_4 were simultaneously recorded.

The MATI spectrum recorded at the mass of phenol$^+$…Ar_4 is shown in Figure 9.2 (a similar spectrum has been already reported in Chapter 6). The spectrum is characterized by a very broad structure therefore it is difficult to distinguish individual features assignable to possible vibrational modes. As mentioned previously, the IE value obtained from this spectrum differs from the value acquired from the PIE spectrum. The first peak in the MATI spectrum recorded at the mass channel of phenol$^+$…Ar_4 can be seen at 67948 ± 20 cm^{-1} which is about 187 cm^{-1} higher than the IE value determined by PIE spectroscopy. It was explained that the more reliable candidate for the IE is the value obtained from the PIE spectrum (67760 ± 50 cm^{-1}). For this reason the ion internal energy of the MATI spectrum of phenol$^+$…Ar_4 is relative to the IE value taken from the PIE spectrum. The phenol$^+$ fragment from dissociated phenol$^+$…Ar_4 is also displayed in Figure 9.2. Two sharp peaks can be observed. The first peak is at 856 ± 3 cm^{-1} above the IE of phenol$^+$…Ar_4 and another peak is present in the spectrum at 872 ± 3 cm^{-1} above the IE of phenol$^+$…Ar_4.

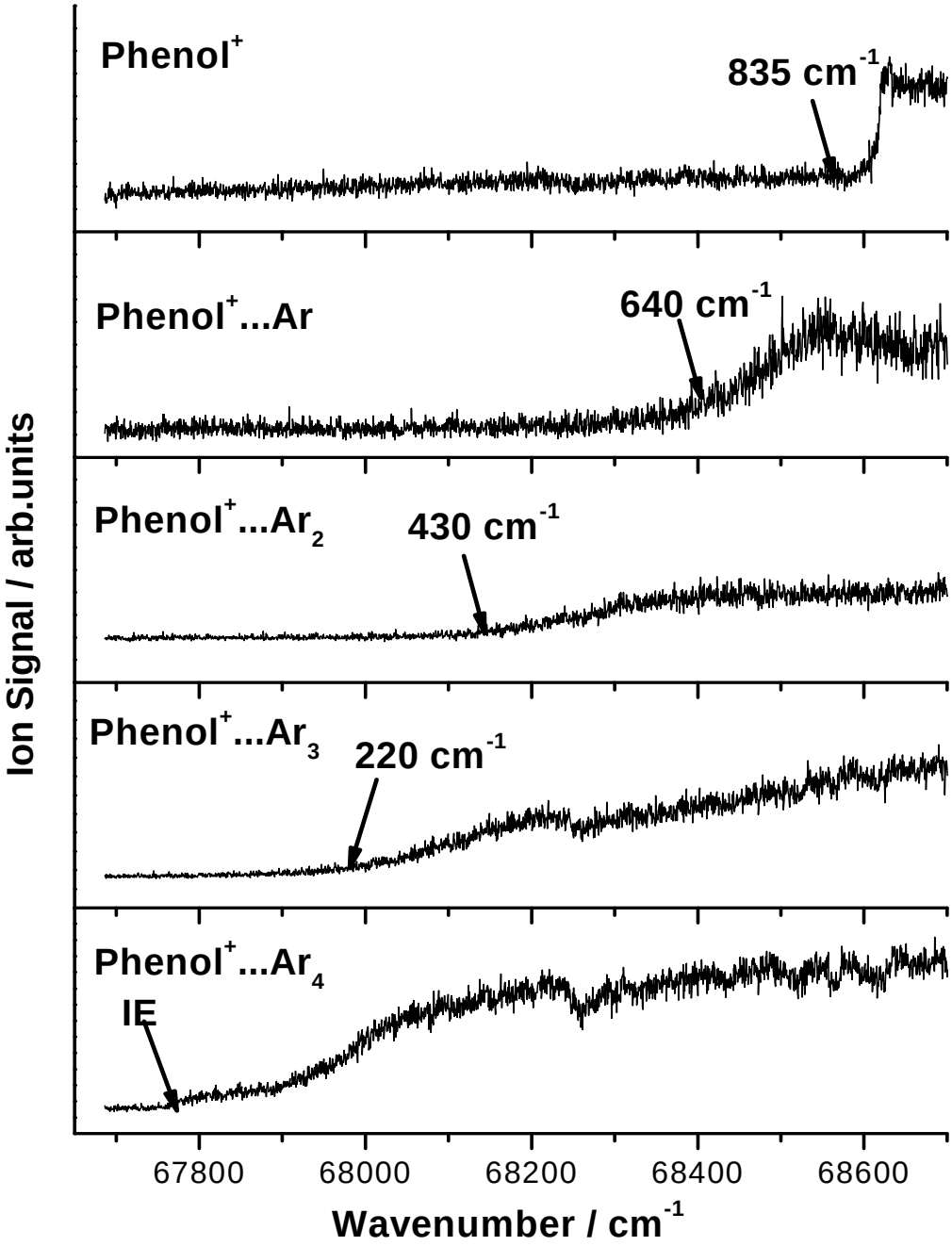

Figure 9.1: PIE spectra of phenol$^+$…Ar_4 recorded at the cluster mass and the fragment masses of phenol$^+$…Ar_n (n=0-3).

.

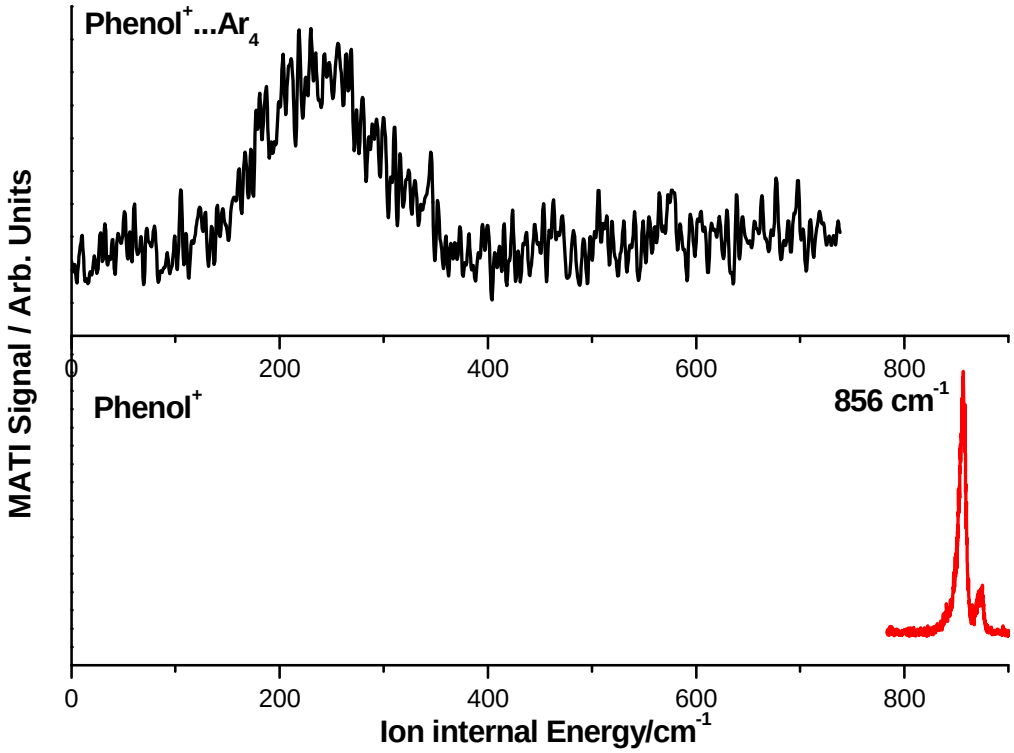

Figure 9.2: MATI spectra of phenol$^+$…Ar_4 *via* the $S_1 0^0$ state recorded at the cluster mass and the fragment mass phenol$^+$. The ion internal energy is considered relative to the IE energy determined by PIE spectroscopy.

9.3 Discussion

9.3.2 Dissociation process

A summary of the energetics for the dissociation process of phenol$^+$…Ar_4 is shown in detail in Figure 9.3.

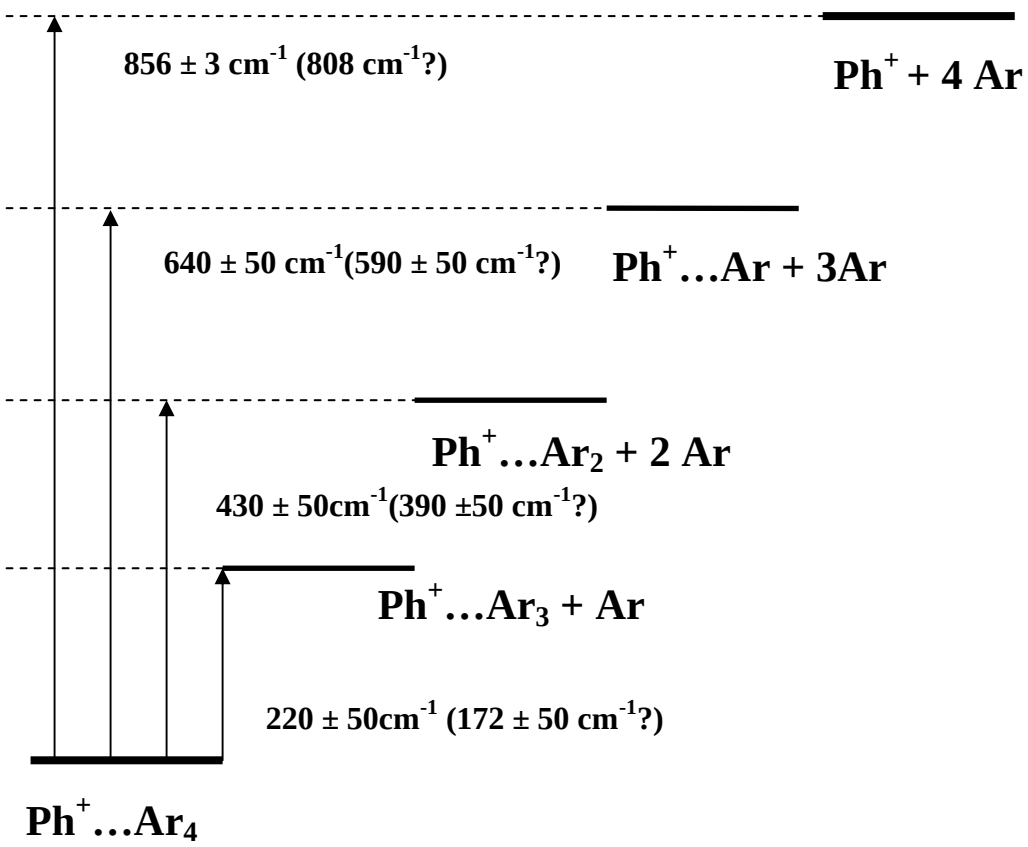

Figure 9.3: Schematic of the dissociation process of the phenol$^+$…Ar_4 cluster.

Dissociation energy for the loss of one argon atom

From the PIE spectrum at the mass channel of phenol$^+$…Ar_3 we can determine that the dissociation threshold for the loss of one argon atom is 220 ± 50 cm^{-1}. As deduced from Table 9.1, this value differs by approximately 315 cm^{-1} from the dissociation threshold one argon from the phenol$^+$...Ar cluster (535 cm^{-1}),[1] and is very similar to the dissociation threshold for the loss of one argon atom for phenol…Ar_n (*n*=2-3) (208 and 190 cm^{-1} are the values for phenol$^+$…Ar_2 and phenol$^+$…Ar_3 respectively). This small dissociation threshold was explained for phenol$^+$…Ar_n (*n*=2-3) by assuming π→H isomerisation. The value for the dissociation threshold for the loss of one argon atom

from phenol$^+$…Ar_4 is comparable to those of phenol…Ar_n (n=2-3) so the π→H isomerisation process could be tentatively proposed upon initial analysis.

Table 9.1: Summary of the dissociation thresholds for phenol$^+$…Ar_n (n=1-4).

	Energy (cm^{-1}) for the loss of			
Cluster	**1 Ar atom**	**2 Ar atoms**	**3 Ar atoms**	**4 Ar atoms**
Phenol…Ar	535			
Phenol…Ar_2	210	1105		
Phenol…Ar_3	190	860	1730	
Phenol…Ar_4	220 (**172 ± 50 cm^{-1}?**)	430(**390 ±50 cm^{-1}?**)	640(**590 ± 50 cm^{-1}?**)	856 (**808**?)

Dissociation energy for the loss of two and three argon atoms

From the PIE spectrum at the mass channel of phenol$^+$…Ar_2 fragment, the dissociation thresholds for the loss of two argon atoms has been found to be 430 ± 50 cm^{-1}. This value is approximately twice the dissociation threshold for the loss of one argon atom. This trend is still valid if the dissociation threshold for the loss of three argon atoms is considered. Also in this case the value obtained from the PIE spectrum at the phenol$^+$…Ar mass channel is 640 ± 50 cm^{-1}, which is almost three times bigger than that for the loss of one argon atom. The dissociation threshold for the loss of two argon atoms is around 400 cm^{-1} smaller than the corresponding value found for phenol$^+$…Ar_3. This surprising result cannot be explained considering a π→H isomerisation as a possible geometry rearrangement of this system. This is additionally supported by the very low energy value obtained for the loss of three argon atoms which suggests that the location of the argon atoms with respect to the aromatic ring may differ from the other phenol$^+$…Ar_n (n=1-3) clusters.

Dissociation energy for the loss of four argon atoms and a possible mechanism for the fragmentation process

A very surprising value can be found when the dissociation energy for the loss of four argon atoms is considered. The value obtained from the PIE spectrum recorded at the mass channel of phenol$^+$ fragment is 835 ± 50 cm^{-1} and is in full agreement with the accurate value of 856 ± 3 cm^{-1} obtained from analysis of the MATI spectrum. This value is two times smaller than the dissociation energy for the loss of three argon atoms in phenol$^+$…Ar_3 (1730 cm^{-1}) and even smaller than the dissociation energy for the loss of both argon atoms from phenol$^+$…Ar_2 (~1105 cm^{-1}).

This data additionally supports the fact that the argon atoms indeed interact with the phenol differently than the other phenol$^+$…Ar_n (n=1-3) clusters. If we list all the possible van der Waals structures the argon atoms can adopt with respect to the aromatic ring, there are three possible geometries: a 2/2 structure where the two argon atoms are located on one side of the aromatic ring and the other two are on the opposite side; a 3/1 structure where three argon atoms are bonded to one side of the phenol and the other argon is on the opposite side; the last possible structure 4/0 is represented by the four argon atoms adopting a geometry where the four atoms are on the same side of the aromatic ring.

The value observed for the dissociation energies exclude the 2/2 and 3/1 structures as initial geometries. In fact, in these cases, the nature of the bonds between the argon atoms and phenol would not differ much from phenol$^+$…Ar_n (n=2-3) and the magnitude of the dissociation threshold should be similar to those clusters. Furthermore, if it is considered that the low energy values for the loss of one, two and three argon atoms would be due to rearrangement of the structure of this cluster, it would be expected a

much higher value for the dissociation energies regarding the loss of the four argon atoms. In particular, as it has been observed for phenol$^+$…Ar_2 and phenol$^+$…Ar_3, any rearrangement does not affect the final fragmentation energy which is almost *n*-times the dissociation energy for the loss of one argon atom in phenol$^+$…Ar (1105 cm^{-1} and 1730 cm^{-1} are the dissociation energies for the loss of two argon atoms from phenol$^+$…Ar_2 and three argon atoms from phenol$^+$…Ar_3 respectively, which are almost two and three times bigger then the energetic value obtained for the loss of one argon atom in phenol$^+$…Ar (535 cm^{-1})). [1] The only geometry that may be able to explain the experimental data is the 4/0 structure.

In aniline…Ar_4, one of the conformers was observed to have a small $S_1 0^0$ red shift of 3 cm^{-1} compared the aniline origin, which corresponds to the most stable 4/0 structure and computational calculations revealed that the four argon atoms adopt a rhombus-like arrangement in this structure.[2,3] A small $S_1 0^0$ red shift of 10 cm^{-1} was observed for phenol…Ar_4 (see Chapter 6) compared to the $S_1 0^0$ of the phenol monomer therefore a similar structure could be a reasonable candidate for phenol…Ar_4.

As already mentioned in chapter 6, the preference for single-sided or double-sided solvation depends on the expansion conditions. High Ar backing pressure favors single-side solvated species, i.e., the formation of (*n*/0) isomers, because first the Ar_n cluster are formed in the expansion and then phenol is attached to the surface of this cluster. In the present work, the Ar backing pressure of > 2 bar corresponds to the high pressure regime, leading to the preferential formation of the (4/0) isomer.

From the values observed for the dissociation thresholds of phenol^{+}…Ar_4 it can be inferred that the argon atoms must be located in equivalent positions to maintain the additivity for the dissociation thresholds.

This assumption is supported by considerations on the geometries adopted in Argon atoms clusters. Free gases rare clusters have been largely investigated[4,5,6] and it has been found that cluster of 4-55 atoms assume structures with high symmetry. Thus for example, a cluster with 5 atoms prefers a trigonal bypiramidal, 6 an octahedral and in particular, 4 a tetrahedral.[7] This is also confirmed by a simple calculation performed on an isolated system of four argon atoms. Figure 9.4 shows a schematic representation of the Ar_4 cluster. Calculations on this system were performed employing the Gaussian 03 program. The geometry optimization of Ar_4 was calculated at the RI-MP2/aug-cc-pVTZ level including counterpoise correction to avoid basis set superposition error (BSSE).[8]

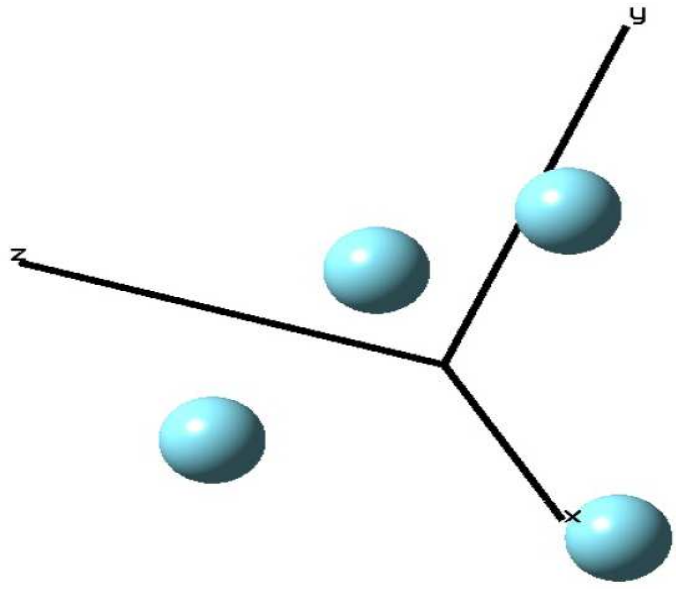

Figure 9.4: Schematic representation of the geometry of Ar_4 cluster. The geometry was calculated using aug-cc-pVTZ level. The calculation of the minimum energy includes BSSE.

It appears that the four argon atoms largely prefer to adopt a structure such as a tetrahedron instead of geometry where all the argon atoms are located in the same plane (such as rhombus-like structure).

The calculated distance between the argon atoms in the geometry reported in Figure 9.4 is around 3.8 Å, which is slightly bigger than the distance between the argon atom and the aromatic ring in phenol…Ar (3.3 Å).[9] If we consider this type of geometry in the phenol$^{(+)}$…Ar_4 where only one argon atom is closer to the aromatic ring; the other argon atoms located twice as far from the ring would be only slightly affect by a non covalent interaction with phenol. Only the closest argon atom would establish a strong interaction with the aromatic ring, supporting the small values found for the dissociation energies.

Furthermore, considering that the bond energy in an argon dimer is around 100 cm^{-1},[10] the value for the dissociation energy for the loss of four argon atoms is just slightly different than 3 × 100 cm^{-1} (bond energy bond of each argon atom with the closest argon atom to the aromatic ring) + 535 cm^{-1} (dissociation energy for the loss of one argon atom from phenol$^+$…Ar).

9.3.3 Intramolecular vibrational modes

Further observations on the results obtained can be made from Figure 9.5. The spectrum in red in Figure 9.5 shows the MATI spectrum for phenol$^+$ monomer and the spectrum in black is the MATI spectrum of the phenol$^+$ from the fragmented phenol$^+$…Ar_4. The intense feature at 808 cm^{-1} in the MATI spectrum of the phenol monomer is assigned to the in-plane mode 12[11] is shifted by ~ 48 cm^{-1} compared to the

most intense peak in the spectrum recorded at the mass fragment channel of phenol$^+$ from phenol$^+$…Ar_4 (no shifts are expected for in-plane modes in a structure where all the argon atoms are located on the top of the aromatic ring). This difference is within the experimental error. In fact the IE for phenol$^+$…Ar_4 has been obtained from the PIE (with an error range of ± 50 cm^{-1}). So we can assume that the most intense peak in the MATI spectrum of the fragment phenol$^+$…Ar_4 corresponds to the intramolecular mode 12 and as a consequence, the value for the dissociation energy can be given at 808 cm^{-1}, leaving unaltered the considerations made on the dissociation process of this cluster. Additionally the peak observed at 17 cm^{-1} above the 12 mode can be reasonable assigned to the in-plane mode 18 b^2 (as expected, no shift is again observed in this case observed if we compare this frequency with the 18 b^2 mode of phenol$^+$). If a shift of the IE energy for phenol…Ar_4 of ~ 50 cm^{-1} is assumed, the value for the dissociation energy for the loss of one, two and three argon atoms would be shifted by ~50 cm^{-1} (172 ± 50 cm^{-1}, 390 ±50 cm^{-1}, 590 ± 50 cm^{-1} would represent the possible values for the dissociation thresholds of one, two and three argon atoms).

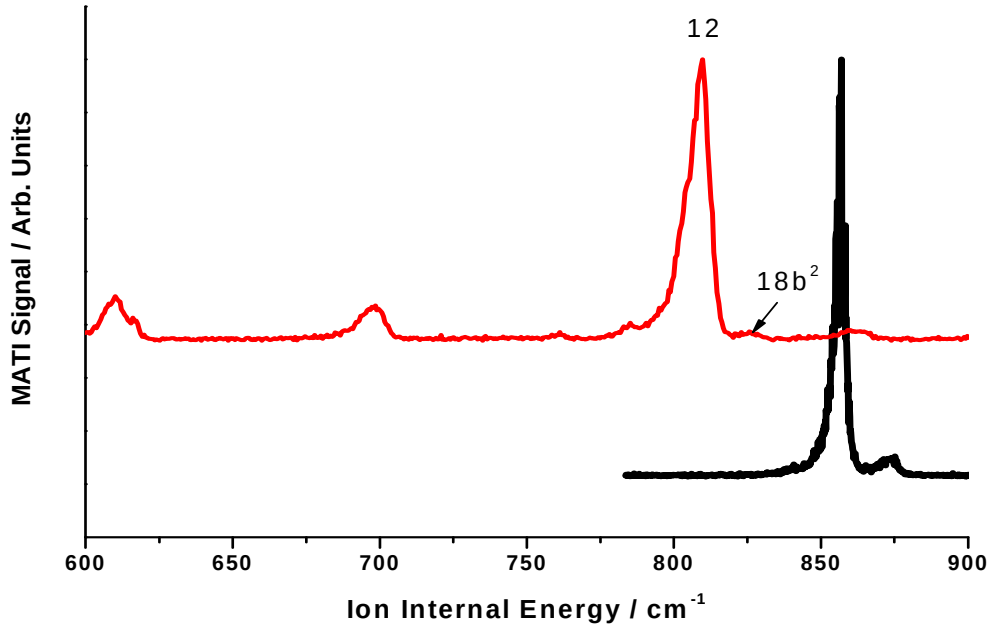

Figure 9.5: MATI spectra of phenol$^+$ (red) and phenol$^+$ (black) from dissociated phenol$^+$…Ar$_4$.

9.4 Further discussion

Analysis of the bands observed in the MATI spectrum of phenol$^+$…Ar$_4$ recorded at the phenol mass reveals a band width of about 20 cm^{-1}. These sharp peaks were not observed in the case of the MATI spectra of phenol$^+$…Ar$_n$ (n = 2, 3) recorded at the fragment masses. In this case, the structures characterizing the spectra were very broad (~50 cm^{-1} for phenol$^+$…Ar$_2$ and ~150 cm^{-1} for phenol$^+$…Ar$_3$). As already mentioned, each peak corresponds to a fundamental vibration followed by the intermolecular vibrations of the cation state. The observed MATI peaks in phenol$^+$…Ar$_4$ should be even broader. Phenol$^+$…Ar$_4$ has more low frequency van der Waals modes in the cation state as can be deduced by considering the fact that the MATI spectrum of phenol$^+$…Ar$_4$ via the $S_1 0^0$ intermediate state is characterized by a broad structure.

For these reasons, further spectroscopic investigation is required to confirm that the MATI signal observed at the mass channel of $phenol^+$ is indeed produced by fragmentation of $phenol^+…Ar_4$.

9.5 Summary

The difficulties in detecting a MATI signal at the masses of $phenol^+…Ar_n$ (n=1-3) fragments of $phenol^+…Ar_4$ did not make it possible to obtain accurate values for the dissociation thresholds for the loss of one, two and three argon atoms; however approximate dissociation thresholds were found by using PIE spectroscopy. Surprising energy values were obtained for the dissociation process. An accurate value (808 cm^{-1}) for the dissociation energy for the loss of the four argon atoms was obtained by analysing the MATI spectrum recorded at the mass channel of phenol fragment of the $phenol^+…Ar_4$. These surprising measurements were explained by proposing a structure for $phenol^+…Ar_4$ where all argon atoms are located on the same side of the ring in a tetrahedron-like structure. Further investigation is necessary to confirm the results obtained from MATI spectroscopy.

9.6 References

[1] C. E. H. Dessent, S. R. Haines and K. Müller-Dethlefs, *Chem. Phys. Lett.*, 1999, **315**, 103.

[2] S. Douin, P. Parneix, F. G. Amar and Ph. Brèchignac. *J. Phys. Chem. A*, 1997, **101**, 122.

[3] P. Hermine, P. Parneix, B. Countant, F. G. Amar and Ph. Brèchignac., *Z. Phys. D. At. Mol. Cluster*, 1992, **22**, 529.

[4] R. D. Etters and J. Kaelberer, *Phys. Rev. A*, 1977, **11**, 1068.

[5] J. D. Honeycutt and H. C. Andersen**,** *Chem. Phys. Lett.*.**,** 1984**, 108,** 535.

[6] H. Cheng and R. S. Berry, *Phys. Rev. A*, 1992, **45,** 7969**.**

[7] C. Rajappa, S. Bandyopadhyay and Y. Subramanian, Bull. Mater. Sci., 1997, **6**, 845.

[8] S. F. Boys and F. Bernardi, *Mol. Phys*. 1970, **19**, 553.

[9] J. Cerny, X. Tong, P. Hobza and K. Müller-Dethlefs, *Phys. Chem. Chem., Phys.*, 2008, **10**, 2780.

[10] P.R. Herman, P.E. Larocque and B.P. Stoicheff, *J. Chem. Phys*., 1988, **89**, 4535.

[11] O. Dopfer, PhD Thesis, 1994, Technische Universität München, München.

Chapter 10

Phenol…CH_4

10.1 Introduction

Methane is a non-polar 'spherical' molecule and as a consequence its interaction with aromatic systems is expected to be similar to those for rare gases such as argon. However the larger polarizability of methane leads to stronger interactions ($\alpha_L/4\pi\varepsilon_0$= 1.63 and 2.6 Å[1] for L= Ar and CH_4).[2] Spectroscopic information regarding the CH_4 complex with aromatic molecules such as toluidine,[3] cresol,[3] aniline,[4,5] and phenol[6,7] can be found in previous works.

In particular, previous reports suggest that phenol…CH_4 has a π-bound equilibrium structure in the neutral ground state S_0.[7] In the ionic state D_0, only the π-bound phenol$^+$… CH_4 will therefore be generated due to the restrictions imposed by the Frank-Condon principle which strongly favours vertical transitions. However, similar to phenol$^+$…Ar, the global minimum of phenol$^+$…CH_4 is expected to have a H-bound geometry as shown by IR spectroscopy of clusters generated in the electron impact source.[7] Information regarding the spectral shift of the band origin of the transition $S_1 \leftarrow S_0$ of phenol…CH_4 relative to the phenol monomer were obtained using stimulated raman−UV double resonance spectroscopy. [6]

In this chapter, a description of the recent results obtained by REMPI and MATI spectroscopy is reported. To supplement these results, Fujii and co-workers[8] have performed REMPI-IR dip spectroscopy on this cluster system. An analysis of the spectra obtained by REMPI-IR dip. spectroscopy are also found in this chapter for a complete description of the geometries adopted in phenol$^{(+)}$…CH_4 with emphasis on the photoionisation-induced site-swiching from π-bonding to H-bonding.

10.2 Results

10.2.1 REMPI Spectrum

A two colour (1+1') R2PI spectrum was recorded as first step preceding investigation of the ion ground state by MATI spectroscopy.

Phenol…CH_4 clusters were produced in a skimmed supersonic jet expansion of phenol seeded in a 5% methane/argon mixture with pressure between 1-2 bar. The sample holder containing phenol was heated at a temperature of 320-340 K. An appropriate value for the energy of the second laser (32200 cm^{-1}) was chosen to reduce fragmentation from higher clusters.

The two-colour (1+1') R2PI spectrum of phenol…CH_4 is shown in Figure 10.1. The most intense feature occurs at 36288.3 ± 0.5 cm^{-1} and is assigned to the band origin (this value is in fully agreement with the results obtained in Ref. 6). The first sequence of bands can be clearly identified in the low energy part of the spectrum (in the range between 22 cm^{-1} and 110 cm^{-1} above the band origin) and arise due to the intermolecular modes of methane with respect to the phenol molecule. The most intense feature can be observed at around 53 cm^{-1} above the band origin. The other bands

observed in the spectrum at higher energies are assigned to the intramolecular modes of phenol[9] (see Table 10.1 for frequencies and assignments); the most intense band in this region can be observed at 476 cm^{-1} and it corresponds to the mode 6a.

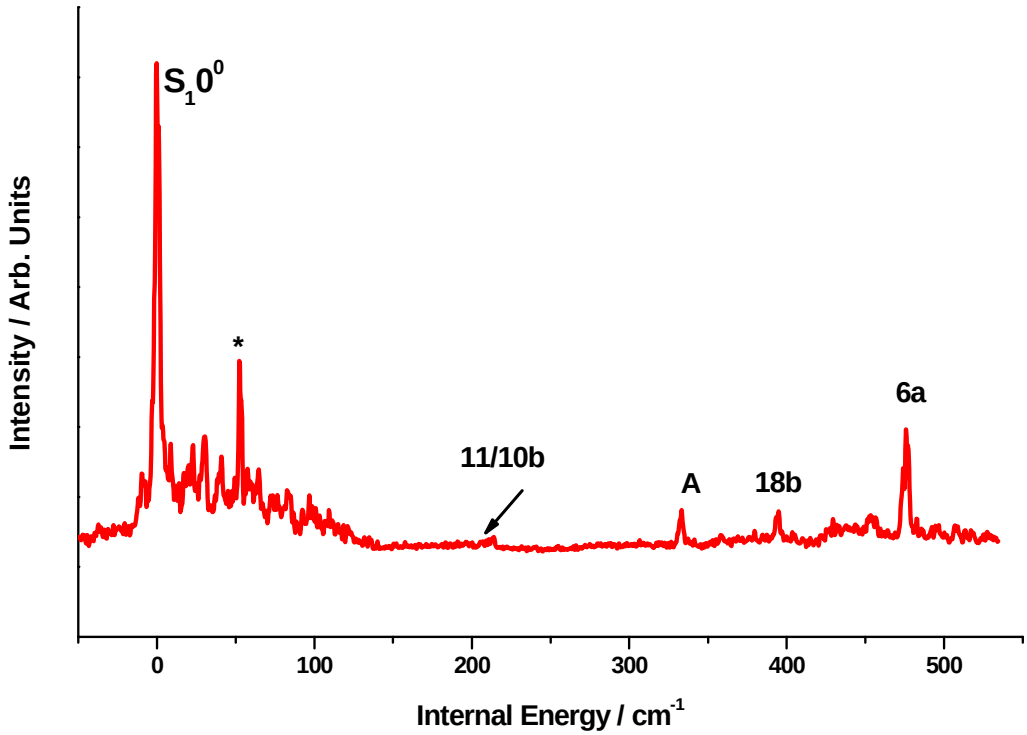

Figure 10.1: (1+1') REMPI spectrum of phenol…CH_4 of the first electronically excited state including the assignment of the intramolecular vibrational modes.

Table 10.1: Frequencies and assignments of the vibrational bands observed in the REMPI spectrum of phenol…CH_4 and phenol monomer.

Frequency / cm^{-1}		
REMPI spectrum Phenol…CH_4	REMPI spectrum Phenol monomer	Assignment
214	208	10b[a]/11[b]
333	324	A[c]
395	395	18b
476	476	6a

[a] Nomenclature of Varsanyi.[10]
[b] Nomenclature of Wilson.[11]
[c] The assignment is not certain.[12,13]

10.2.2 PIE and MATI Spectra

PIE and MATI spectroscopy were used to record spectra of the D_0 state of the phenol$^+$…CH_4. The pulse sequence timings and field strengths used to obtain the MATI spectrum are identical to those previously described. Ionisation energies have been corrected for fields effects using the formula $\Delta E = 4F^{1/2}$. [14]

The PIE and MATI spectra of phenol$^+$…CH_4, recorded by ionising *via* the $S_1 0^0$ intermediate state at 36288.3 ± 0.5 cm^{-1} are shown in Figure 10. 2. The first clear step in the PIE spectrum can be observed at 68331 ± 30 cm^{-1} providing an approximate value for the ionisation energy of phenol$^+$…CH_4.

A more accurate value for the ionisation energy can be obtained by analyzing the MATI spectrum. The MATI spectrum is characterized by a broad structure of about 100 cm^{-1} width; however six individual bands can be certainly identified with an equal spacing of about 15 cm^{-1} as shown in Figure 11.3). The first feature at 68341 ± 5 cm^{-1} can be assigned to the ionisation energy due to the fact that no further bands are observed at lower energy in the spectrum in agreement with the value found in the PIE spectrum. This band does not represent the most prominent feature in the spectrum as was also observed in the MATI spectra of phenol…Ar_n (n = 2-3) (see Chapters 4 and 6).

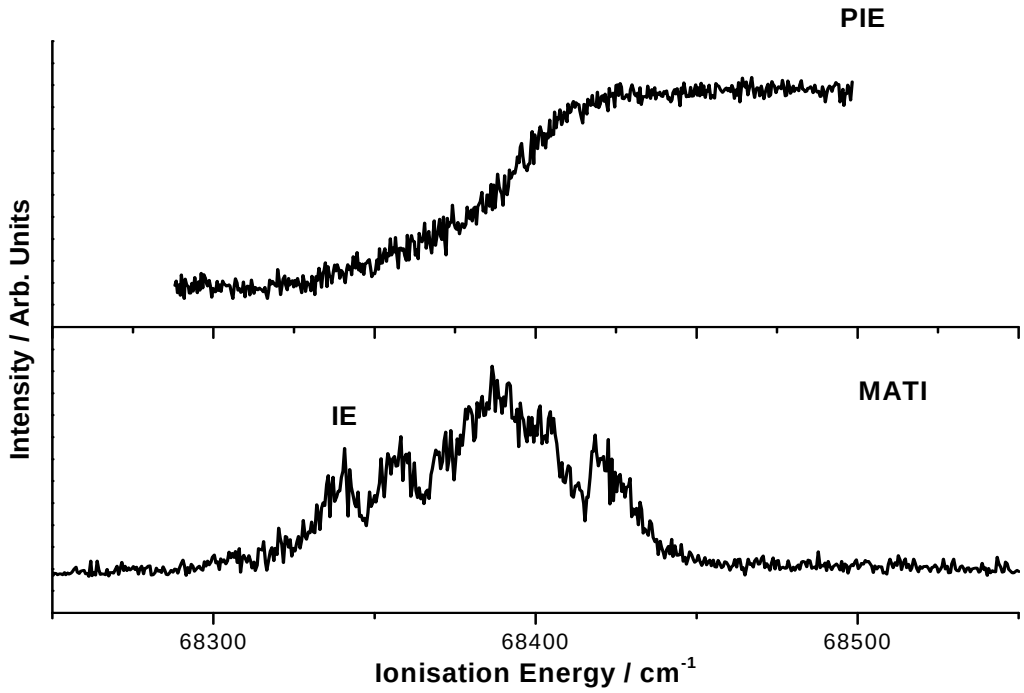

Figure 10.2: PIE and MATI spectra of phenol$^+$…CH_4 recorded by ionising *via* the $S_1 0^0$ transition.

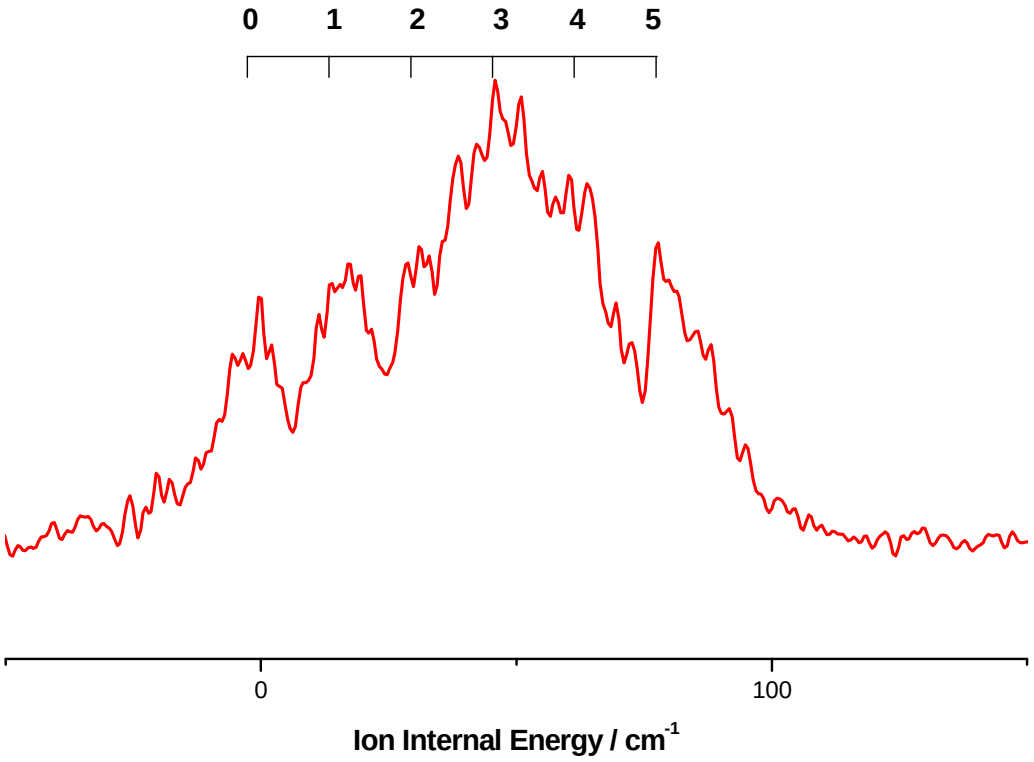

Figure 10.3: MATI spectrum of phenol$^+$…CH_4. The top scale shows the equal spacing between the vibrational modes.

10.3 Discussion

10.3.1 Spectral shift of the first electronic excited state

The $S_1 0^0$ transition of phenol…CH_4 located at 36288.3 ± 0.5 cm^{-1} represents a red-shift of 61 cm^{-1} compared to the S_1 origin of the phenol monomer. It can inferred from Table 11.2 that this value is between the corresponding shift for the H-bound phenol…N_2 (100 cm^{-1}) and the π-bound phenol…Ar (33 cm^{-1}).

Table 10.2: Spectral shift of origin transition of phenol…X cluster relative to the S_1 origin of the phenol monomer.

Cluster	Spectral Shift in S_1 /cm^{-1}
Phenol…NH_3[15]	-650
Phenol…H_20[16]	-353
Phenol…CO[17]	-190
Phenol…N_2[18]	-100
Phenol…Ar[19]	-33
Phenol…CH_4	-61

10.3.2 Intramolecular Vibrations

Among the vibrational modes observed in the R2PI spectrum of phenol…CH_4, our attention is focused on the frequencies of the 6a and 18b in-plane modes. The 6a and 18b modes have the same frequencies as the corresponding monomer phenol bands (see Table 10.1) as expected for a cluster adopting a π-bond geometry.

However, the 6a mode is blue-shifted in the case of the phenol…X (X = H_2O, N_2, CO) clusters adopting a structure with a hydrogen bond interaction (a blue-shift of 2.5 cm^{-1} was observed for phenol…N_2,[16] of 5 cm^{-1} for phenol…H_2O[17] and phenol…CO).[18]

10.3.3 Ionisation Energy

The IE of phenol$^+$…CH_4 is red-shifted by 287 cm^{-1} compared to the IE of the monomer phenol$^+$ cation and lies in-between the corresponding values for phenol$^+$…Ar[19] and phenol$^+$…N_2[18] of 171 cm^{-1} and 1205 cm^{-1}. However the IE is only ~100 cm^{-1} bigger than the IE value for phenol$^+$…Ar suggesting that these clusters have similar geometry in the ionic ground state.

10.3.4 Vibrational modes in cationic state

The nearly harmonic vibrational progression of 15 cm^{-1} observed in the MATI spectrum via the $S_1 0^0$ transition of phenol$^+$…CH_4 has a structure very similar to that of phenol$^+$…Ar_2 (see Chapter 4). The vibrational spacing in the case of phenol$^+$…Ar_2 was found to be around 10 cm^{-1}. In this cluster the mode of this progression was assigned to the symmetric bending mode b_{xs}. On the basis of this spectral similarity, it reasonably assumed that the vibrational progressions in phenol…CH_4 can be assigned to the symmetric bending mode. This assignment is also supported by a comparison with the MATI spectrum of the isoelectronic cluster aniline$^+$…CH_4 which shows analogous vibrational progression (approximately 20 cm^{-1}).[20] Additionally, the mode b_x has exactly the same value in phenol$^+$…Ar[19] and phenol$^+$…CH_4 (15cm^{-1}).

10.3.5 Geometry of phenol…CH_4 in the neutral ground state S_0

As mentioned before, previous works suggest that phenol…CH_4 has a π-bound equilibrium structure in the neutral ground state, S_0.[6,7]

Recently, phenol… CH_4 has been investigated by Fujii and co-workers[8] using REMPI-IR dip. spectroscopy. A short description of the principle of the IR spectroscopy is reviewed prior to discussing the analysis of these results.

The principle of the REMPI-IR dip. spectroscopy in the S_0 and D_0 states is illustrated in Figure 10.4.a and 10.4.b, respectively.[21,22,23] A first UV laser (ν_{UV}), excites the cluster under study to the S_1 origin and a second UV laser (ν_{Ion}) ionises the electronically excited cluster. At the same time, a tunable IR laser (ν_{IR}) is fired and scanned. When the ν_{IR} is resonant with a vibrational transition of the cluster, the vibrationally excited cluster dissociates and the ion current decreases. If ν_{IR} is fired prior to the ν_{UV}, the IR spectrum of the S_0 state can be measured (Figure10.4.a) and if the ν_{IR} is fired after $\nu_{Ion,}$ the IR spectrum of the D_0 state can be recorded (Figure 10.4.b).

The IR spectrum of phenol…CH_4 was measured in the S_0 state (Figure 10.4). The ν_{OH} band of phenol… CH_4 was observed at 36656 cm^{-1} which is only slightly red-shifted (by 2 cm^{-1}) from the corresponding transition of phenol (36658 cm^{-1}). As the ν_{OH} band of phenol…CH_4 also occurs at the same frequency as that of phenol…Ar[19] and phenol…Ar_2,[24] it was concluded that phenol…CH_4 adopts a π-bound minimum structure in the S_0 state.

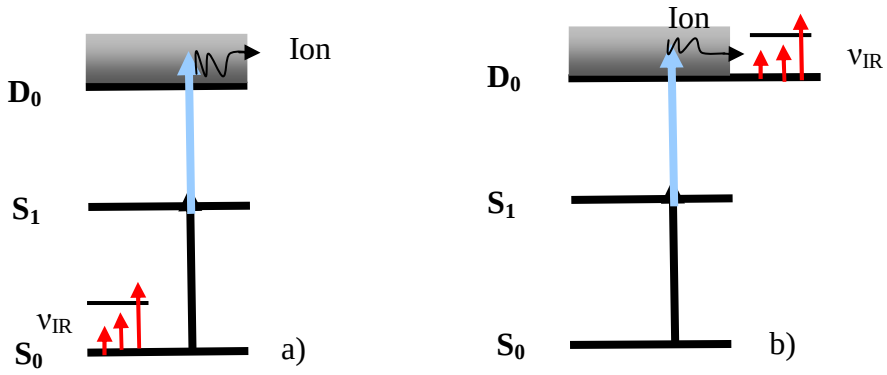

Figure 10.4: Schematic diagram of the principle of a) IR dip. spectroscopy for the neutral ground state S_0, b) for cationic ground state D_0.

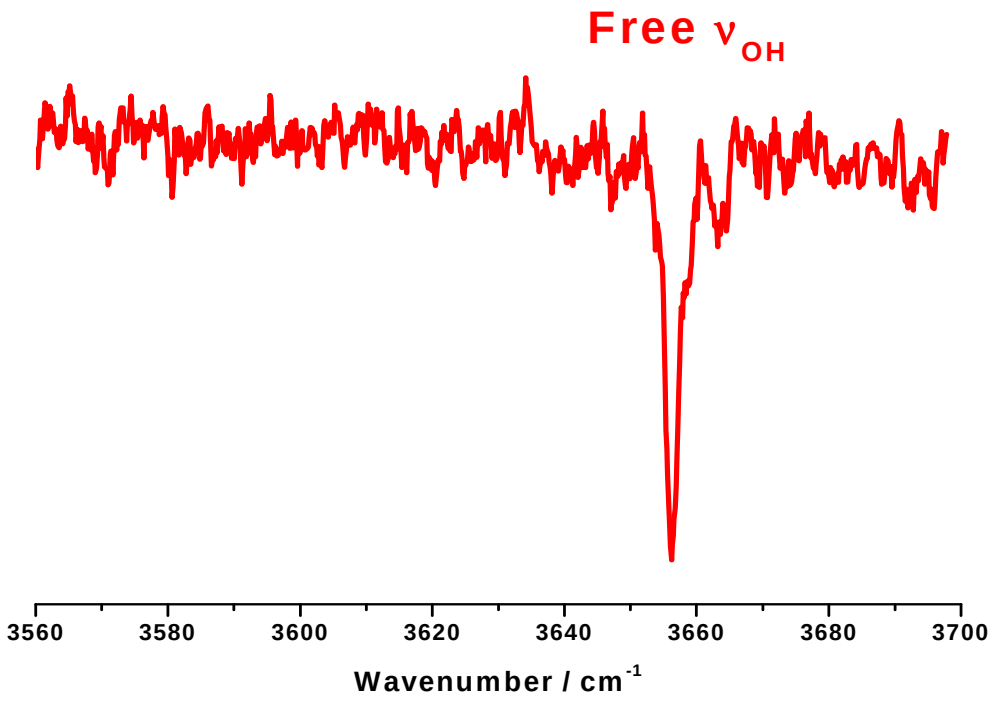

Figure 10.5: IR dip spectrum of phenol…CH_4 in S_0 from Ref 8.

10.3.6 Geometry of phenol…CH_4 in S_1

The spectral shift of the first electronically excited state observed for phenol…CH_4 is only 28 cm^{-1} bigger than the spectral shift relative to phenol…Ar[19] (phenol…Ar adopts

a π-bound structure). However the difference between the spectral shift of phenol… CH_4 and the other clusters adopting H-bond interactions is much bigger (589 cm^{-1}**,** 291 cm^{-1}, 129 cm^{-1}, 49 cm^{-1} for phenol…NH_3, phenol…H_20, phenol…CO and phenol…N_2, respectively). This information combined with the fact that the 6a and 18b in-plane intramolecular vibrational modes have the same frequency as the 6a and18b bands observed in the REMPI spectrum of the phenol monomer again supports the assignment of a π-bound geometry for phenol…CH_4.

10.3.7 IR dip spectrum of phenol$^+$...CH_4 in the ionic D_0 state

The information on the ionic D_0 state of phenol...CH_4 obtained from PIE/MATI spectroscopy has also been expanded by an REMPI-IR dip. spectroscopy of phenol$^+$...CH_4.[8] The IR dip spectrum of phenol$^+$...CH_4 presented in Figure 10.6, displays an intense and broad band ν_{OH} band at 3390 cm^{-1} (in the IR dip spectrum of the phenol monomer in ionic D_0 state, the band relative to the free ν_{OH} was observed at 3534 cm^{-1} [25]). Its position is slightly shifted by 25 cm^{-1} to ν_{OH} of H-bound phenol$^+$...CH_4 obtained by IR spectroscopy of the cluster prepared in an EI source[7]. This result suggests that the phenol$^+$…CH_4 cluster cation produced by photoionisation adopts a H-bound geometry. The appearance of the H-bound structure and a complete absence of the of the π-bound structure in the IR spectrum suggests a π→H site switching in the D_0 state as already observed in the case of phenol$^+$…Ar_2.

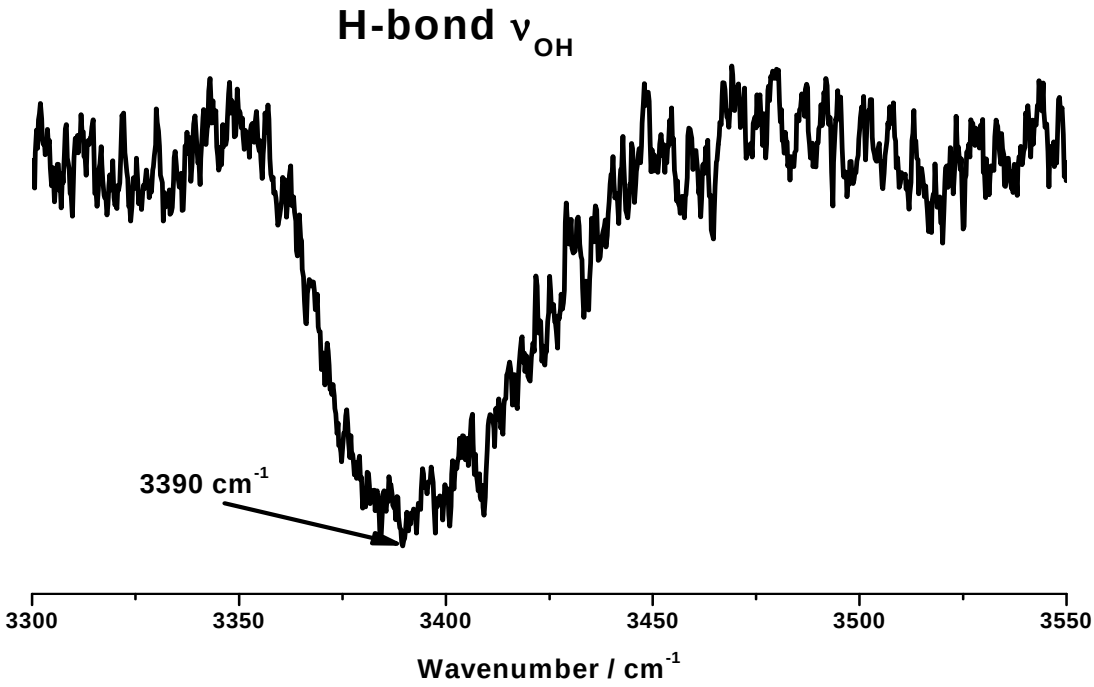

Figure 10.6: IR dip spectrum of phenol$^+$…CH_4 in D_0 from Ref 8.

10.4 Summary and further discussion

In this chapter the REMPI spectrum of phenol…CH_4 revealed that the origin transition $S_1 \leftarrow S_0$ is redshifted by 61 cm^{-1} compared to the origin of the phenol monomer. This value is close to the red-shift found for phenol…Ar (33 cm^{-1}) and confirms the geometrical similarity between argon and methane in these neutral clusters.

The recorded PIE/MATI spectra of phenol…CH_4 allowed the determination of a value of the IE which is red-shifted by 287 cm^{-1}compared to the IE of the phenol monomer. A detailed view of the threshold region showed a vibrational progression of approximately 15 cm^{-1} which was assigned to the symmetric bending mode.

Additionally, the analysis of the IR dip spectrum in the S_0 state demonstrated that the neutral cluster exhibits π-bonding. Interesting results were obtained by recording the IR dip. spectrum of this cluster in cation state. The phenol$^+$…CH_4 cluster prefers hydrogen bonding. This observation implies that π→H site switching occurs in phenol…CH_4 upon the photoionisation process.

Further investigations on this system would be able to confirm the assumption of the π→H isomerisation and produce more information regarding the energetic of this dynamic. A study of the dissociation process by means of MATI spectroscopy, which has been not possible to conduct to date due to the experimental challenge of obtaining significant intensity of the parent cluster for this system, would give an accurate value for the energy necessary for the loss of the methane molecule. Consequently the binding energy for the H-bond could be easily calculated.

10.5 References

[1] E. J. Bieske, M. W. Rainbird, I. M. Atkinson and A. E. W. Knight, *J. Chem. Phys.*, 1989, **91**, 752.

[2] J. N. Israelachvili, *J. Intermolecular and surface Forces;* academic Press, London 1992.

[3] X. Zhang and J. L. Knee, *Faraday Discuss.*, 1994, **97**, 299.

[4] E. R. Bernstein, K. Law and M. Schaur, *J. Chem. Phys.*, 1984, **80,** 634.

[5] J. M. Smith, X. Zhang and J. L. Knee, *J. Chem. Phys.*, 1993, **99,** 2550.

[6] G. V. Hartland, B. F. Henson, V. A. Venturo and P. M. Felker, *J. Chem. Phys.*, 1992, **96**, 1164.

[7] N. Solcà and O. Dopfer, *J. Chem. Phys A*, 2001, **105**, 5637.

[8] A. Takeda, M. Miyazaki, S . Ishiuchi, M. Sakai and M. Fujii unpublished work.

[9] O. Dopfer, PhD Thesis, 1994, Technische Universität München, München

[10] G. Varsanyi, *Assigments for vibrational Spectra of 700 Benzene Derivatives*, Wiley, New York, 1974.

[11] H. W. Wilson, R. W. MacNamee and J. R. Durig, *J. Raman Spectrosc.*, 1981, **11**, 252.

[12] H. D. Bist, J. C. D. Brand and D. R Williams, *J. Mol. Spec*., 1966, **21**, 76; 1967, **24**, 402; 1967, **24**, 413.

[13] M. Takayanagi and I. Hanazaki, *Laser Chem.* 1994, **14**, 103.

[14] C. E. H. Dessent, K. Müller-Dethlefs, Chem. Rev. 2000, **100**, 3999.

[15] D. Solgadi, C. Jouvet and A Tramer. *J. Phys. Chem*., 1988, **92**, 3313.

[16] O. Dopfer, G. Reiser, K. Müller-Dethlefts, E. W. Schlag and S. D. Colson, *J. Chem. Phys*., 1994, **101**, 974**.**

[17] S. R. Haines, C. E. D. Dessent and K. Müller-Dethlefts, *J. Chem. Phys.*, 1999, **111**, 1947.

[18] S. R. Haines, W. D. Geppert, D. M. Chapman, M. J. Watkins, C. E. D. Dessent, M. C. R. Cockett and K. Müller-Dethlefts, *J. Chem. Phys.*, 1998, **109**, 9244.

[19] S.R. Haines, C.E.H. Dessent and K. Müller-Dethlefs, *J. Electron Spectrosc. Relat. Phenom*. 2000, **108**, 1.

[20] X. Zhang, J. M. Smith and J. L. Knee *J. Phys. Chem*., 97, **1992**, 2843**.**

[21] T. S. Zwier, *J. Chem. Phys. A,* 2001, **105**, 8827.

[22] B. Brutschy, *Chem. Rev. (Washington, D. C.)*, 2000, **100**, 3891.

[23] R. H. Page, Y. R. Shen, and Y. T. Lee, *J. Chem. Phys.*, 1988, **88**, 5362.

[24] S. Ishiuchi, M. Sakai, Y. Tsuchida, A. Takeda, Y. Kawashima, O. Dopfer, K. Müller-Dethlefts and M. Fujii, *J. Chem. Phys*, 2007, **127**, 114307.

[25] A. Fujii, T. Sawamura, S. Tanabe, T. Ebata and N. Mikami, *Chem. Phys. Lett.***,** 1994, **225**, 104.

Chapter 11

Conclusions and future works

The spectroscopic investigations using high-resolution spectroscopic methods such as REMPI, ZEKE/MATI, PIE spectroscopy reported in this work of thesis has contributed to establish the geometries adopted by simple van der Waals complexes which represents a starting point to provide basic information on the structural, energetic, and dynamic manifestations of intermolecular forces involving much larger chemical systems, including the study of biomolecules. In particular, these studies on clusters containing aromatic systems and gas rare have given further information which is essential to better understand how the salvation processes work. This knowledge is also important for further refinement of *ab initio* computational methods. The achievements of new results regarding the dissociation processes and a precise determination of the fragmentation energies of such clusters have been possible only by employing MATI spectroscopy.

In more details, photoionisation of the π-bound neutral phenol…Ar_2 cluster was expected to conserve the π-bound configuration due to the Frank–Condon principle. However, determination of the dissociation thresholds for the loss of one and two argon atoms in phenol$^+$…Ar_2 revealed the surprising existence of a H-bound structure of this cluster upon ionisation, suggesting that a π→H site switching occurs.

The R2PI spectra of phenol…Ar_n (*n*=3-6) revealed that the origins of the transition $S_1 \leftarrow S_0$ transition are red-shifted compared to the monomer origin for all the clusters with the only exception of phenol…Ar_3, where a blue-shift was observed. A comparison of the origin spectral shifts with the monomer origin of one-side aniline…Ar_n (*n*=3-6) conformers showed a similar trend to those of phenol…Ar_n (*n*=3-6). This points to similar structures for phenol…Ar_n (*n*=3-6) where argon atoms are located on one side of the aromatic ring.

A similar scenario to the dissociation processes of phenol$^+$…Ar_2 has been found for phenol$^+$…Ar_3. The energy diagram drawn to explain the dissociation process in phenol$^+$…Ar_3 showed that a $\pi \rightarrow H$ isomerisation occurs upon ionisation as observed for phenol$^+$…Ar_2. The binding energy of the hydrogen bond between the phenol cation and argon atom was calculated (~ 870 cm^{-1}, similar to the value found in phenol$^+$…Ar_2). This value, as expected, is between the much stronger conventional hydrogen bond and typical weaker vdW bond. A very surprising value was found for the dissociation energy for the loss of the four argon atoms (less than 900 cm^{-1}) from phenol$^+$…Ar_4. This indicated a structure where the four argon atoms adopt a tetrahedral symmetry on one side of the aromatic ring. Interesting results were also obtained by recording the IR dip spectrum of phenol$^+$…CH_4 in cation state. Also in this case, a $\pi \rightarrow H$ isomerisation occurs upon ionisation.

To obtain further confirmations and information regarding the stability and the structures of the clusters analysed, it would be convenient to carry out other experimental and computational investigations.

As an extension of previous theoretical study complexes calculations to obtain structures and relative energies are already started also for the larger clusters (*n*=4-6). The difficulty of guessing the possible argon arrangements in the larger clusters is solved performing random relaxed scan of the geometry, probing thus the potential energy surface (PES) of the complexes. From these starting geometries further optimisation can provide the most stable geometries of the different conformers for each cluster.

Additionally, a further investigation on the phenol…Ar_n (*n*=2-6) using the spectroscopic methodologies used in these work of thesis, combined with hole burning spectroscopy can be carried out changing the thermodynamic conditions (in particular the pressure of the Argon gas) to possibly prove the existence of other conformers for each cluster.

Finally the analysis of the dissociation process of phenol$^+$…CH_4 can be only completed if the MATI spectra *via* the $S_1 0^0$ state of phenol…CH_4 are simultaneously recorded at the mass channel of the cluster and the phenol$^+$ fragment.

Chapter 12

Appendix

12.1 Appendix A: *Ab Initio* calculation methodologies

12.1.1 Introduction

The use of computational methods can be a valid support for a complete analysis and interpretation of the spectroscopic experiment. Molecular mechanics and semi-empirical methods can give an approximate evaluation of the properties of molecular clusters but only an *ab initio* approach for the calculation of van der Walls or hydrogen bonded complexes can offer the reasonable reflections of the true structure.

A short description of the theoretical basis for *ab initio* calculations is here reported.

12.1.2 Definition of *ab initio* quantum chemistry

The basis of electronic structure calculation is the solution of the non-relativistic, time-independent Schrödinger equation. The Hamiltonian $\hat{H}$ (equation 12.1) expressed in atomic units is a function of the nuclear and electronic coordinates of the molecule (equation 12.2). The first two terms are the electronic and nuclear kinetic energy operators $\hat{T}_e$ and $\hat{T}_N$, the third the nuclear-nuclear potential energy operator $\hat{V}_{NN}$, the fourth the nuclear-electronic potential energy operator $\hat{V}_{Ne}$ and the fifth the electronic

potential energy operator $\hat{V}_{ee}$ (*i,j* are the indices for electrons, *I,J*… indices for the nuclei) (equation 12.3)

$$\hat{H}\Psi = E\Psi \quad [12.1]$$

$$\hat{H} = -\tfrac{1}{2}\sum_i \nabla_i^2 - \sum_I \frac{1}{2M_i}\nabla_I^2 + \sum_{I>J}\frac{Z_I Z_J}{R_{IJ}} - \sum_{Ii}\frac{Z_I}{r_{Ii}} + \sum_{i>j}\frac{1}{r_{ij}} \quad [12.2]$$

$$\hat{H} = \hat{T}_e + \hat{T}_N + \hat{V}_{NN} + \hat{V}_{Ne} + \hat{V}_{ee} \quad [12.3]$$

The equation 12.1 cannot be solved analytically when we consider any molecule with more degrees of freedom than H_2^+ and only the use of approximations can provide a solution to this equation. The major approximation used in quantum chemistry is the *Born Oppenheimer approximation*. This approximation separates the electronic and nuclear components of the Hamiltonian. Within this approximation, the electronic Hamiltonian is written as:

$$\hat{H}_e = -\tfrac{1}{2}\sum_i \nabla_i^2 + \sum_{I>J}\frac{Z_I Z_J}{R_{IJ}} - \sum_{Ii}\frac{Z_I}{r_{Ii}} + \sum_{i>j}\frac{1}{r_{ij}} \quad [12.4]$$

$$\hat{H}_e\Psi_e = E(R)\Psi_e \quad [12.5]$$

The equation 12.4 can be rewritten as

$$\hat{H}_e = \hat{T}_{ee} + \hat{V}_{eN} + \hat{V}_{ee} = \sum_i \hat{h}(i) + \sum_i\sum_{j>i}\hat{v}(i,j) \quad [12.6]$$

$$\sum_i\sum_{j>i}\hat{v}(i,j) \approx \sum_i \hat{v}(i) \quad [12.7]$$

$$\hat{H}_e \approx \sum_i [\hat{h}(i) + \hat{v}(i)] = \sum_i \hat{H}'(i) \quad [12.8]$$

Where $\hat{h}(i)$ is known as the core Hamiltonian, a hydrogenic Hamiltonian for the i^{th} electron in the field of a bare nucleus of charge Z The Hamiltonian effectively becomes an one-electron operator.

12.1.3 The Hartree-Fock method

In the Hartree-Fock (HF) approximation, the electron-electron repulsion is treated in average way. Thus each electron has its own wave equation and the other electrons are treated as an average field.

The antisymmetric product of *n*-electron wave function used in the Hartree-Fock method can be expressed in the form of a Slater determinant shown in equation 12.9:

$$\Psi(1,2,\ldots n) = \frac{1}{\sqrt{n!}}\det[\varphi_i] = \frac{1}{\sqrt{n!}}\begin{bmatrix} \varphi_1(1) & \varphi_2(1) & \cdots & \varphi_n(1) \\ \varphi_1(2) & \varphi_2(2) & \cdots & \varphi_n(2) \\ \cdots & \cdots & \cdots & \cdots \\ \varphi_1(n) & \varphi_2(n) & \cdots & \varphi_n(n) \end{bmatrix} \quad [12.9]$$

or using the standard shorthand notation:

$$\boldsymbol{\psi}=[\psi_1\psi_2\ldots\psi_a\psi_b\ldots\psi_n] \quad [12.10]$$

Therefore the energy can be evaluated as following:

$$E[\Psi] = \left\langle \Psi \middle| \hat{H}_e \middle| \Psi \right\rangle = 2\sum_i^{N/2} h_i + \sum_i^{N/2}\sum_j^{N/2}(2J_{ij} - K_{ij}) \quad [12.11]$$

where h_i again represents the one-electron core Hamiltonian , J_{ij} *i*s the electron Hamiltonian for Coulomb interactions and K_{ij} is the Hamiltonian for the exchange interaction.

$$h_i = \left\langle \varphi_i(i) \middle| \hat{h}(i) \middle| \varphi_i(i) \right\rangle \quad [12.12]$$

$$J_{ij} = \left\langle \varphi_i(i)\varphi_j(j) \middle| \hat{v}_{ij} \middle| \varphi_i(i)\varphi_j(j) \right\rangle \quad [12.13]$$

$$K_{ij} = \left\langle \varphi_i(i)\varphi_j(j) \middle| \hat{v}_{ij} \middle| \varphi_j(i)\varphi_i(j) \right\rangle \quad [12.14]$$

At this point two new operators, called the Coulomb and exchange operators are introduced (shown in equations 12.15 and 12.16, respectively). It can be easily seen that

the operators in 12.15 and 12.16 give rise to the integrals in 12.13 and 12.14, respectively and a new one-electron Hamiltonian is defined (see equation 12.17).

$$\hat{J}_i\left|\varphi_j(j)\right\rangle = \left\langle\varphi_i(i)\left|\hat{v}_{ij}\right|\varphi_i(i)\right\rangle\left|\varphi_j(j)\right\rangle \quad [12.15]$$

$$\hat{K}_{ii}\left|\varphi_j(j)\right\rangle = \left\langle\varphi_i(i)\left|\hat{v}_{ij}\right|\varphi_j(i)\right\rangle\left|\varphi_i(j)\right\rangle \quad [12.16]$$

$$\hat{F}_i = \hat{h}_i + \sum_{j=1}^{n}(\hat{J}_j - \hat{K}_j) \quad [12.17]$$

$$\hat{F}_i\varphi_i = \varepsilon_i\varphi_i \quad [12.18]$$

For molecules, basis set expansions are almost always used to describe the molecular orbitals, φ_i:

$$\varphi_i = \sum_{\mu} c_{\mu i} f_\mu \quad [12.19]$$

Variational optimisation of the orbital coefficients is achieved through Hartree-Fock-Roothan equations, shown below:

$$FC = SCe \quad [12.20]$$

where **F** is the Fock matrix, **C** the matrix of the orbital coefficients and **S** the overlap matrix between different atomic orbitals, and **e** the diagonal matrix of the orbital energies.The equation 12.20 only has a non-trivial solution if the following secular determinant is satisfied:

$$\det = \left|\mathbf{F}-\boldsymbol{\varepsilon}\mathbf{S}\right| = 0 \quad [12.21]$$

Since the Fock matrix is only known if molecular orbitals are known, the procedure starts off by some guess of the coefficients, forms the **F** matrix, and diagonilises it. The new set is used for calculating a new Fock matrix, etc. This process continues until the set of coefficients used for constructing the Fock matrix is equal to those resulting from

the diagonalisation. This iterative procedure is known as the self consistent field (SCF) method and the resulting wavefunction is called the SCF wave function (Figure 12.1).

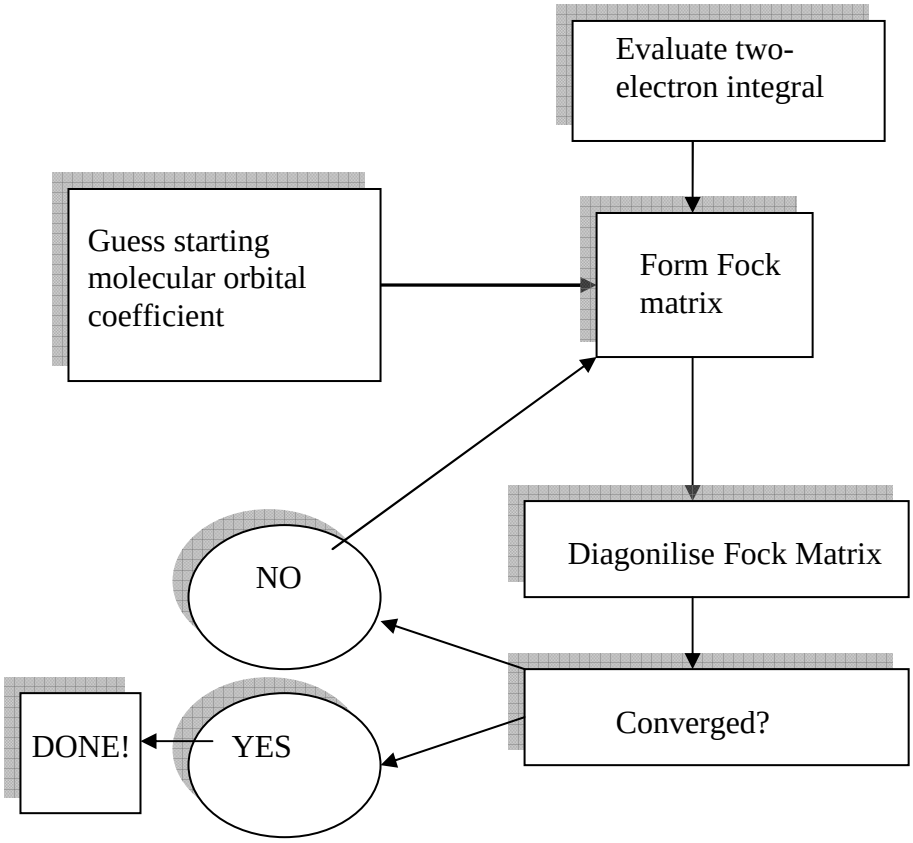

Figure 12.1: Hartree-Fock self-consistent procedure.

12.1.4 Electron correlation methods

The HF method generates solutions to the Schrödinger equation where the real electron interaction is substituted by an average interaction. The HF wave function is able to consider the 99 % of the total energy, but no the remaining 1 % which is important to describe chemical phenomena. The difference between the HF and the lowest possible energy in the given basis set is called *Electron correlation* energy[1,2] The HF method determines the energetically best one-determinant trial wave function. It is therefore clear that in order to improve the HF result the start point has to be a trial wave function

that contains more than one Slater determinant, φ. A generic trial wave function can be written as:

$$\Psi = a_0\varphi_{HF} + \sum_{i=1} a_1\varphi_i \qquad [12.22]$$

Electron correlation methods differ in how the coefficients in front of the determinants are calculated, with a_0 being determined by the normalization condition.

There are three main methods to calculate electron correlation: *Configuration Interaction* (CI), *Many-Body Perturbation Theory* (MBPT) and *Coupled Cluster* (CC).

Configuration interaction

In this method, the trial wave function is a linear combination of determinants with expansion coefficients determined by requiring that the energy should be a minimum. Subscripts S, D, T, etc. indicate determinants that are singly, doubly, triply, excited relative to the HF configuration:

$$\Psi_{CI} = a_0\varphi_{HF} + \sum_S a_s\varphi_s + \sum_D a_D\varphi_D + \sum_T a_T\varphi_T ... \sum_{i=0} a_i\varphi_i \qquad [12.23]$$

Many-body perturbation theory

The perturbation method is based on the fact system under study differs slightly from a system which has been already solved. Mathematically, this can be described introducing a Hamiltonian **(H)** operator consisting of two parts: a reference H_0 and a perturbation H'**.** Usually the perturbation is expressed as a power series, and so H can be written as:

$$H = H_0 + \lambda H' \qquad [12.24]$$

$$H = H_0 + \lambda H_1 + \lambda^2 H_2 + \lambda^3 H_3 + ... \qquad [12.25]$$

The total energy and the wave function of the perturbed system can also be expressed as a power series:

$$E = E_0 + \lambda E_1 + \lambda^2 E_2 + \lambda^3 E_3 + ... \quad [12.26]$$

$$\psi = \psi_0 + \lambda \psi_1 + \lambda^2 \psi_2 + \lambda^3 \psi_3 + ... \quad [12.27]$$

In order to apply perturbation theory to the calculation of correlation energy, the unperturbed Hamiltonian operator must be selected. The most common choice is based on taking this as a sum over Fock operators, leading to Møller-Plesset (MP) perturbation theory[3].

Coupled-cluster theory

The central tenet of the coupled cluster theory is that the full-CI (configuration interaction) wave function can be described as[4]:

$$\Psi = e^T \Psi_{HF} \quad [12.28]$$

The cluster operator is defined as:

$$T = T_1 + T_2 + T_3 + ... + \mathrm{T}_n \quad [12.29]$$

where n is the total number of electrons and the various $\mathrm{T_i}$ operators generate all possible determinants having i excitation from the reference.

12.1.4 Basis sets

One of the approximations inherent in essentially all *ab initio* methods is the introduction of a basis set.

A finite number of functions are used as a basis set to represent an unknown molecular orbital (MO) which is accurately represented only by an infinite number of functions.

The most efficient strategy is to represent the MOs as *linear combinations of atomic orbitals* (LCAO):

$$\varphi_i = \sum_{\mu} c_{\mu i} f_{\mu} \qquad [12.30]$$

There are two types of basis functions commonly used in electronic structure calculations:

- Slater-type Orbitals (STO)[5]
- Gaussian Type Orbitals (GTO)[6]

Slater-type orbital

Slater-type orbitals have the functional form shown in the equation 12.31:

$$f_{\varsigma,n,l,m}(r,\vartheta,\phi) = NY_{l,m}(\vartheta,\phi)r^{n-1}e^{-\zeta r} \qquad [12.31]$$

Where N is a normalization constant and $Y_{l,m}$ are spherical harmonic functions. The exponential dependence on the distance between the nucleus and electron mirrors the exact orbitals for the hydrogen atom. However there is no radial node in any single STO function; nodes in the radial part are introduced by making linear combinations of STOs. The evaluation of two-electron integrals using STOs is very time consuming, for this reason the STOs are primarily used for atomic and diatomic systems where high accuracy is required.

Gaussian-type orbital

The use of Gaussian–type orbitals (GTO) can be considered computationally more practical and a preferred option. GTOs can be written in terms of polar (equation 12.32) or Cartesian coordinate (equation 12.33):

$$f_{\varsigma,n,l,m}(r,\vartheta,\phi) = NY_{l,m}(\vartheta,\phi)r^{2n-2-l}e^{-\zeta r^2} \quad [12.32]$$

$$f_{\varsigma, Ix, Iy, Iz}(x,y,z) = N\, x^{Ix} y^{Iy} z^{Iz}\, e^{-\varsigma r} \quad [12.33]$$

The sum of I_x, I_y, I_z, determines the type of orbitals (for example $I_x + I_y + I_z = 1$) is a p-orbital. The r^2 dependence in the exponential makes the GTOs inferior to STOs in two aspects.

1. At the nucleus a GTO has a zero slope, in contrast to a STO which has a "cusp" (discontinuous derivative), and as a consequence the GTOs do not properly represent the behaviour near the nucleus.
2. The GTO falls off too rapidly far from the nucleus compared with an STO. More GTOs are necessary to achieve a certain accuracy compared with STOs. However, the increase in the number of GTO basis functions is more than compensated by the fact that the integrals can be easily calculated. The GTOs are therefore preferred and used universally as basis function in electronic calculations.

12.1.5 Classification of basis sets

The smallest number of functions possible is a minimum basis set. Only a sufficient number of functions are employed to contain all the electrons. For example, for hydrogen and helium, this means a single *s*-function. For the first row in the periodic system it means two *s*-functions (1s and 2s) and one set of *p*-functions ($2p_x$, $2p_y$, and $2p_z$).

The next improvement of basis sets is a doubling of all basis functions, producing a double zeta (DZ) type basis. This means, for example, that a DZ basis employs two

s-functions for hydrogen (1s and 1s'), four *s*-functions (1s, 1s', 2s and 2s') and two sets of *p* –functions for second row elements. However because the chemical bonding occurs between valence orbitals, a variation of the DZ type basis only doubles the number of valence orbitals, producing a s*plit valence basis.*

The next step in basis set size is a *Triple Zeta (TZ) (*three times as many functions as the minimum basis) , *Quadrupule Zeta (QZ)* and *Quintuple Zeta(PZ).*

In most cases, higher angular momentum functions have to be introduced for a better description of the system. These are denoted polarization functions due to the fact that p-orbital introduces a polarization of the s-orbital, and similarly d-orbitals are responsible for polarizing p-orbital, f-orbital for polarizing d-orbitals and etc. Polarization functions are added to sp-basis. Adding a single set of polarization functions (p-functions on hydrogens and d-functions on heavy atoms) to the DZ basis forms a *Double Zeta plus Polarization* (DZP) type basis. Multiple sets of polarization functions are added to a TZ sp-basis, a triple zeta plus double polarization (TZ2P) type basis is obtained.

12.1.6 Contracted basis sets

Combining the full set of basis functions, known as the *primitive* GTOs (PGTOs), into a smaller set of functions by forming fixed linear combinations is known as basis set *contraction* and the resulting functions are called contracted basis set (equation 12.34).

$$f(CGTO) = \sum_{i}^{k} a_i f_i(PGTO) \qquad [12.34]$$

There are two different ways of contracting a set of primitive GTOs to a set of contracted GTOs: *segmented* and *general contraction.* In the segmented contraction, a given set of PGTOs is portioned into smaller sets of functions that are made into

CGTOs by determining suitable coefficients. In a general contraction all primitives (on a given atom) enter all the contracted functions, but with different contraction coefficients.

Pople style basis sets

STO-nG basis sets[7]

These are *Slater type orbitals* consisting of *n* PGTOs. This is a minimum type basis where the exponents of the PGTO are determined by fitting to the STO, rather than optimizing them by a variational procedure.

k-mlmG basis sets

These basis sets are split valence types, with the *k* in front of the dash indicating how many PGTOs are used for representing the core orbitals. The *nml* after the dash indicate both how many functions the valence orbitals are split into, and how PGTOs are used for their representation. Two values (*nl*) indicate a split valence, while three values (*nml*) indicate a triple split valence. The values before the G (for Gaussian) indicate the s- and p-functions in the basis.

All the Pople style basis sets can be extended by adding diffuse[8] and / or polarization functions[9].

Dunning-Huzinaga (DH) basis sets

An alternative to the Pople type basis sets is a family of basis set devised by Dunning and co-workers.[10,11,12] These basis sets have built up systematically and by using successively larger basis sets in the series; the energies, geometries and other properties converge to a complete basis set limit.

Atomic natural orbitals basis sets

Pople style and DH basis sets are of the segmented contraction type. Modern contracted basis sets aimed at producing very accurate wave functions often employ a general contraction scheme. The Atomic natural orbitals basis sets (ANO) and Correlations consistents basis sets (cc) are of the general contraction type. The idea in the Atomic Natural Orbital type basis sets is to contract a large PGTO set to a fairly small number of CGTO by using natural orbitals from a correlated calculation on the free atom.

Correlation Consistent (cc) basis sets

The correlation consistent basis sets are geared toward recovering the correlation energy of the valence electrons. The basis sets are designed such that functions that contribute similar amounts of correlation energy are included at the same stage, independent of the function type. Several different sizes of cc basis sets are available in terms of final number of contracted functions. These are known by their acronyms: cc-pVDZ, cc-pVTZ, cc-pVQZ, cc-pV5Z and cc-pV6Z.[13]

12.1.7 Basis set superposition errors

When the energies are compared at different geometries, the nuclear fixed basis introduces an error. The quality of the basis set is not the same at all geometries. This effect is more evident when van der Waals complexes or hydrogen bonds are considered and is known as the *Basis Set Superposition Error* (BSSE). Many methods are used to evaluate this error; the most common is the *Counterpoise* (CP) correction.[14] The CP correction is defined by the equation 12.35.

$$\Delta E_{CP} = E(A)_{AB} + E(B)_{AB} - E(A)_{A} - E(B)_{B} \qquad [12.35]$$

Where $E(A)_{AB}$ and $E(B)_{AB}$ are the energies of the monomers calculated with the combined basis set *ab* and $E(A)_A$ and $E(B)_B$ are the energies of the monomers calculated with the basis set *a* and *b* respectively.

12.2 Appendix B: Rotational band counter analysis

Rotational band counter analysis of the REMPI spectrum of phenol…Ar_3 has been carried out using the simulated spectra generate with in-house software employing the rigid rotor approximation.[15]

The simulated spectra are calculated using rotational constants (S_1 rotational constants are 2 % smaller than the S_0 constants) from *ab initio* calculated geometries (asymmetric REMPI simulation (ARS)). After that, the software tries to fit the simulated spectrum to the experimental REMPI spectrum (asymmetric REMPI fitting (ARF)).

All fits in this thesis were carried out by optimising the correlation coefficient between experimental and simulated spectrum to unity, at which identity of the two spectra is achieved. The two sets of rotational constants for S_0 and S_1 are simultaneously optimised using a Monte-Carlo procedure. Other parameters are optimised independently by directly maximising the correlation coefficient. A Lorentzian was used as the lineshape function with a line-width of 1200 MHz. The fitting was carried out with a precision for the correlation coefficient of 0.96 which was sufficiently accurate for the determination of the best fitting.

12.3 References

[1] A.Szabo and N. S. Osttlund, *Modern Quantum Chemistry*, McGraw-Hill. 1982

[2] R. McWeeny, *Methods of Molecular Quantum Mechanics*, Academic Press, 1992.

[3] C.Møller and M. S. Plesset**,** *Phys. Rev.*, 1934, **46**, 618.

[4] R. J. Bartlett, *J. Phys. Chem*., 1989, **93,** 1697.

[5] J.C. Slater, *Phys. Rev.*, 1930, **36,** 50.

[6] S. F. Boys, *Proc. R. Soc. (London) A*, 1950, **200**, 542.

[7] W.J.HeHre, R. F. Stewart and Pople, *J. Chem. Phys*. 1969, **51**, 2657.

[8] M. J. Frisch and J. A. Pople, *J. Chem. Phys.*, 1969, **51,** 2657**.**

[9] M. M. Francl, W. J. Pietro, W. J. Hehre, J. S. Binkley, M. S. Gordon, D. J. Defrees and J. A. Pople, *J. Chem. Phys.*, 1982, **77,** 3654.

[10] T. H. Dunning, *J. Chem. Phys*., 1989, **90**, 1007.

[11] R. A. Kendall, R. J. Harrison and T. H. Dunning, *J. Chem. Phys*.1992, **96**, 6796.

[12] D. E. Woon and T. H. Dunning, *J. Chem. Phys.*, 1995, **103,** 4572.

[13] A. K. Wilson and T. H. Dunning, *J. Chem. Phys.*, 1997, **106**, 8718.

[14] S. F. Boys and F. Bernardi, *Mol. Phys*. 1970, **19**, 553.

[15] M. S. Ford, *Ph.D thesis*, University of York, 2002.